NASA Technical Memorandum 104566, Vol. 26

SeaWiFS Technical Report Series

Stanford B. Hooker and Elaine R. Firestone, Editors

Volume 26, Results of the SeaWiFS Data Analysis Round-Robin, July 1994 (DARR-94)

David A. Siegel, Margaret C. O'Brien, Jens C. Sorensen, Daniel A. Konnoff, Eric A. Brody, James L. Mueller, Curtiss O. Davis, W. Joseph Rhea, and Stanford B. Hooker

May 1995

NASA Technical Memorandum 104566, Vol. 26

SeaWiFS Technical Report Series

Stanford B. Hooker, Editor
NASA Goddard Space Flight Center, Greenbelt, Maryland

Elaine R. Firestone, Technical Editor
General Sciences Corporation, Laurel, Maryland

Volume 26, Results of the SeaWiFS Data Analysis Round-Robin, July 1994 (DARR-94)

David A. Siegel, Margaret C. O'Brien, Jens C. Sorensen, Daniel A. Konnoff, and Eric A. Brody
University of California, Santa Barbara, Santa Barbara, California

James L. Mueller
San Diego State University, San Diego, California

Curtiss O. Davis and W. Joseph Rhea
Naval Research Laboratory, Washington, DC

Stanford B. Hooker
NASA Goddard Space Flight Center, Greenbelt, Maryland

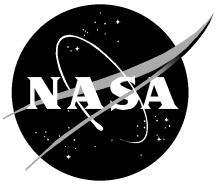

National Aeronautics and
Space Administration

Goddard Space Flight Center
Greenbelt, Maryland 20771

1995

Preface

One of the primary objectives of the SeaWiFS Project, as stated in Volume 1 of this technical memorandum series (Hooker et al. 1992), is "to achieve radiometric accuracy of 5% absolute and 1% relative, water-leaving radiances to within 5% absolute, and chlorophyll *a* concentration to within 35% over the range of 0.05–50.0 $\mathrm{mg\,m^{-3}}$." This objective presents a challenge to the ocean color community, and the SeaWiFS Calibration and Validation Team (CVT) has initiated a number of activities directed towards attaining these accuracy goals which include

1) The SeaWiFS Intercalibration Round-Robin Experiments (SIRREXs),
2) The development of *in situ* measurement protocols (Mueller and Austin 1992 and 1995),
3) The construction of the SeaWiFS transfer radiometer (SXR),
4) Support for the Marine Optical Buoy (MOBY), and
5) Support for the collection of high quality bio-optical data sets.

These activities address the issues of instrument calibration, data collection techniques, and bio-optical data set diversity.

An additional aspect to the problem is the methodology by which vertical profiling radiometric observations are extrapolated to the surface so field observations can be compared with the satellite derived products or used as inputs for satellite bio-optical algorithms. The first SeaWiFS Data Analysis Round-Robin (DARR-94) was convened for the purpose of comparing the various techniques being used by the ocean color community, to clarify the sources of error, and work toward establishing standard methods for deriving the relevant products, e.g., water-leaving radiance and diffuse attenuation. This technical memorandum summarizes the results of DARR-94 and establishes that careful data analysis is necessary and that errors in the analysis can lead to very large errors in the derived fields. As a result of DARR-94, it is clear that continued refinement of radiometric data analysis techniques is necessary. Therefore, as with the instrument round-robins, the CVT will promote additional analysis round-robins in a continuing effort to attain the SeaWiFS mission objectives.

Greenbelt, Maryland — C. R. McClain
February 1995

Table of Contents

Abstract

The accurate determination of upper ocean apparent optical properties (AOPs) is essential for the vicarious calibration of the Sea-viewing Wide Field-of-view Sensor (SeaWiFS) instrument and the validation of the derived data products. To evaluate the role that data analysis methods have upon values of derived AOPs, the first Data Analysis Round-Robin (DARR-94) workshop was sponsored by the SeaWiFS Project during 21–23 July, 1994. The focus of this intercomparison study was the estimation of the downwelling irradiance spectrum just beneath the sea surface, $E_d(0^-, \lambda)$; the upwelling nadir radiance just beneath the sea surface, $L_u(0^-, \lambda)$; and the vertical profile of the diffuse attenuation coefficient spectrum, $K_d(z, \lambda)$. In the results reported here, different methodologies from four research groups were applied to an identical set of 10 spectroradiometry casts in order to evaluate the degree to which data analysis methods influence AOP estimation, and whether any general improvements can be made. The overall results of DARR-94 are presented in Chapter 1 and the individual methods of the four groups are presented in Chapters 2–5. The DARR-94 results do not show a clear winner among data analysis methods evaluated. It is apparent, however, that some degree of *outlier* rejection is required in order to accurately estimate $L_u(0^-, \lambda)$ or $E_d(0^-, \lambda)$. Furthermore, the calculation, evaluation and exploitation of confidence intervals for the AOP determinations needs to be explored. That is, the SeaWiFS calibration and validation problem should be recast in statistical terms where the *in situ* AOP values are statistical estimates with known confidence intervals.

PROLOGUE

The Sea-viewing Wide Field-of-view Sensor (SeaWiFS) Project is tasked with executing a program to acquire the global SeaWiFS data set, validate and monitor its accuracy and quality, process the radiometric data into geophysical units using a set of atmospheric and bio-optical algorithms, and distribute the final products to the scientific community through the Goddard Space Flight Center (GSFC) Distributed Active Archive Center (DAAC). The SeaWiFS data products are prominent components of major scientific programs studying global climate change, including the Joint Global Ocean Flux Study (JGOFS), the World Ocean Circulation Experiment (WOCE), and the Global Ocean Ecosystems dynamics (GLOBEC) programs.

The accurate determination of upper ocean apparent optical properties (AOPs) is essential for the vicarious calibration of the SeaWiFS instrument and the validation of the derived data products. The only economically feasible approach for minimizing spatial biases is to maximize the acquisition of global *in situ* measurements by soliciting contributions of data from the oceanographic community at large, and to combine them with data collected from SeaWiFS sponsored activities into a single database. The SeaWiFS Calibration and Validation Team (CVT) have responded to this need by implementing the SeaWiFS Bio-Optical Archive and Storage System (SeaBASS). Data from a variety of sources are expected to go into this database including

- The Bermuda Bio-Optics Project (BBOP),
- The Bermuda Atlantic Time-series Study (BATS),
- The California Cooperative Fisheries Institute (CalCoFI),
- The JGOFS Equatorial Pacific (EqPac) process study,
- The Gulf of Mexico Experiment (GOMEX), and
- The Tropical Ocean Global Atmosphere (TOGA) Coupled Ocean-Atmosphere Response Experiment (COARE).

The accuracy of any AOP determination is a function of the quality of the measurement, and the differences in the data analysis method employed. In order to minimize observational errors, the SeaWiFS Project has sponsored a variety of multidisciplinary workshops to outline the observations and sampling protocols required for bio-optical algorithm development (Mueller and Austin 1992 and 1995). One of the consequences of the workshops was the establishment of a series of SeaWiFS Intercalibration Round-Robin Experiment (SIRREX) activities to establish and advance the state of the art for calibrating the instruments used in field activities, e.g., the Marine Environmental Radiometers (MERs).

Although the SeaBASS architecture allows for some quality control (Hooker et al. 1994), it is based primarily on resolving obvious clerical errors in the reporting of where and when data acquisiton activities took place—it does not attempt to quantify differences in the data analysis methods employed. The latter is, in part, a function of how the individual software packages deal with data despiking, binning and smoothing, and removing possible artifacts from changes in surface illumination, ship shadow, or reflections and wave focusing.

The focus of this intercomparison study is the estimation of the downwelling irradiance spectrum just beneath the sea surface, $E_d(0^-, \lambda)$, the upwelling nadir radiance

just beneath the sea surface, $L_u(0^-, \lambda)$, and the vertical profile of the diffuse attenuation coefficient spectrum, $K_d(z, \lambda)$. In the results reported here, different methodologies from four research groups are applied to the aforementioned spectroradiometry profiles in order to evaluate the degree to which data analysis methods influence AOP estimation, and whether any general improvements can be made. The four groups involved were as follows:

1. The University of California at Santa Barbara (UCSB) Institute for Computational Earth System Science (ICESS),
2. San Diego State University (SDSU) Center for Hydro-Optics and Remote Sensing (CHORS),
3. The Naval Research Laboratory (NRL), and
4. Scripps Institution of Oceanography (SIO).

The overall results of the first Data Analysis Round-Robin (DARRone) are presented in Chapter 1 and the individual methods of the four groups are presented in Chapters 2–5, respectively. The attendees to the workshop are given in Appendix A. A summary of the material presented in each Chapter is given below.

1. *The First SeaWiFS Ocean Optics DARR*

This study shows that with *good* data (near-constant incident irradiance), the different analyses produce estimates of $L_u(0^-, \lambda)$ and $E_d(0^-, \lambda)$ that are within 3–4% of the aggregate mean value. The statistical uncertainties in determining $E_d(0^-, \lambda)$ are considerably larger (approximately 7%) than those for $L_u(0^-, \lambda)$ (about 2%). These differences can be attributed to geophysical noise sources in the raw data streams which appear to be primarily due to the aliasing of surface wave induced glinting in the vertical radiometric profiles. Furthermore, the profile of the diffuse attenuation coefficient spectrum, $K_d(z, \lambda)$, can be replicated to better than 5% with the different analyses. These differences account for much of the total 5% uncertainty that is tolerated for SeaWiFS calibration and validation purposes (Mueller and Austin 1995). For *bad* data, large deviations among methods occur. The DARR-94 results do not show a clear winner among data analysis methods evaluated. It is apparent, however, that some degree of *outlier* rejection is required in order to accurately estimate $L_u(0^-, \lambda)$ or $E_d(0^-, \lambda)$. Possible solutions include manual or automated data disqualification, robust curve fitting routines, or extrapolation using the incident flux (not fully evaluated in this study). Furthermore, the calculation, evaluation and exploitation of confidence intervals for the AOP determinations needs to be explored; that is, the SeaWiFS calibration and validation problem should be recast in statistical terms where the *in situ* AOP values are statistical estimates with known confidence intervals. This is critical for the long-term assessment of ocean color imagery and its calibration and validation using *in situ* data sets. Finally, there is no substitute for *good in situ* data for accurately determining AOPs. Good at-sea procedures and clear skies are essential and cannot be over emphasized.

2. *The BBOP Data Processing System*

The BBOP group has developed a data analysis method based on the philosophy that they will take more casts then they need. For example, the BBOP collects over 1,000 profiles each year in order to link time-series observations of primary production rates to bio-optical parameters. This means suspect data will be *flagged* and eliminated from future consideration rather than corrected. A computer data processing system capable of efficiently calibrating, processing, reducing, analyzing, and interpreting the data in a timely manner is presented. The processing system is comprised of a suite of American National Standards Institute (ANSI) `C++` programs that read and operate on a specified file format, the least common denominator (LCD) data file. The LCD file contains all relevant data and metadata, which include calibration information and at-sea comments, in a single easy-to-read file that conforms to American Standard Code for Information Interchange (ASCII) standards. UNIX shell scripts are used in the control of data flow as well as error and log handling. The final product is a binned spectroradiometer data set with relevant derived parameters included [$K_d(z,\lambda)$, $R_{rs}(z,\lambda)$, $E_d(0^-, \lambda)$, etc.] that may be disseminated to other groups or databases.

3. *Integral Method for Analyzing Irradiance and Radiance Attenuation Profiles*

The CHORS group has taken a very different approach and has developed an integral method for determining the slope of the log-transformed irradiance profile, $K_d(z, \lambda)$, and its intercepts, $L_u(0^-, \lambda)$ and $E_d(0^-, \lambda)$. Their analysis goals are driven by the fact that they must make good estimates of AOPs from every cast in order to meet their own as well as their colleagues' scientific objectives. The CHORS method determines the profile of K for a vertical profile of irradiance or radiance through a least-squares fit to the optical depth profile, expressed as the integral of K from the surface to each depth z. The measured optical depth at each z is calculated as the natural logarithm of the surface-to-depth ratio of measured irradiances (or radiances). The K profile is represented analytically by Hermitian cubic polynomials connecting nodes at several discrete depths, with unknown values of K and its vertical derivative at each node as coefficients. These polynomials are integrated analytically to each z, which allows each measured optical depth to be set equal to a polynomial with node values of K and its derivative at the node depths. This results in an overdetermined set of equations corresponding to all measured depths in the irradiance (or radiance) profile, which is solved using classical least-squares methods. Prior to solution, irradiance data are normalized to minimize effects of surface irradiance variations,

and segments near major anomalies (resulting from strong cloud shadows or ship shadows) are eliminated from the fit. In contrast to the classical derivative solutions for K, the integral approach ensures a correct representation of total attenuation through missing data intervals. The CHORS method utilizes human-selected data rejection and node setting, and is developed with a sophisticated graphical user interface (GUI). It should be noted that the determination of the $L_u(0^-, \lambda)$ and $E_d(0^-, \lambda)$ values strongly affect the fit to the entire profile.

4. *Automated and Interactive Bio-Optical Processing Package*

The NRL method has been developed with the same analysis goal as the CHORS method. Namely, they need to make accurate determinations of AOPs from every cast during a cruise to achieve their science goals. NRL has developed a multiple level, prediction-correction software package called Automated and Interactive Bio-Optical Processing (AIBOP). The data is processed in two parts: first the is despiked and binned using an automated routine, and second, the effects of changes in surface illumination, ship shadow, or reflection and near surface effects (such as wave focusing) are removed using interactive spectral processing. The second level method is not used for the DARR-94 comparisons as many of the data sets used were missing required data types. Once the data is processed, routines are provided for calculating extinction coefficients, surface radiance and irradiance values, and remote sensing reflectance.

5. *The SIO Method*

For DARR-94, the SIO group employed a bulk method for deriving AOPs from spectroradiometry profiles. The bulk approach has been long employed in the past and much of what is known about AOPs has come from using this approach. The bulk method has been used in the past by the SIO group, although, they are not doing so presently. The bulk approach fits a straight line to the log-transformed irradiance and radiance profiles within the oceanic mixed layer. The fluxes just below the sea surface are estimated from the exponentiated intercept and the slope gives a mixed layer averaged diffuse attenuation coefficient, $K_d(z_0, \lambda)$. This method provides only a single estimate of $K_d(z_0, \lambda)$ and cannot be used to determine the depth dependence of $K_d(z, \lambda)$. One distinct advantage of the bulk method is that it can easily be applied using any spreadsheet program on a personal computer (PC).

Chapter 1

The First SeaWiFS Ocean Optics DARR

David A. Siegel, Margaret C. O'Brien, and Jens C. Sorensen
University of California, Santa Barbara, Santa Barbara, California

Abstract

The focus of this intercomparison study is the estimation of the downwelling irradiance spectrum just beneath the sea surface, $E_d(0^-, \lambda)$, the upwelling nadir radiance just beneath the sea surface, $L_u(0^-, \lambda)$, and the vertical profile of the diffuse attenuation coefficient spectrum, $K_d(z, \lambda)$. This study shows that with *good* data (near-constant incident irradiance), the different analyses produce estimates of $L_u(0^-, \lambda)$ and $E_d(0^-, \lambda)$ that are within 3–4% of the aggregate mean value. The statistical uncertainties in determinations of $E_d(0^-, \lambda)$ are considerably larger (approximately 7%) than those for $L_u(0^-, \lambda)$ (about 2%), as found using the BBOP analyzed results. These differences can be attributed to geophysical noise sources in the raw data streams which appear to be primarily due to the aliasing of surface wave induced glinting in the vertical radiometric profiles. Furthermore, the profile of the diffuse attenuation coefficient spectrum, $K_d(z, \lambda)$, can be replicated to better than 5% with the different analyses. These differences account for much of the total 5% uncertainty that is tolerated for SeaWiFS calibration and validation purposes (Mueller and Austin 1995). For *bad* data, large deviations among methods occur. The DARR-94 results do not show a clear winner among data analysis methods evaluated. It is apparent, however, that some degree of *outlier* rejection is required in order to accurately estimate $L_u(0^-, \lambda)$ or $E_d(0^-, \lambda)$. Possible solutions include manual or automated data disqualification, robust curve fitting routines, or extrapolation using the incident flux (not fully evaluated in this study). Furthermore, the calculation, evaluation and exploitation of confidence intervals for the AOP determinations needs to be explored. That is, the SeaWiFS calibration and validation problem should be recast in statistical terms where the *in situ* AOP values are statistical estimates with known confidence intervals. This is critical for the long-term assessment of ocean color imagery and its calibration and validation using *in situ* data sets. Last, there is no substitute for *good in situ* data for accurately determining AOPs. Good at-sea procedures and clear skies are essential and cannot be over emphasized.

1.1 INTRODUCTION

Accurate determinations of upper ocean AOPs are essential for the vicarious calibration and validation of the SeaWiFS instrument and its derived data products (McClain et al. 1992 and Mueller and Austin 1995). To date, much of the effort in the SeaWiFS CVT has been spent on the radiometric calibration of at-sea optical instrumentation and on the development of protocols for deploying them (e.g., Mueller et al. 1994 and Mueller and Austin 1995). These efforts have produced significant and important improvements in the SeaWiFS research community's ability to provide accurate AOP estimates for SeaWiFS calibration and validation, as well as algorithm development requirements. The correct deployment of accurate spectroradiometric instrumentation, however, is only the first step in making accurate determinations of AOPs.

In order to calculate AOPs using a vertically profiling spectroradiometer, a number of critical assumptions must be made concerning how the data is handled. For example, to determine the water-leaving radiance from a near-surface profile of upwelled spectral radiance, $L_u(z, \lambda)$, one must numerically extrapolate the profile from depth to just beneath the sea surface (where z=0^-). Difficulties arise due to superposition of the time course signals from surface gravity waves and random variations in package orientation, as well as ship shadows, upon the time mean upwelled radiance profile. These factors can lead to noise in spectroradiometry data. Hence, least-squares estimation methods are generally used to objectively extrapolate $L_u(z, \lambda)$ determinations to the sea surface to estimate $L_u(0^-, \lambda)$, the upwelling radiance spectrum just beneath the sea surface. This procedure has been applied by many investigators (e.g., Smith and Baker 1984, Smith and Baker 1986, Siegel and Dickey 1987, Sorensen et al. 1994, and Siegel et al. 1995a) and is recommended by the SeaWiFS Ocean Optics Protocols (Mueller and Austin 1995). However, a variety of procedural questions remain which

may impact the derived value of $L_u(0^-, \lambda)$:

1. Are $L_u(z, \lambda)$ data vertically smoothed before extrapolation to the sea surface?
2. Is the data binned vertically before calculating $L_u(0^-, \lambda)$?
3. How are ship shadows excluded?
4. How is a surface sensor used if one is available?
5. What effect(s) do these decisions have on an estimate of $L_u(0^-, \lambda)$?
6. How about other important AOPs?

To evaluate the role that data analysis methods have upon values of derived AOPs, the DARR-94 workshop was sponsored by the SeaWiFS Project Office during July 21–23, 1994 at ICESS (UCSB). Four research groups used their *standard* spectroradiometer data analysis routines (Table 1) on an identical data set of 10 spectroradiometry casts. The goal of DARR-94 was to assess the degree to which data analysis methods affect AOP estimation and to make general recommendations where applicable. This assessment is critical as fully processed spectroradiometry data will be used to calibrate and validate the SeaWiFS satellite data stream. Hence, the direct comparisons of the results of the four data analysis methods will put some bounds on the degree of certainty for AOP estimates and their effects upon the calibration and validation of the upcoming SeaWiFS ocean color mission.

Table 1. A listing of data contributors for DARR-94 along with their methods and primary study sites.

Contact	*Method*	*Primary Site*
D. Siegel	Differential†	JGOFS BATS TOGA COARE
J. Mueller	Integral	Gulf of Mexico Gulf of California
C. Davis	Differential‡	JGOFS EqPac Arabian Sea
G. Mitchell	Bulk	CalCoFI

† With confidence intervals and quality flags.

‡ With sea surface and surface irradiance adjustments.

This study evaluates and documents the magnitude of uncertainty in derived estimates of ocean color relevant AOPs due to differences in data analysis methods. In particular, estimates of the spectrum of upwelling radiance and downwelling irradiance just beneath the sea surface, $L_u(0^-, \lambda)$ and $E_d(0^-, \lambda)$, respectively, and the vertical profile of the diffuse attenuation coefficient spectrum, $K_d(z, \lambda)$, are considered in detail. The approach taken for the DARR-94 is rather simple. Each of the four research groups (Table 1) provided up to three spectroradiometry casts (discussed below) and each group analyzes the data to relevant AOPs. The resulting values of $L_u(0^-, \lambda)$ and $E_d(0^-, \lambda)$ and vertical profiles of $K_d(z, \lambda)$ are compared and relevant conclusions presented. All raw data and analyzed products are available using the anonymous file transfer protocol (ftp):

```
ftp.icess.ucsb.edu
cd pub/bbop/DARR-94/data
```

or from the SeaWiFS Project Office data system (Hooker et al. 1994).

Since the scope of this first data analysis intercomparison study (DARR-94) has been purposely limited, the present results will obviously have several inherent limitations:

1. The methods are compared for a limited amount of data (9 casts) over a small range of environmental conditions. These data are for the mostly Case-1 waters (Table 2) and will not cover all possible observational scenarios.
2. It is not known which method (if any) is providing the *right* answer as these are field data sets. Clearly, if all four methods coincide, the differences amongst the methods applied can be assumed unimportant; however if their results diverge, it remains unclear which method is right and which is wrong.
3. A variety of correction procedures, which may be important for accurately determining AOPs, were not evaluated. These include corrections for Raman emissions, instrument self-shading, gimballing (or not) of surface irradiance sensors, tilt corrections for underwater spectroradiometer signals, and propagating the $L_u(0^-, \lambda)$ and $E_d(0^-, \lambda)$ through the air-sea interface. All of these corrections may be important although they are not assessed here in an effort to simplify the goals of the DARR. It is likely that these corrections will be examined, along with a more extensive data set, in future DARR workshops. The use of synthetic data sets may also prove to be useful.

It should be stressed that the goal of the DARR-94 workshop was not to codify a single *recipe* by which data must be processed for SeaWiFS calibration and validation needs. This recipe is unknown and there are many factors, involving instrumentation, data acquisition, at-sea deployment procedures, and the analysis goals of the investigation, which make it difficult to provide a simple recipe for all investigators and all applications. That task is clearly beyond a three-day workshop. Nonetheless, an attempt is made to make generalities concerning what should and should not be done in analyzing spectroradiometry profiles. Furthermore, the conclusion is reached that the determination of AOPs should be cast as a stochastic problem where statistical estimates are made with assessible confidence limits. This approach is critical for achieving SeaWiFS calibration and validation goals.

1.2 DATA ANALYSIS METHODS

The present objective is to assess the differences among four different data analysis methodologies when applied to identical spectroradiometry data. All of the methods are presently used in the field and will be utilized by the CVT (McClain et al. 1992). Complete descriptions for each data analysis method are presented in subsequent chapters. Here, only a brief introduction of each method is presented. It should be mentioned that code (both source and executable) for most of the data analysis methods are available via anonymous ftp (see the authors of the individual chapters involved).

The four methods have been developed with very different design objectives which are primarily specified by the science goals and logistical limitations of each group's at-sea sampling programs (Table 1). For example, the method employed by the BBOP (Chapter 2) has been designed to deal with large volumes of data (as many as 70 casts from a single day and over 2,000 casts a year). The design philosophy is that bad data are flagged and discarded rather than *corrected*. On the other hand, investigators at CHORS have developed an integral method for determining AOPs with the ability to hand select *spurious* data points. This design goal is predicated by inherent wire-time limitations due to large multidisciplinary cruises in which the CHORS group participates. These design goals reflect the at-sea sampling opportunities available to each group. The data analysis methods are each group's solution to these problems while optimizing their science objectives.

The BBOP group has developed a data analysis method with the data analysis philosophy that they will take more casts than they need (Chapter 2, Sorensen et al. 1994, Siegel et al. 1995a, and Siegel et al. 1995b). This means suspect data will be eliminated from future consideration rather than corrected. Thus, the BBOP data processing system produces quality flags and is able to routinely handle large volumes of data, which requires that nearly all of the processing steps be completed with little human intervention. The *suspect* data condition is determined by evaluating a variety of predetermined quality flags (stability of incident irradiance levels, tilt and roll limitations, etc.) as well as the calculation of statistical confidence limits for most derived products. Relevant to the present intercomparison study, the BBOP data processing system estimates the values of $L_u(0^-, \lambda)$ and $E_d(0^-, \lambda)$ by fitting a straight line to the upper 20 meters of a profile (10 m for $\lambda > 600$ nm). The vertical profile of $K_d(z, \lambda)$ is determined using a differential method where least-square fits are applied over 10 m vertical intervals. Robust curve fitting algorithms are used to reduce the effects of spurious data points or *outliers* (Press et al. 1992); also, confidence intervals for estimates of $L_u(0^-, \lambda)$ and $E_d(0^-, \lambda)$ are determined. The BBOP processing system runs on UNIX workstation computers and requires a GNU `C++` compiler and a GUI package, such as Matlab or Interactive Data Language (IDL). For more information concerning acquiring the BBOP system see Chapter 2 or Siegel et al. (1995b).

The CHORS group has taken a very different approach and has developed an integral method for determining the slope of the log-transformed irradiance profile, $K_d(z, \lambda)$, and its intercepts, $L_u(0^-, \lambda)$ and $E_d(0^-, \lambda)$ (Chapter 3). Their analysis goals are driven by the fact that they must make good estimates of AOPs from every cast in order to meet their own, as well as their colleagues', scientific objectives. The CHORS method determines the profile of $K_d(z, \lambda)$ and values of $L_u(0^-, \lambda)$ and $E_d(0^-, \lambda)$ simultaneously using an integral method by fitting the radiation profile using low-order polynomials between user-selected node locations. The node locations may be determined initially by examining a companion chlorophyll fluorescence profile, or if one is not present, by examination of curvature in the radiometric profile. The number and depths of nodes are then iteratively adjusted to minimize systematic departures between the modeled and measured profile curves. Values of $K_d(z, \lambda)$ are determined analytically from the fitted polynomials. The CHORS method utilizes human-selected data rejection and node setting, and is developed with a sophisticated GUI. It should be noted that the determination of the $L_u(0^-, \lambda)$ and $E_d(0^-, \lambda)$ values strongly affect the fit to the entire profile. The CHORS method presently runs on Silicon Graphics Inc. (SGI) workstations under IRIX 4.0 and higher.

The NRL method (Chapter 4) has been developed with the same analysis goal as the CHORS method; namely, the need to make accurate determinations of AOPs from every cast during a cruise to achieve the science goals. NRL has employed a multiple level, prediction-correction procedure for estimating AOPs. The first level utilizes a differential approach to make first order estimates of AOPs and is fully automated. The second level employs a series of correction procedures and modeling to affect a robust surface normalization evaluating the $z = 0^-$ and $z = 0^+$ difference in an interactive mode through a sophisticated GUI. This surface normalization is done in order to eliminate the effects of changing solar illumination due to clouds, as well as a correction procedure for the potential effects of ship shadowing and hull reflection. The second level method is not used for the DARR-94 comparisons as many of the data sets used were missing required data types. The NRL method works on UNIX workstations using the IDL software package.

The SIO group has employed a bulk method for deriving AOPs from spectroradiometry profiles (Chapter 5). The bulk approach has been long employed in the past and much of what is known about AOPs has come from using this approach (e.g., Strickland 1958, Tyler and Smith 1970, Smith and Baker 1978a and 1978b, and Morel 1988). The bulk method has been used in the past by the SIO group (e.g., Mitchell and Holm-Hansen 1991), although, they are not doing so presently. The bulk approach fits a straight

Table 2. Geolocation and sky conditions for data files compared in DARR-94.

Group	*File*	*Priority*	*Location*	*Station*	*Longitude*	*Latitude*	*Sky*
BBOP	a010992b.dn	1	Sargasso	BATS	64°44.20 W	31°23.61 N	Haze
	a061792f.dn	1	Sargasso	BATS	64 18.24	31 30.40	8/8 Stratus
	a082092c.dn	1	Sargasso	BATS	64 7.84	31 50.99	2/8 Cumulus
CHORS	04111945.dn	2	GOMEX	611	89 59.88	28 30.12	Clear
	04111700.dn	2	GOMEX	510	90 0.00	28 45.12	Clear
	04141407.dn	1	GOMEX	1625	89 27.48	28 30.48	Patchy Clouds
NRL	e920328a.dn	1	EqPac	5	139 57.90	0 1.80	Overcast
	e921016a.dn	1	EqPac	5	140 2.09	0 1.69	Clear
SIO	c0403d.up	1	CalCoFI		122 40.40	31 5.30	
	c0411g.up	2	CalCoFI		121 10.30	34 7.30	

Table 3. Temporal and in-water parameters for files compared in DARR-94. The maximum depth of the profile is given by $z_{\max}$ and the mixed layer depth by z_{mld}.

Group	*File*	*Priority*	*Date*	*Local Time*	$z_{\max}$	z_{mld}	*Notes*
BBOP	a010992b.dn	1	9 Jan 92	1600	200 m	100 m	Late afternoon (sunset).
	a061792f.dn	1	17 Jun 92	1000	200	20	
	a082092c.dn	1	20 Aug 92	1100	200	30	Clear overhead.
CHORS	04111945.dn	2	11 Apr 93	1345	80		Surface and bottom nephels.
	04111700.dn	2	11 Apr 93	1100	30		Dark at 22 m ($K \approx 1.4\,\mathrm{m}^{-1}$).
	04141407.dn	1	14 Apr 93	0800	200		Deep water, clouds.
NRL	e920328a.dn	1	16 Oct 92	1000	180	90	Variable overcast.
	e921016a.dn	1	28 Mar 92	1000	200	70	Ship shadow?
SIO	c0403d.up	1	3 Apr 93	0928	200	60	Ship shadow, no surface.
	c0411g.up	2	11 Apr 93	1325	200	10	Good data to 30 m.

line to the log-transformed irradiance and radiance profiles within the oceanic mixed layer. The fluxes just below the sea surface are estimated from the exponentiated intercept and the slope gives a mixed layer averaged diffuse attenuation coefficient, $K_d(z_0, \lambda)$. Obviously, only a single estimate of $K_d(z_0, \lambda)$ is provided by this method; hence, it cannot be used to determine the depth dependence of $K_d(z, \lambda)$. The bulk method is included in the DARR-94 as an *experimental control* providing a single analysis from which one can interpret differences among the other methods. One distinct advantage of the bulk method is that it can easily be applied using any spreadsheet program on a PC.

There are significant differences among the four data analysis methods due to differing scientific objectives and at-sea logistics of the individual research groups. For the most part, differences among the data analysis methods are due to the way each group collects data at sea. The sampling philosophy for BBOP is based upon the understanding that not every cast will produce good AOPs. The CHORS and NRL groups must be able to interact with other researchers on synoptic survey cruises and, hence, must determine AOPs for every daytime cast made. Thus, the CHORS and NRL groups have developed extensive surface normalization and correction procedures. The BBOP method assumes bad data can never be made into good data and, therefore, rejects AOP determinations based upon quality flags and the size of confidence intervals. The bulk method (SIO) completes the methods evaluated and is presented in a historical context from which an evaluation of the degree of improvement made by the other more sophisticated data analysis methods can be made.

1.3 DATA AND RESULTS

1.3.1 The DARR-94 Data Set

A summary of the spectroradiometry data files and basic environmental conditions for these files used in the DARR-94 is shown in Tables 2 and 3. The files are labeled with a priority number of 1 or 2 based upon whether these profiles provide adequate light data deep in the sampled water column. In some sense, priority 1 casts correspond to open ocean conditions in that the good data are found throughout the vertical profile and no anomalous features are observed, i.e., extremely high $K_d(z, \lambda)$ values, nepheloid layers, etc. Using this criteria, there are seven priority 1 profiles from which comparisons of data analysis methods are made. The priority 2 data appear to be mostly Case-2 water casts; hence, the primary comparisons made using the DARR-94 data set will be valid primarily for open ocean conditions using the priority 1 data set.

Unprocessed vertical profiles of $E_d(z, 488)$, $L_u(z, 488)$, $E_d(0^+, 488)$,temperature, and *in situ* chlorophyll fluorescence used in DARR-94 are shown in Figs. 1–10. Note that not all of parameters are sampled for each cast. In particular, there are no temperature or chlorophyll fluorescence data for the CHORS casts (CHORS `04111945`, `04111700`, and `04141407`) nor are there surface radiation measurements made with the SIO data set (`c0403d` and `c0411g`; the CHORS analysis was applied assuming the incident irradiance was constant). It must be stressed that the data provided here are not the *best* data collected by the contributing research group, but rather the data represent typical data collected from the field. Indeed, some casts were selected to demonstrate how data analysis methods deal with bad data. Obviously, bad casts are not useful for making AOP determinations for SeaWiFS calibration and validation purposes.

It is apparent that there is a wide range of profile shapes in the aggregate DARR-94 data set. Water columns with deep chlorophyll maxima are found (BBOP `a061792f` and `a082092c`, NRL `e921016a`, and SIO `c0403d`) where the depth of chlorophyll fluorescence maximum varies from approximately 50 m (NRL `e921016a`) to more than 125 m (BBOP `a082092c`). Casts with high chlorophyll values in the near surface layer are also found (BBOP `a010992b`, NRL `e920328a`, and SIO `c0411g`). It is obviously difficult to make this determination from the CHORS data as there are no chlorophyll fluorescence data. Also, mixed layer depths of the DARR-94 data files vary from 10 to more than 100 m (Table 3). For the most part, the profiles are taken under excellent incident illumination conditions. The obvious exceptions are the low light conditions of BBOP `a010992b`, which was taken at sunset, and the extreme incident irradiance variability found in the CHORS `04141407` cast. Again, these distinctions cannot be made using the SIO casts, since incident irradiance is not included in the data; hence, a wide range of conditions are represented by the DARR-94 data set, although they are by no means inclusive.

The upper 30 m of the downwelling irradiance, $E_d(z, \lambda)$, and upwelling radiance, $L_u(z, \lambda)$ profiles are of particular relevance for assessing AOPs for SeaWiFS calibration and validation purposes (Figs. 1–10). Within this depth region, the intercept values, $L_u(0^-, \lambda)$ and $E_d(0^-, \lambda)$, are determined using a statistical method (such as least-squares estimation). If stable values of $L_u(0^-, \lambda)$ and $E_d(0^-, \lambda)$ are to be retrieved, the log-transformed $E_d(z, \lambda)$ and $L_u(z, \lambda)$ profiles must be found along a straight line. The raw $E_d(z, \lambda)$ and $L_u(z, \lambda)$ profiles show a significant degree of variation off this assumed straight line (Figs. 1–10). Furthermore, the variance about a *straight line* appears to increase as the sea surface is approached and is greater for $E_d(z, \lambda)$ than for $L_u(z, \lambda)$. There are a variety of causes for these variations, including, ship shadow and hull reflection, surface gravity wave-induced glint and focusing, random tilting of the profiling spectroradiometer off zenith, as well as cloud-induced fluctuations of the incident irradiance (which may affect a profile of light at any depth).

Large near-surface radiation variations in radiometric profiles may also result from strong, vertically stratified region of increased attenuation by particles and dissolved materials in the water column. In the CHORS `04111945` cast, for example, both the $E_d(z, \lambda)$ and $L_u(z, \lambda)$ profiles show a strongly nonlinear decrease with depth over the top 5 m. This profile was taken near the Mississippi River outflow, and the highly turbid surface lay responsible for large values of $K_d(z, \lambda)$ for both $E_d(z, \lambda)$ and $L_u(z, \lambda)$ are of Mississippi River origin. However for most of the other casts, the high degree of near-surface $E_d(z, \lambda)$ and $L_u(z, \lambda)$ variations is not due to changes in optical water masses, but rather to random sources of irradiance noise within the profile. Ship-induced sources of noise (i.e., ship shadows) are apparent in some of the profiles (cf., NRL `e921016a` and SIO `c0403d`). Note that for the BBOP data, the ship shadow signal has been shown to be smaller than other inherent sources of noise in the estimation of AOPs (Weir et al. 1994).

1.3.2 Near-Surface Data Comparisons

Central to the agreed upon goals of DARR-94 was the comparison of estimates of the downwelling irradiance and the upwelling radiance spectra just beneath the sea surface ($z = 0^-$), $E_d(0^-, \lambda)$ and $L_u(0^-, \lambda)$ respectively. Estimates of $E_d(0^-, \lambda)$ and $L_u(0^-, \lambda)$ for the four individual analyses of the priority 1 data set and their aggregate statistics are presented in Figs. 11–17. A casual examination of the $E_d(0^-, \lambda)$ and $L_u(0^-, \lambda)$ estimates illustrates several generalities concerning the abilities to make accurate determinations of $E_d(0^-, \lambda)$ and $L_u(0^-, \lambda)$ from spectroradiometry profiles:

1. The variations among the various methods is greater for $E_d(0^-, \lambda)$ than for $L_u(0^-, \lambda)$.
2. This difference is accentuated in the red wavelengths.
3. The spread among the individual $E_d(0^-, \lambda)$ estimates is mostly smaller than the size of the 95% confidence interval for the BBOP estimate; although, at times, there are exceptions (BBOP `a010992b`).
4. The simple least-squares methods employed by the SIO group appears to be the onle one of the four methods that consistently produces outlier estimates of $E_d(0^-, \lambda)$ and $L_u(0^-, \lambda)$. This is particularly apparent in the red wavelengths.
5. The spread among the differing $E_d(0^-, \lambda)$ and $L_u(0^-, \lambda)$ estimates does not appear to be related to the clarity of the water as inferred by the estimated color, $L_u(0^-, \lambda)$.

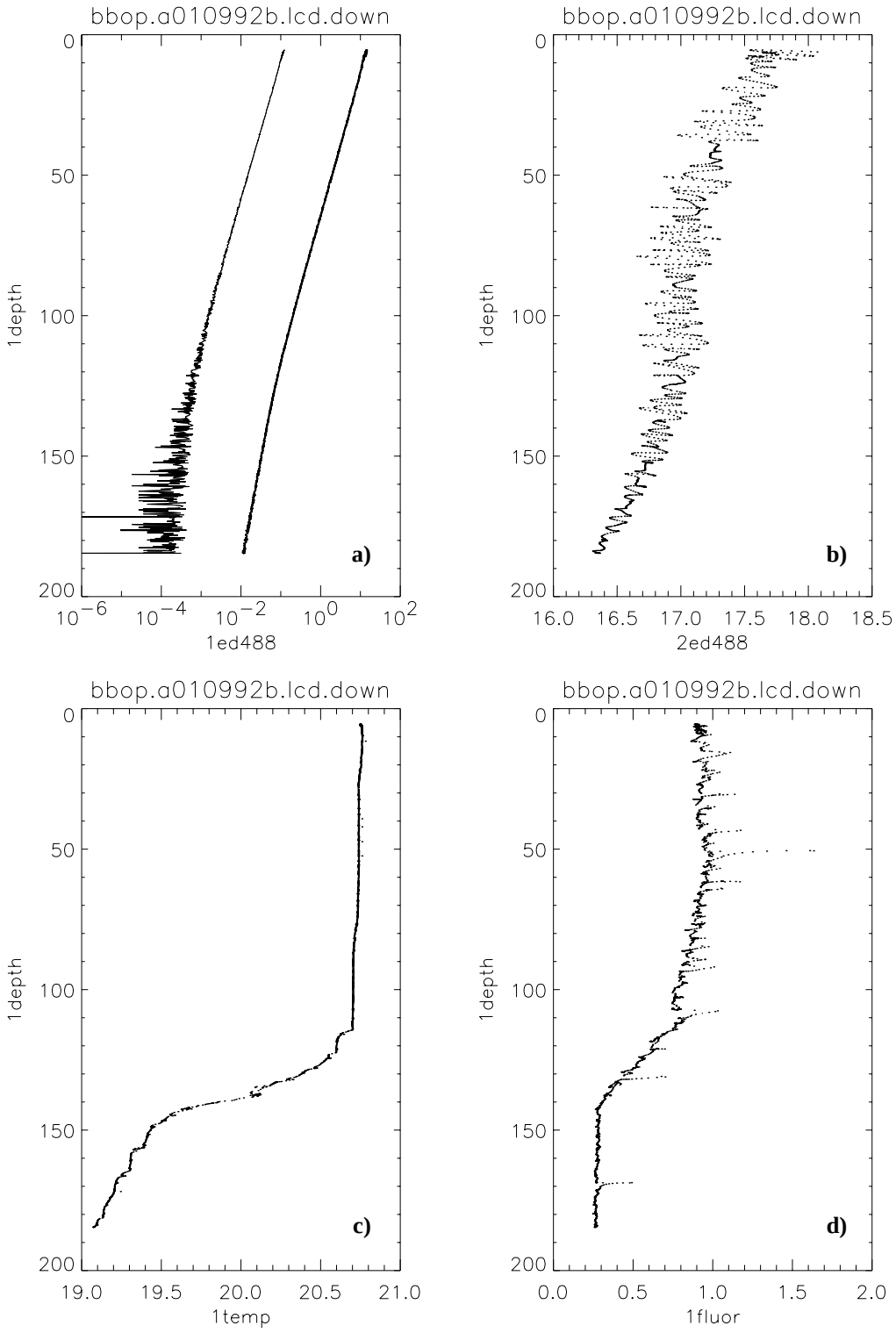

Fig. 1. Vertical profiles of the raw data used in the DARR-94 comparison for BBOP `a010992b`. The four panels for each vertical distribution are assembled: **a)** downwelling irradiance at 488 nm and upwelling radiance at 488 nm, $E_d(z, 488)$ (in units of $\mathrm{mW\,cm^{-2}\,nm^{-1}}$) and $L_u(z, 488)$ ($\mathrm{mW\,cm^{-2}\,nm^{-1}\,sr^{-1}}$), respectively; **b)** the incident irradiance at 488 nm during the time of the cast, $E_d(0^+, 488)$; **c)** *in situ* temperature (°C); and **d)** chlorophyll fluorescence (in volts).

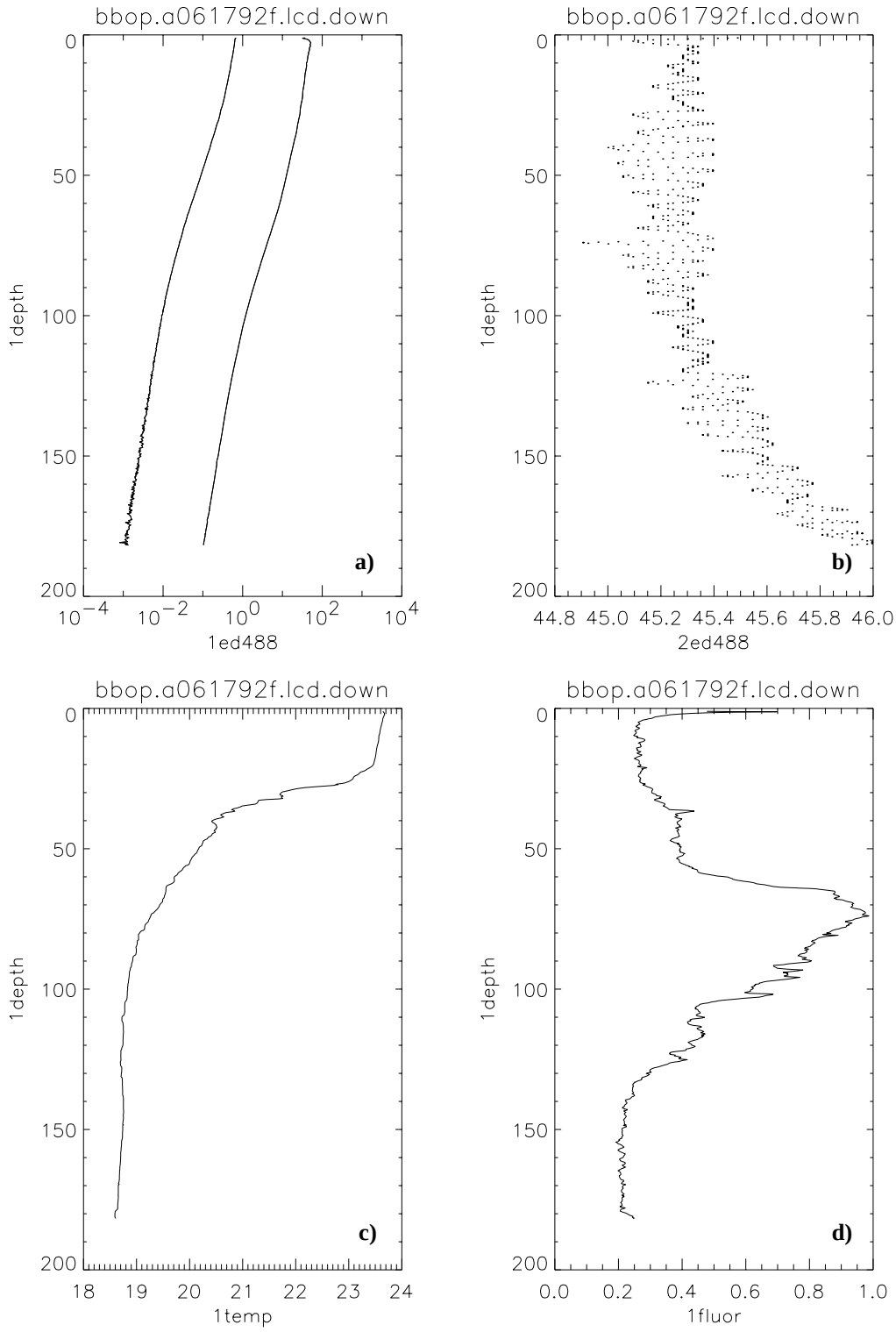

Fig. 2. Vertical profiles of the raw data used in the DARR-94 comparison for BBOP `a061792f`. The four panels for each vertical distribution are assembled: **a)** downwelling irradiance at 488 nm and upwelling radiance at 488 nm, $E_d(z, 488)$ (in units of $\mathrm{mW\,cm^{-2}\,nm^{-1}}$) and $L_u(z, 488)$ ($\mathrm{mW\,cm^{-2}\,nm^{-1}\,sr^{-1}}$), respectively; **b)** the incident irradiance at 488 nm during the time of the cast, $E_d(0^+, 488)$; **c)** *in situ* temperature (°C); and **d)** chlorophyll fluorescence (in volts).

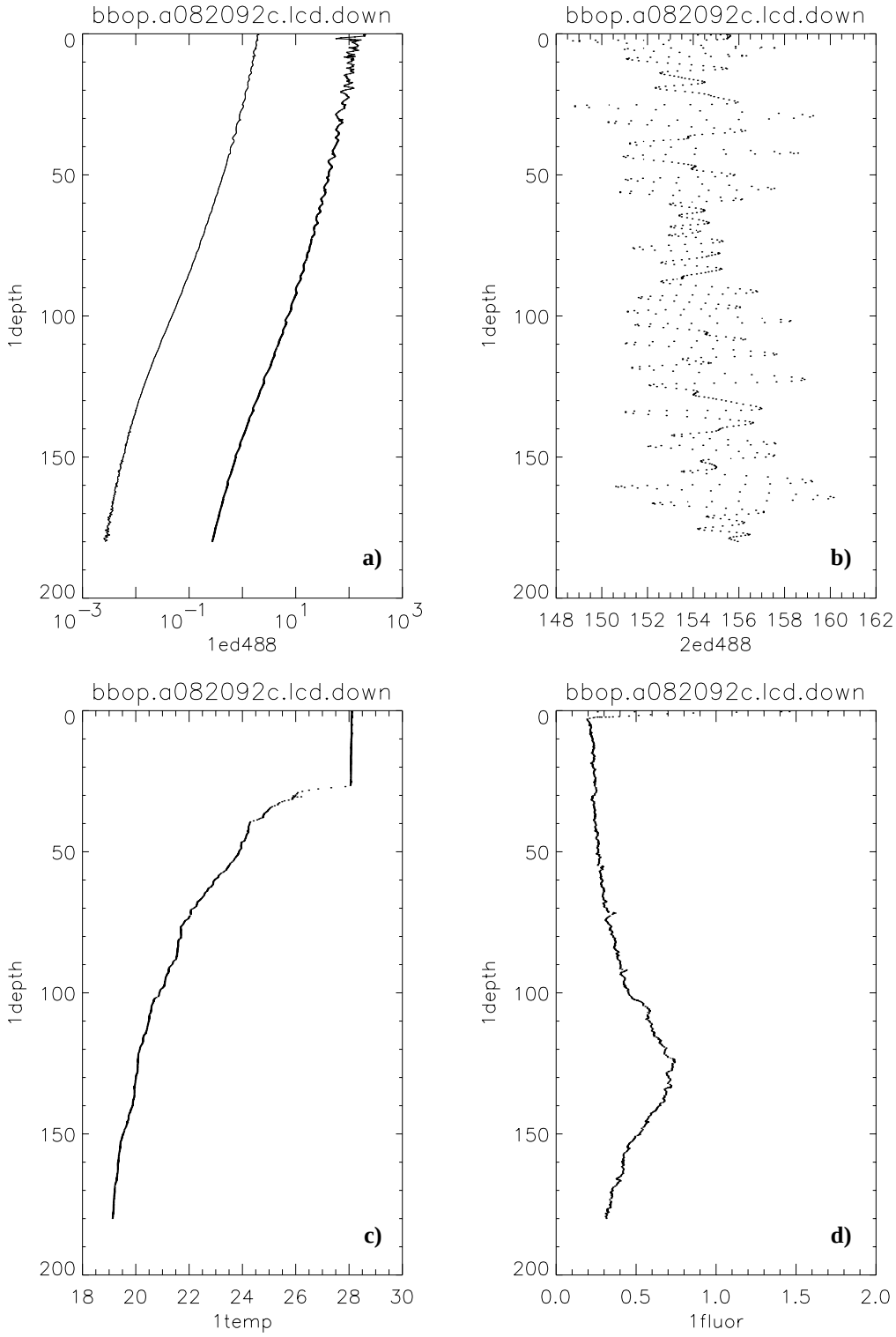

Fig. 3. Vertical profiles of the raw data used in the DARR-94 comparison for BBOP `a082092c`. The four panels for each vertical distribution are assembled: **a)** downwelling irradiance at 488 nm and upwelling radiance at 488 nm, $E_d(z, 488)$ (in units of mW cm^{-2} nm^{-1}) and $L_u(z, 488)$ (mW cm^{-2} nm^{-1} sr^{-1}), respectively; **b)** the incident irradiance at 488 nm during the time of the cast, $E_d(0^+, 488)$; **c)** *in situ* temperature (°C); and **d)** chlorophyll fluorescence (in volts).

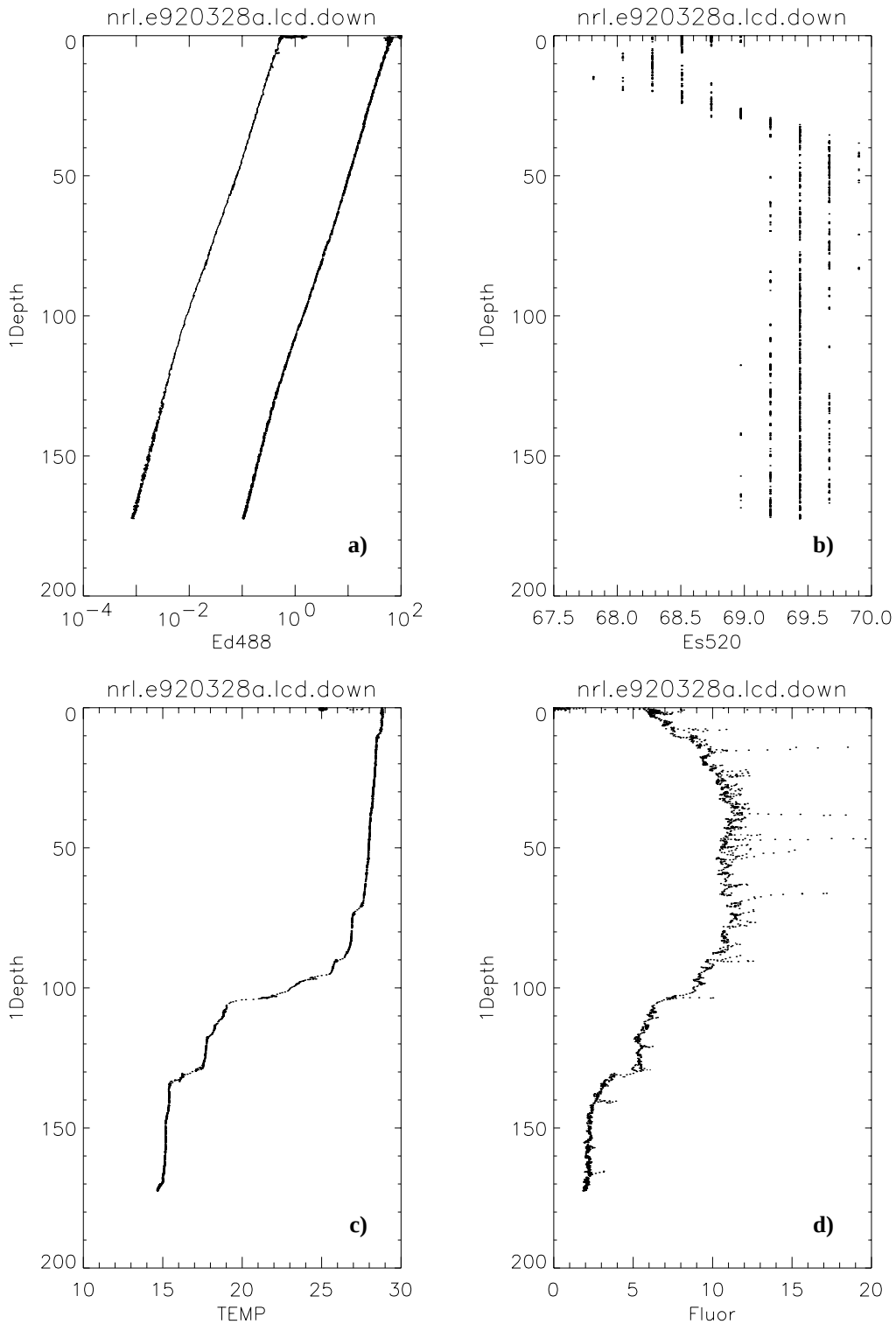

Fig. 4. Vertical profiles of the raw data used in the DARR-94 comparison for NRL `e920328a`. The four panels for each vertical distribution are assembled: **a)** downwelling irradiance at 488 nm and upwelling radiance at 488 nm, $E_d(z, 488)$ (in units of $\mathrm{mW\,cm^{-2}\,nm^{-1}}$) and $L_u(z, 488)$ ($\mathrm{mW\,cm^{-2}\,nm^{-1}\,sr^{-1}}$), respectively; **b)** the incident irradiance at 488 nm during the time of the cast, $E_d(0^+, 488)$; **c)** *in situ* temperature (°C); and **d)** chlorophyll fluorescence (in volts).

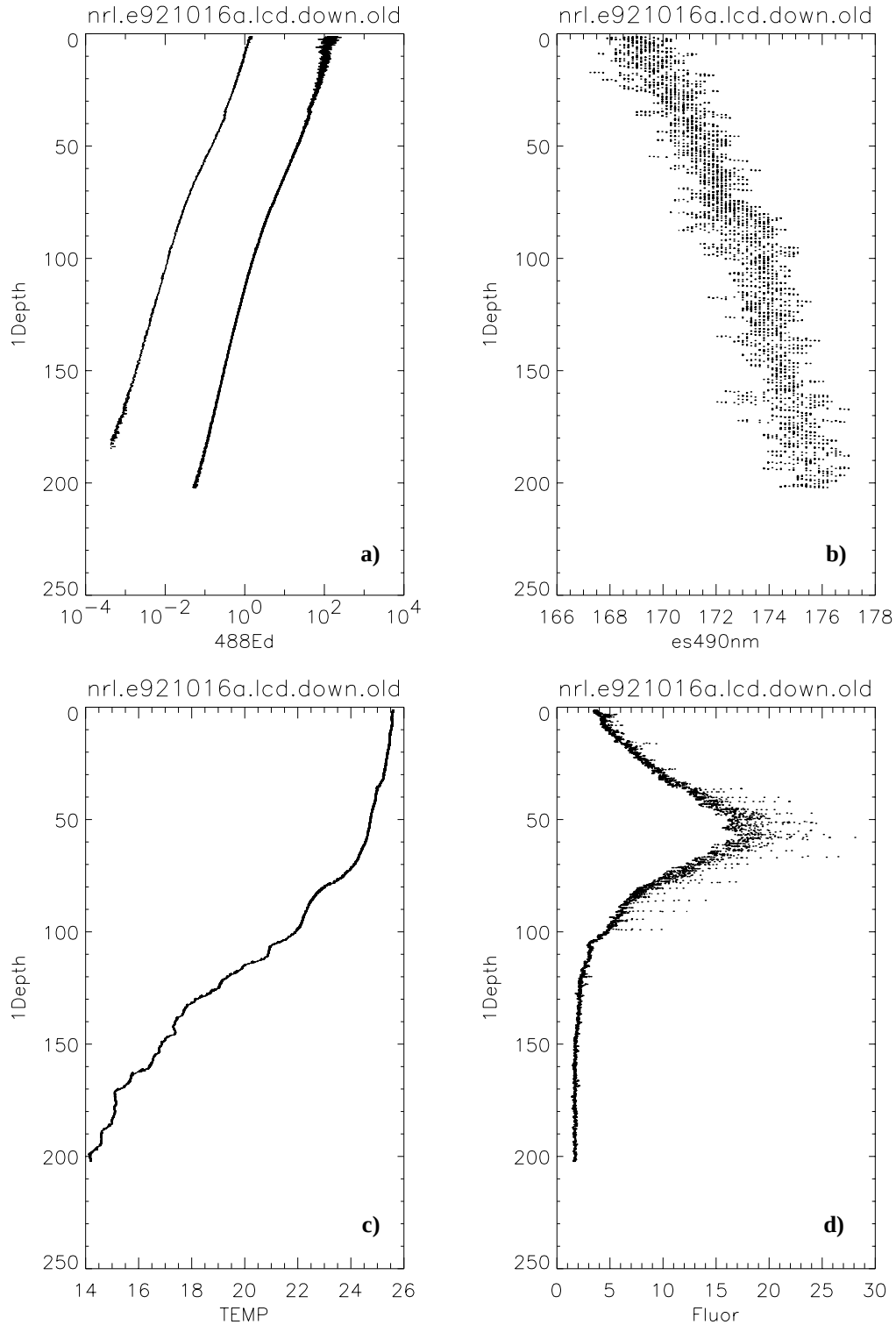

Fig. 5. Vertical profiles of the raw data used in the DARR-94 comparison for NRL `e921016a`. The four panels for each vertical distribution are assembled: **a)** downwelling irradiance at 488 nm and upwelling radiance at 488 nm, $E_d(z, 488)$ (in units of $\mathrm{mW\,cm^{-2}\,nm^{-1}}$) and $L_u(z, 488)$ ($\mathrm{mW\,cm^{-2}\,nm^{-1}\,sr^{-1}}$), respectively; **b)** the incident irradiance at 488 nm during the time of the cast, $E_d(0^+, 488)$; **c)** *in situ* temperature (°C); and **d)** chlorophyll fluorescence (in volts).

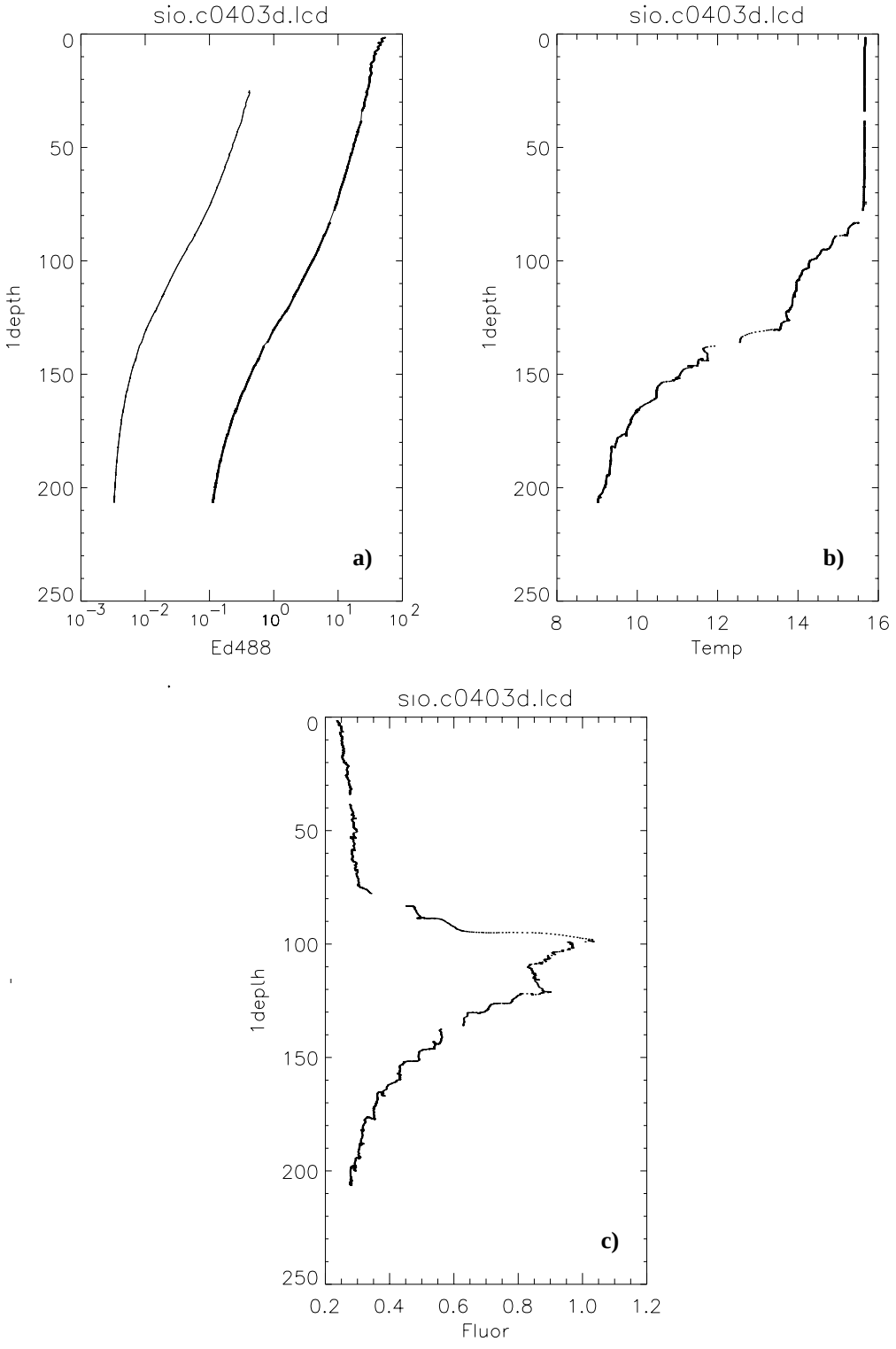

Fig. 6. Vertical profiles of the raw data used in the DARR-94 comparison for SIO `c0403d`. The three panels for each vertical distribution are assembled: **a)** downwelling irradiance at 488 nm and upwelling radiance at 488 nm, $E_d(z, 488)$ (in units of $\mathrm{mW\,cm^{-2}\,nm^{-1}}$) and $L_u(z, 488)$ ($\mathrm{mW\,cm^{-2}\,nm^{-1}\,sr^{-1}}$), respectively; **b)** *in situ* temperature (°C); and **c)** chlorophyll fluorescence (in volts).

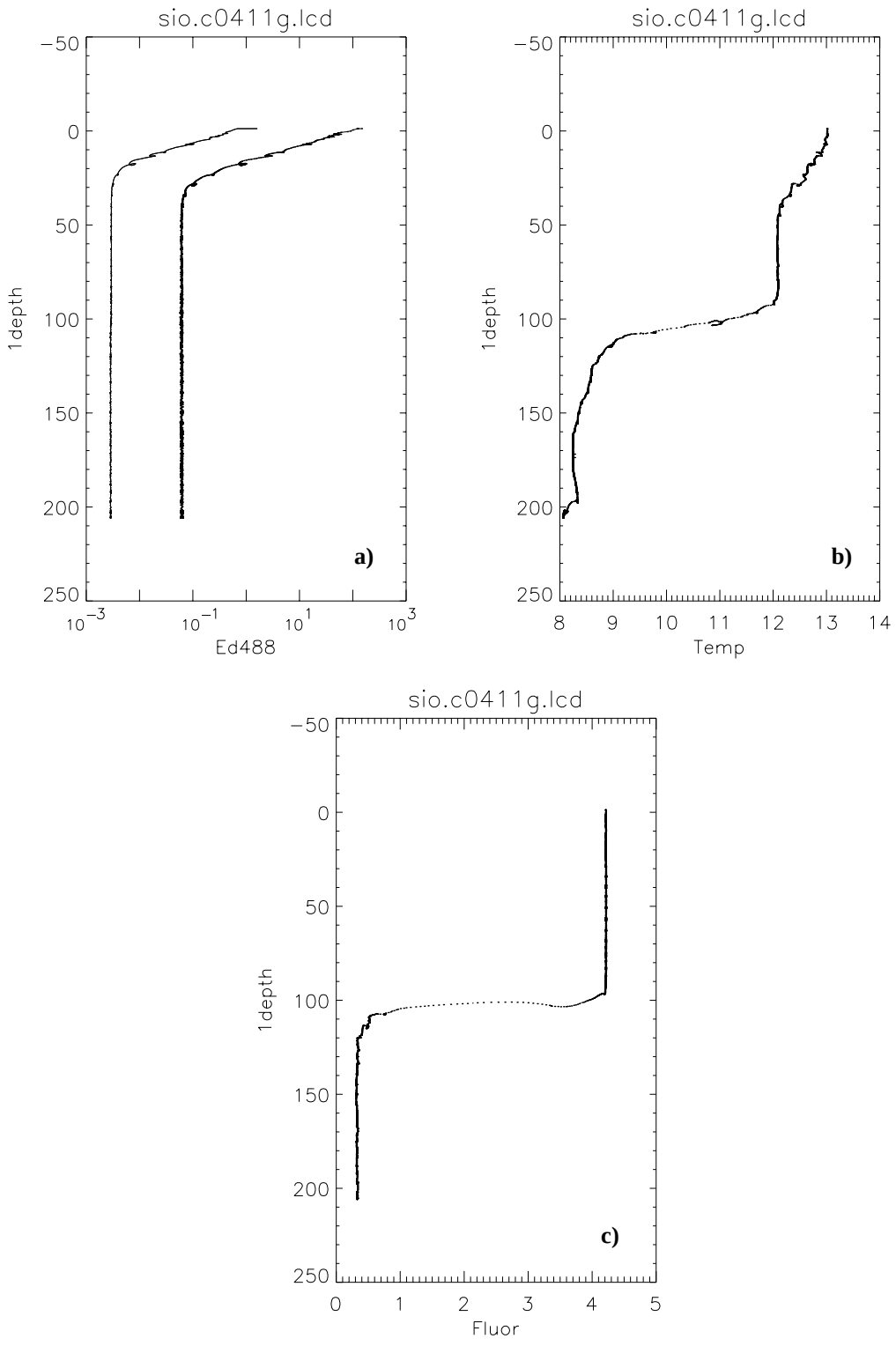

Fig. 7. Vertical profiles of the raw data used in the DARR-94 comparison for SIO `c0411g`. The three panels for each vertical distribution are assembled: **a)** downwelling irradiance at 488 nm and upwelling radiance at 488 nm, $E_d(z, 488)$ (in units of $\mathrm{mW\,cm^{-2}\,nm^{-1}}$) and $L_u(z, 488)$ ($\mathrm{mW\,cm^{-2}\,nm^{-1}\,sr^{-1}}$), respectively; **b)** *in situ* temperature (°C); and **c)** chlorophyll fluorescence (in volts).

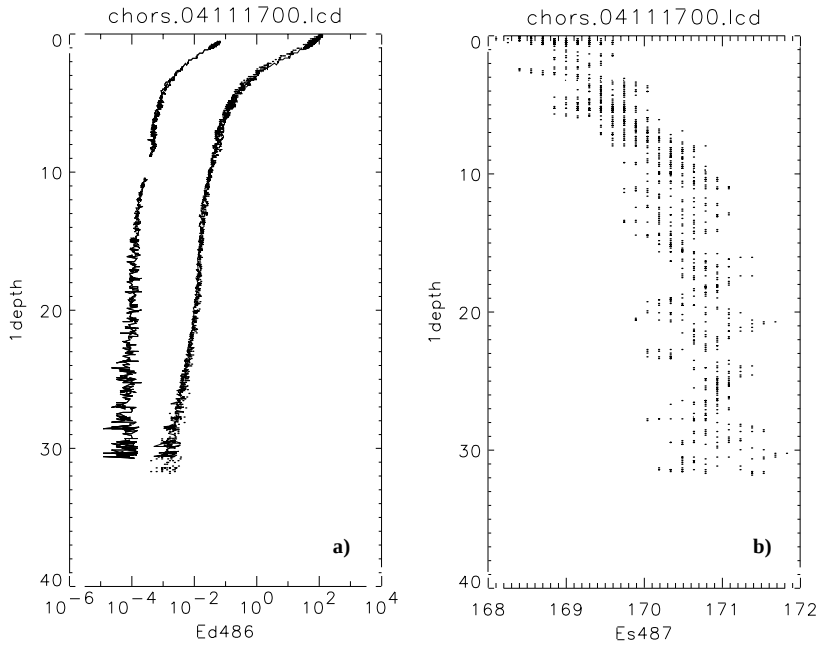

Fig. 8. Vertical profiles of the raw data used in the DARR-94 comparison for CHORS `04111700`. The two panels for each vertical distribution are assembled: **a)** downwelling irradiance at 486 nm and upwelling radiance at 486 nm, $E_d(z, 486)$ (in units of $\mathrm{mW\,cm^{-2}\,nm^{-1}}$) and $L_u(z, 486)$ ($\mathrm{mW\,cm^{-2}\,nm^{-1}\,sr^{-1}}$), respectively; **b)** the incident irradiance at 487 nm during the time of the cast, $E_s(0^+, 487)$.

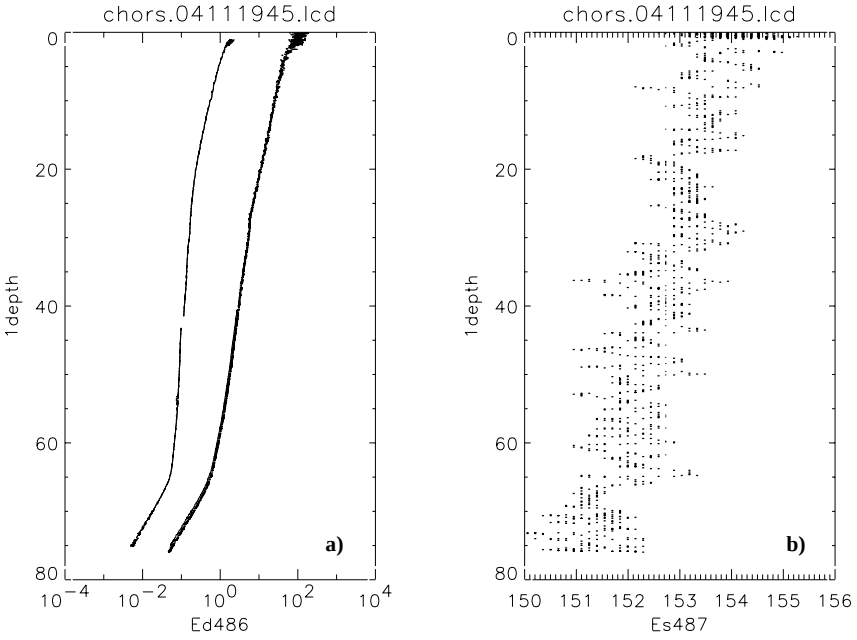

Fig. 9. Vertical profiles of the raw data used in the DARR-94 comparison for CHORS `04111945`. The two panels for each vertical distribution are assembled: **a)** downwelling irradiance at 486 nm and upwelling radiance at 486 nm, $E_d(z, 486)$ (in units of $\mathrm{mW\,cm^{-2}\,nm^{-1}}$) and $L_u(z, 486)$ ($\mathrm{mW\,cm^{-2}\,nm^{-1}\,sr^{-1}}$), respectively; **b)** the incident irradiance at 487 nm during the time of the cast, $E_s(0^+, 487)$.

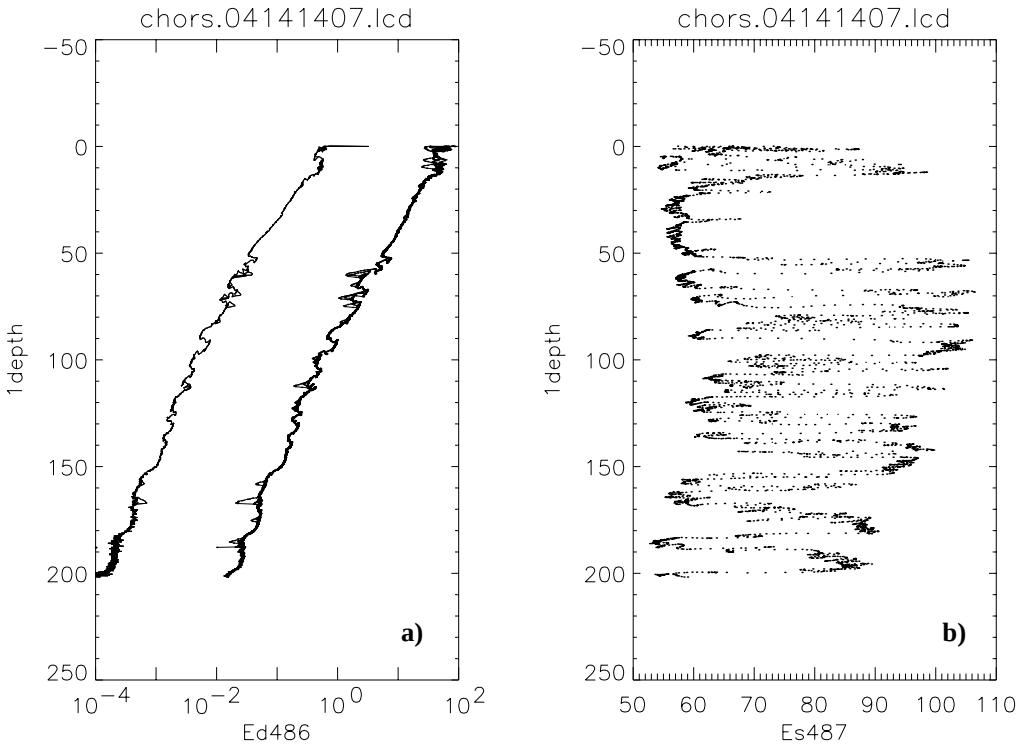

Fig. 10. Vertical profiles of the raw data used in the DARR-94 comparison for CHORS `04141407`. The two panels for each vertical distribution are assembled: **a)** downwelling irradiance at 486 nm and upwelling radiance at 486 nm, $E_d(z, 486)$ (in units of mW cm^{-2} nm^{-1}) and $L_u(z, 486)$(mW cm^{-2} nm^{-1} sr^{-1}), respectively; **b)** the incident irradiance at 487 nm during the time of the cast, $E_s(0^+, 487)$.

A quantitative evaluation of the differing $E_d(0^-, \lambda)$ and $L_u(0^-, \lambda)$ estimates may be made by examining the coefficient of variation (c.v.) among the four analyses for each priority 1 cast. Values of c.v. (in percentages) for the priority 1 DARR-94 casts are shown in Table 4. Only overlapping wavebands are shown in Table 4 (where $L_u(0^-, 530)$ is substituted for $L_u(0^-, 520)$ in the CHORS data). Typical c.v. values range from about 1–8%. When all of the priority 1 data are evaluated, mean c.v. values are slightly lower for $E_d(0^-, \lambda)$ estimates than they are for $L_u(0^-, \lambda)$. Of the individual casts, the CHORS data file `04141407` is by far the worst of the priority 1 casts, especially for $L_u(0^-, \lambda)$. This is expected as this cast had extensive cloud-induced incident irradiance variations (Fig. 10). When this cast is removed from consideration (the *EC* values in Table 4), the DARR-94 mean c.v. values are around 3–4% with no significant difference between the $L_u(0^-, \lambda)$ and $E_d(0^-, \lambda)$ estimates; hence, the scatter of the results of the four analyses about the analysis aggregate mean for good casts is less than 4% of the retrieved value.

The comparison of the relative size of the 95% confidence intervals for the BBOP determined $E_d(0^-, \lambda)$ and $L_u(0^-, \lambda)$ provides another objective measure of the degree to AOPs can be accurately determined. Here, the relative uncertainty in the least-squares estimation of $E_d(0^-, \lambda)$ and $L_u(0^-, \lambda)$ is presented in Table 5 as the ratio of the confidence interval to the retrieved value. In general, the relative uncertainty in $L_u(0^-, \lambda)$ is much smaller than it is for $E_d(0^-, \lambda)$ (with the obvious exception of the CHORS `04141407` cast). Excluding this one bad cast, the relative uncertainty is approximately 2% for $L_u(0^-, \lambda)$ and about 7% for $E_d(0^-, \lambda)$. Some casts (BBOP `a061792f` and `a082092c`, and SIO `c0403d`) result in very large values (greater than or equal to 8%) of relative uncertainty for $E_d(0^-, \lambda)$. This is due to the high degree of variability in the near-surface $E_d(z, \lambda)$ profile for these casts (Figs. 2, 3, and 6). The $L_u(0^-, \lambda)$ estimates have significantly lower relative uncertainties for these casts suggesting that the source of error may be due to surface gravity wave-induced irradiance fluctuations (see below).

Comparison of the $K_d(z, \lambda)$ estimates are shown in Figs. 18–26. In general, the comparison looks very good for most of the casts where normalized root mean square (rms) deviations among the four analyses are typically less than 5%. If anything, the normalized rms deviations are smaller for the higher wavelengths ($\lambda > 550$ nm), which

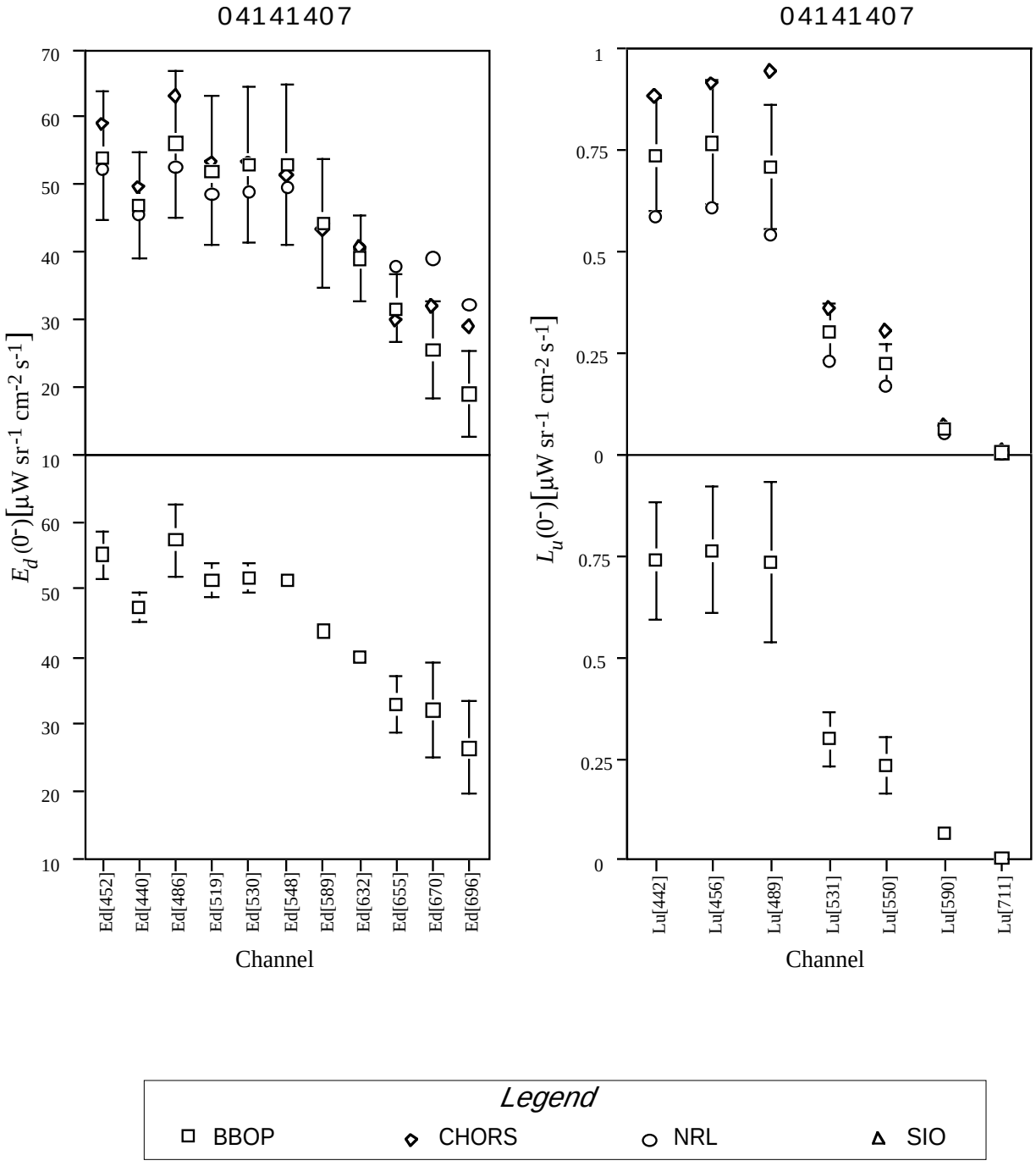

Fig. 11. Estimates of **a)** the downwelling irradiance just beneath the sea surface, $E_d(0^-, \lambda)$, and **b)** the upwelling radiance just beneath the sea surface, $L_u(0^-, \lambda)$ for CHORS `04141407`. In the upper panels, all four of the individual analyses are shown. The error bars in the upper panels correspond to the 95% confidence intervals for the BBOP extrapolations for $E_d(0^-, \lambda)$ and $L_u(0^-, \lambda)$ and are shown in each of the upper panels. The lower panels show the mean of the four analyses and the error bars represent the standard deviation about the mean for each waveband. Only priority 1 casts are shown. Confidence intervals are not calculated as the sample size ($N = 4$) is very small.

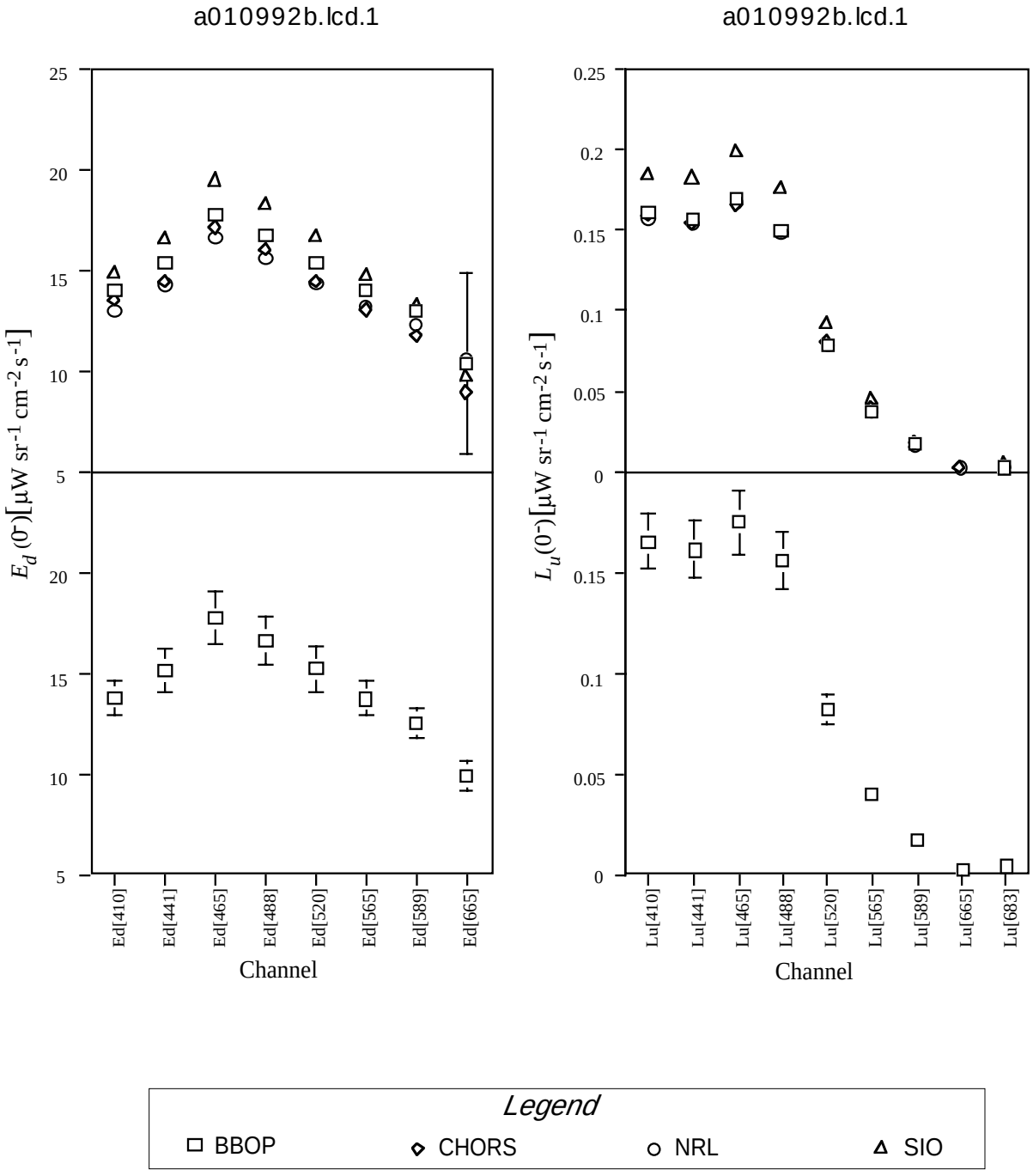

Fig. 12. Estimates of **a)** the downwelling irradiance just beneath the sea surface, $E_d(0^-, \lambda)$, and **b)** the upwelling radiance just beneath the sea surface, $L_u(0^-, \lambda)$ for BBOP `a010992b`. In the upper panels, all four of the individual analyses are shown; the lower panels show the mean of the four analyses. The error bars for the upper and lower panels are the same as those indicated in Fig. 11. Only priority 1 casts are shown. Confidence intervals are not calculated as the sample size ($N = 4$) is very small.

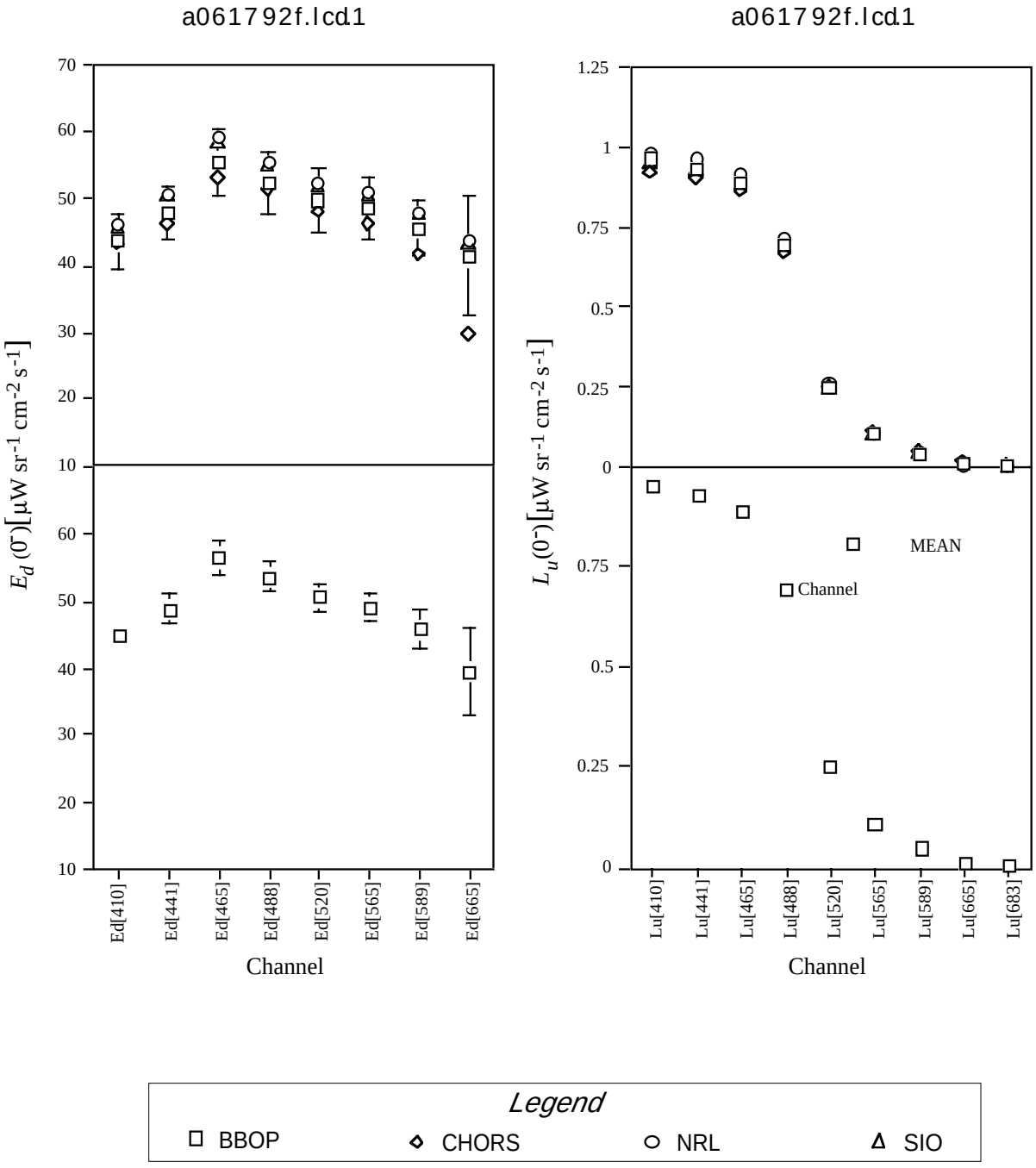

Fig. 13. Estimates of **a)** the downwelling irradiance just beneath the sea surface, $E_d(0^-, \lambda)$, and **b)** the upwelling radiance just beneath the sea surface, $L_u(0^-, \lambda)$ for BBOP `a061792f`. In the upper panels, all four of the individual analyses are shown; the lower panels show the mean of the four analyses. The error bars for the upper and lower panels are the same as those indicated in Fig. 11. Only priority 1 casts are shown. Confidence intervals are not calculated as the sample size ($N = 4$) is very small.

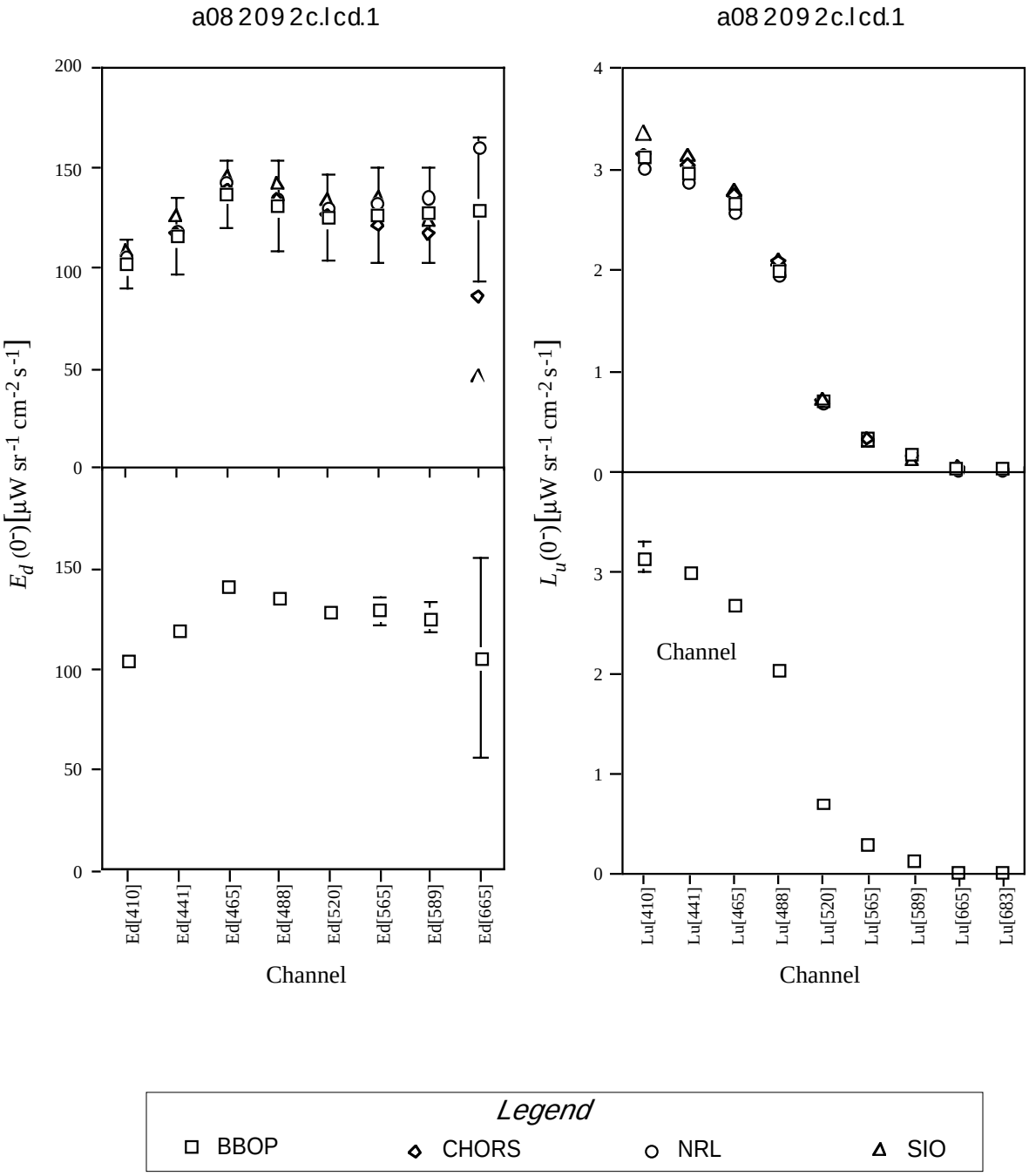

Fig. 14. Estimates of **a)** the downwelling irradiance just beneath the sea surface, $E_d(0^-, \lambda)$, and **b)** the upwelling radiance just beneath the sea surface, $L_u(0^-, \lambda)$ for BBOP `a082092c`. In the upper panels, all four of the individual analyses are shown; the lower panels show the mean of the four analyses. The error bars for the upper and lower panels are the same as those indicated in Fig. 11. Only priority 1 casts are shown. Confidence intervals are not calculated as the sample size ($N = 4$) is very small.

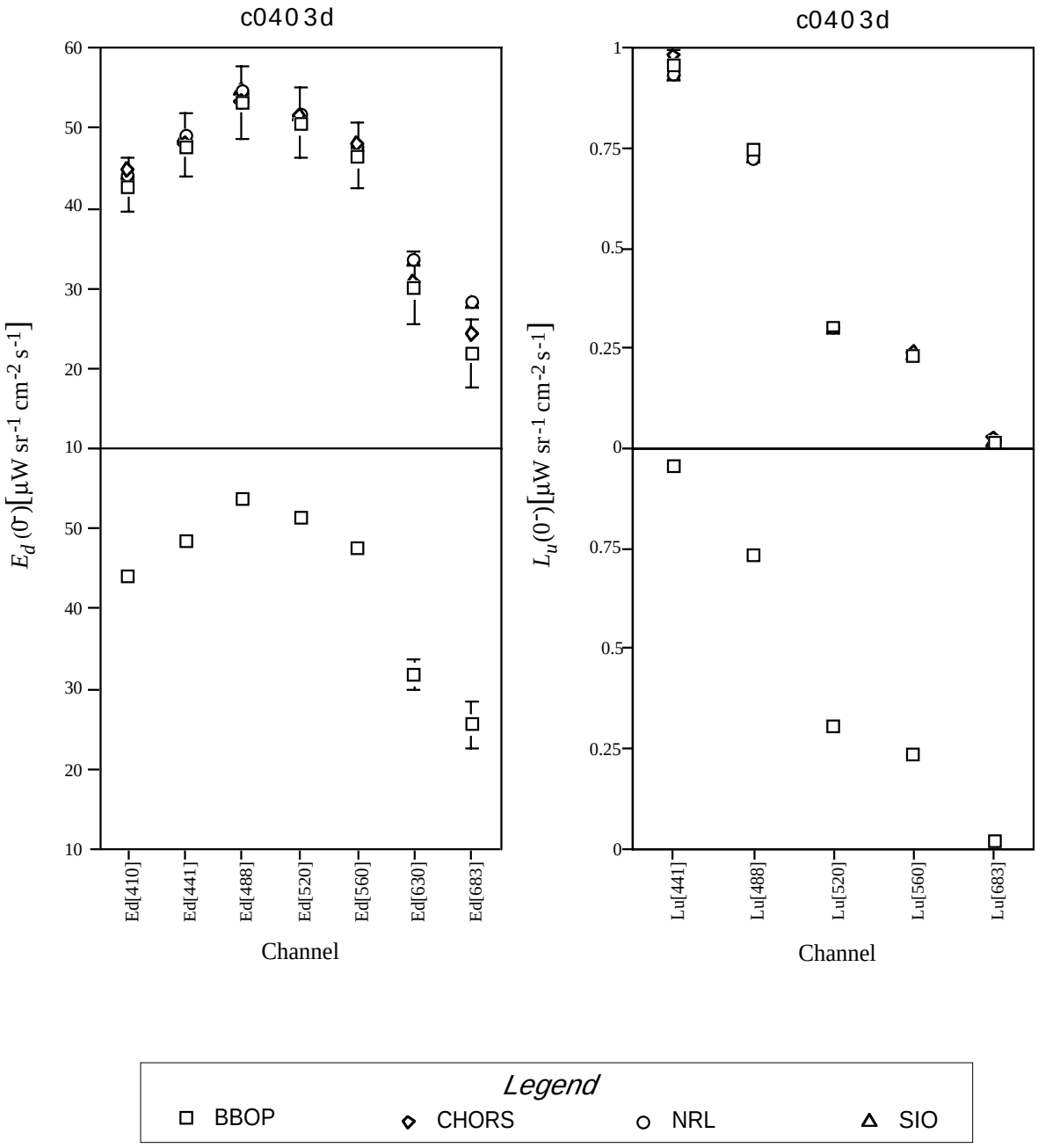

Fig. 15. Estimates of **a)** the downwelling irradiance just beneath the sea surface, $E_d(0^-, \lambda)$, and **b)** the upwelling radiance just beneath the sea surface, $L_u(0^-, \lambda)$ for SIO `c0403d`. In the upper panels, all four of the individual analyses are shown; the lower panels show the mean of the four analyses. The error bars for the upper and lower panels are the same as those indicated in Fig. 11. Only priority 1 casts are shown. Confidence intervals are not calculated as the sample size ($N = 4$) is very small.

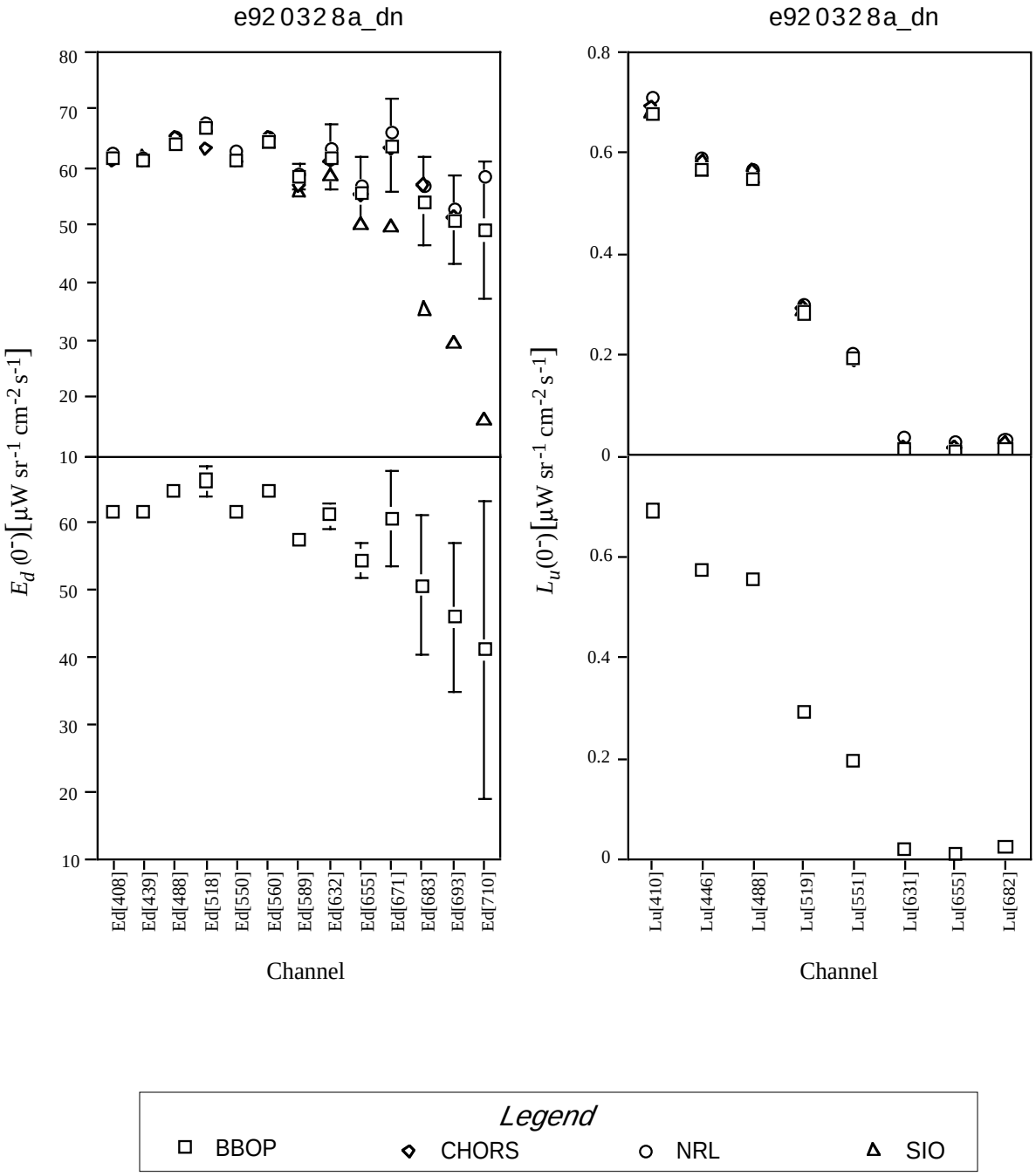

Fig. 16. Estimates of **a)** the downwelling irradiance just beneath the sea surface, $E_d(0^-, \lambda)$, and **b)** the upwelling radiance just beneath the sea surface, $L_u(0^-, \lambda)$ for NRL `e920328a`. In the upper panels, all four of the individual analyses are shown; the lower panels show the mean of the four analyses. The error bars for the upper and lower panels are the same as those indicated in Fig. 11. Only priority 1 casts are shown. Confidence intervals are not calculated as the sample size ($N = 4$) is very small.

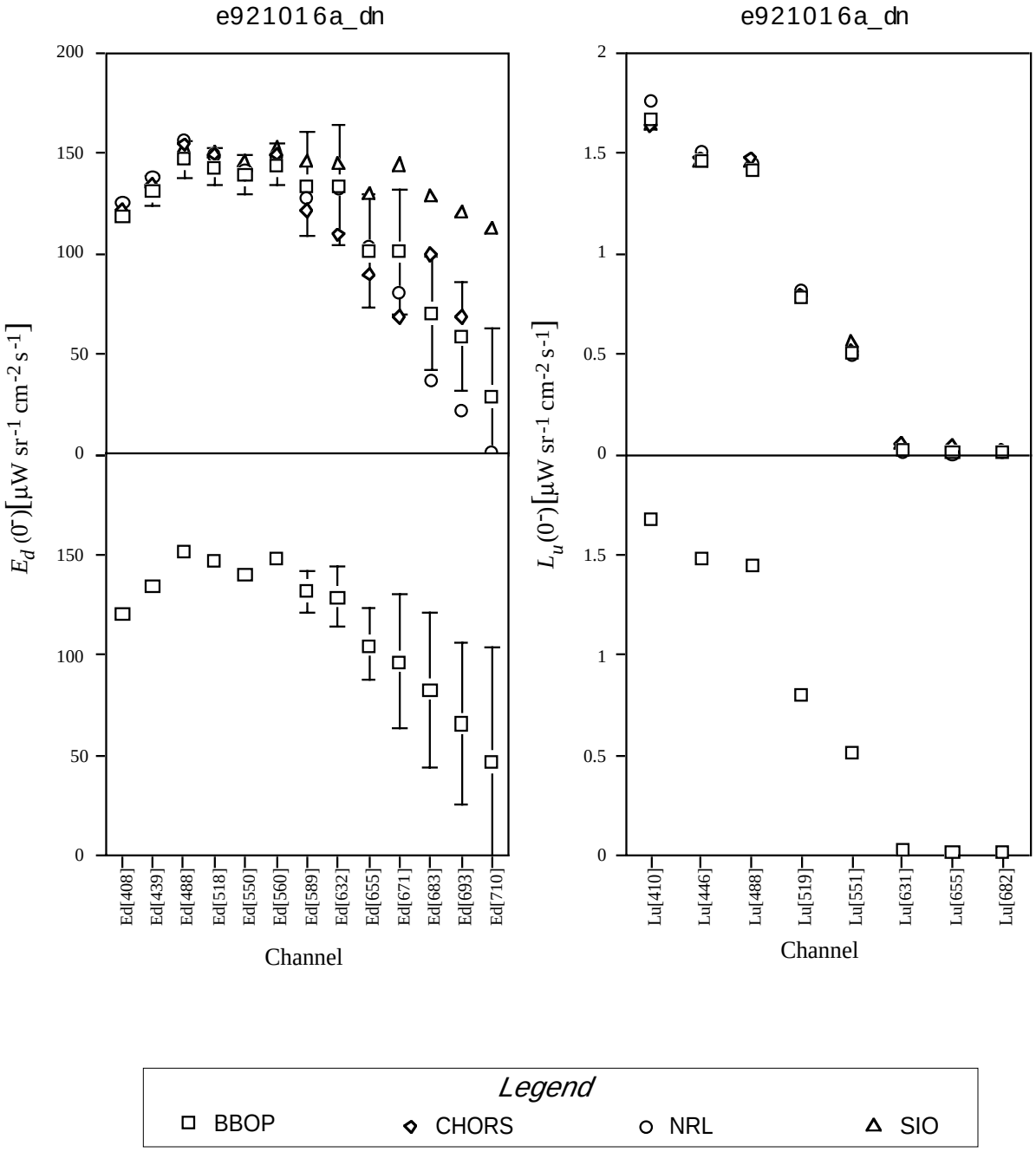

Fig. 17. Estimates of **a)** the downwelling irradiance just beneath the sea surface, $E_d(0^-, \lambda)$, and **b)** the upwelling radiance just beneath the sea surface, $L_u(0^-, \lambda)$ for NRL `e921016a`. In the upper panels, all four of the individual analyses are shown; the lower panels show the mean of the four analyses. The error bars for the upper and lower panels are the same as those indicated in Fig. 11. Only priority 1 casts are shown. Confidence intervals are not calculated as the sample size ($N = 4$) is very small.

Table 4. Coefficients of variation (in percentage) among the four analyses for estimates of $E_d(0^-, \lambda)$ and $L_u(0^-, \lambda)$ from the priority 1 casts. Data are given only where there are overlapping wavebands. Data set mean and standard deviation *EC* values in the last two lines exclude the spurious CHORS cast.

Group	*Cast*	$E_d(0^-, 441)$	$E_d(0^-, 490)$	$E_d(0^-, 520)$	$L_u(0^-, 441)$	$L_u(0^-, 490)$	$L_u(0^-, 520)$
BBOP	a010992b	7.02	6.20	7.17	8.84	8.91	8.24
	a061792f	4.41	4.02	4.12	2.65	2.33	7.97
	a082092c	3.85	3.47	3.32	3.98	3.83	2.57
CHORS	04141407	4.41	9.41	4.69	19.89	27.52	22.30
NRL	e920328a	0.58	0.80	3.30	2.00	1.59	2.00
	e921016a	2.09	2.63	1.99	1.75	1.78	2.05
SIO	c0403d	1.43	1.59	1.18	2.20	1.54	1.49
	Mean	3.40	4.02	3.68	5.90	6.79	6.66
	Standard Deviation	2.19	2.95	1.95	6.64	9.51	7.47
	EC Mean	3.23	3.12	3.51	3.57	3.33	4.05
	EC Standard Deviation	2.35	1.92	2.08	2.70	2.86	3.16

Table 5. Ratio of the BBOP-analyzed 95% confidence estimates for $E_d(0^-, \lambda)$ and $L_u(0^-, \lambda)$ to the estimated value (in percentage) for the priority 1 DARR-94 casts. *EC* values in the last two lines correspond to statistical values excluding the CHORS data.

Group	*Cast*	$E_d(0^-, 441)$	$E_d(0^-, 490)$	$E_d(0^-, 520)$	$L_u(0^-, 441)$	$L_u(0^-, 490)$	$L_u(0^-, 520)$
BBOP	a010992b	2.16	2.11	2.27	2.16	2.03	2.56
	a061792f	8.75	8.97	9.74	1.52	1.11	0.64
	a082092c	16.60	17.40	16.70	1.62	1.84	3.10
CHORS	04141407	16.80	19.70	21.20	18.90	21.60	19.40
NRL	e920328a	5.69	6.11	6.46	1.43	1.57	1.96
	e921016a	0.99	0.99	1.16	0.98	1.43	3.94
SIO	c0403d	8.18	8.28	8.64	3.42	3.42	3.65
	Mean	8.45	9.08	9.45	4.29	4.71	5.04
	Standard Deviation	6.31	7.14	7.31	6.49	7.48	6.43
	EC Mean	7.06	7.31	7.50	1.86	1.90	2.64
	EC Standard Deviation	5.62	5.90	5.65	0.86	0.81	1.22

is due to the fact that the values of $K_d(z, \lambda)$ are much larger for these wavebands. The tracking of the results of the three depth-varying methods (CHORS, BBOP, and NRL) is encouraging. Since the CHORS method is an integral method, its $K_d(z, \lambda)$ profiles are smoother and for many of the DARR-94 profiles it seems to do an excellent job. However, it may not reproduce all the *real* high wavenumber variations in $K_d(z, \lambda)$ as the other methods do.

The largest deviations among the methods occur for those casts that are affected by cloud-induced variations of the incident flux (CHORS 04141407), obvious ship shadows (NRL e921016a and SIO c0403d) or what appear to be surface wave induced variations (BBOP a082092c). Indications of the noise sources are apparent via the pattern of the $K_d(z, \lambda)$ variations with depth. For example, the CHORS 04141407 cast has large random-looking variations in the derived $K_d(z, \lambda)$ values for the BBOP and NRL (differential analyses). The CHORS analyzed $K_d(z, \lambda)$ profile seems to fall in the middle in the scatter between the other two noisy $K_d(z, \lambda)$ profiles. It should be mentioned that this particular cast has an extensive amount of incident irradiance noise and is flagged as unacceptable by the BBOP analysis. The NRL e921016a data shows a single *wiggle* in the $K_d(z, \lambda)$ profile at about 30 m which is likely due to a ship shadow since there are little significant short-time scale variations in the incident flux during this profile (Fig. 5). The BBOP cast with large rms deviations among analyses (BBOP a082092c) seems to show a regular pattern with depth.

The bulk method for $K_d(z, \lambda)$ (SIO) provides only a single point, which is representative of the mixed layer. In general, its retrieved value is consistent with the more sophisticated analyses and there are no apparent biases in the bulk methods $K_d(z_0, \lambda)$ value and the results of the other analyses. It is obvious that the bulk method cannot produce data appropriate for assessing the vertical profile of $K_d(z, \lambda)$.

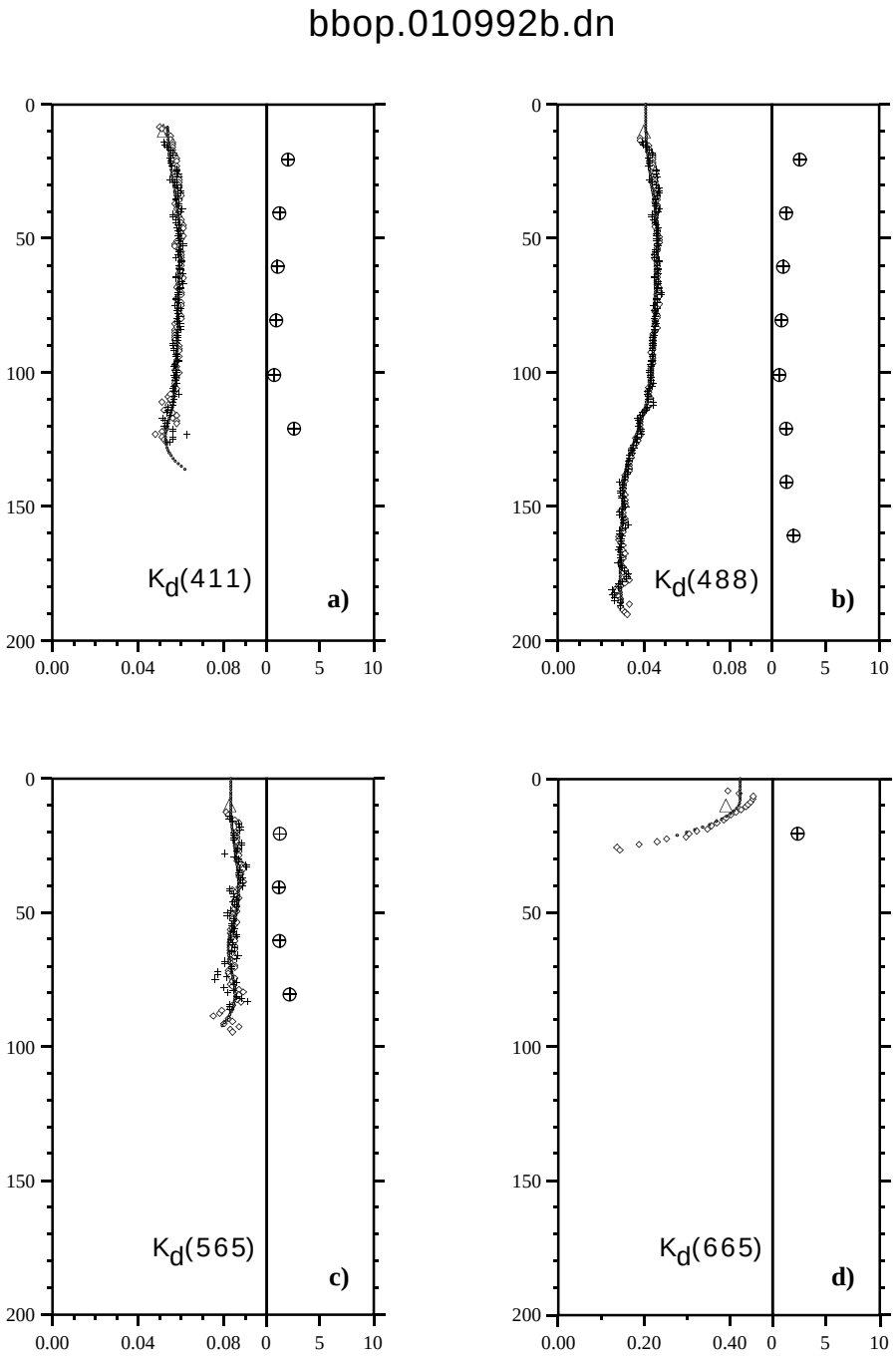

Fig. 18. Vertical profiles of $K_d(z,\lambda)$ for downwelling irradiance from BBOP `010992b`, and the normalized rms deviation for the four DARR-94 analyses in the **a)** blue, **b)** blue-green, **c)** green-yellow, and **d)** red spectral regions. Normalized rms deviations are calculated over 20 m intervals. The four individual analyses are shown as plus signs (+) for BBOP, dots (•) for CHORS, diamonds (◇) for NRL, and triangles (△) for SIO.

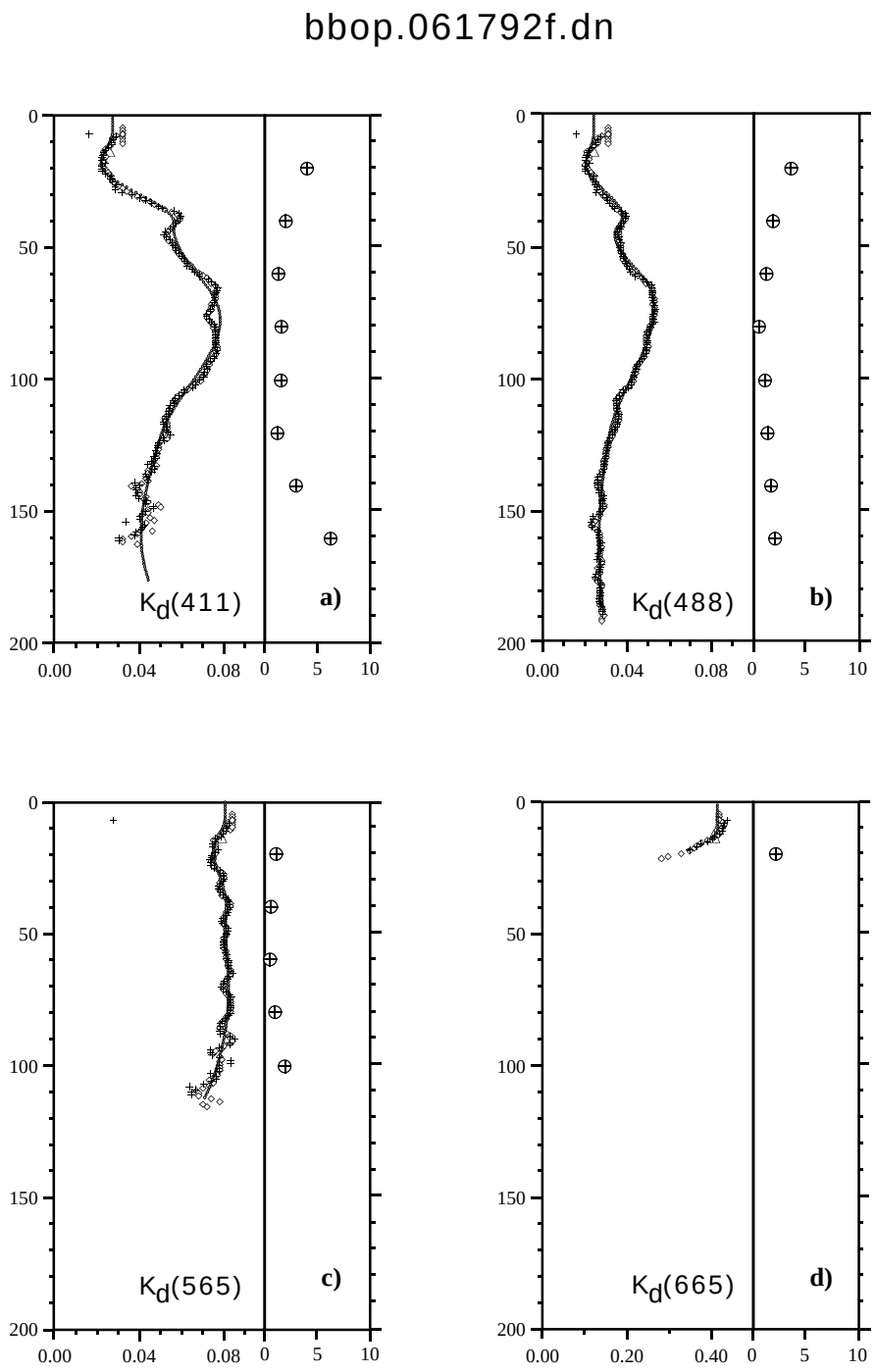

Fig. 19. Vertical profiles of $K_d(z,\lambda)$ for downwelling irradiance from BBOP `061792f`, and the normalized rms deviation for the four DARR-94 analyses in the **a)** blue, **b)** blue-green, **c)** green-yellow, and **d)** red spectral regions. Normalized rms deviations are calculated over 20 m intervals. The four individual analyses are shown as plus signs (+) for BBOP, dots (•) for CHORS, diamonds (◇) for NRL, and triangles (△) for SIO.

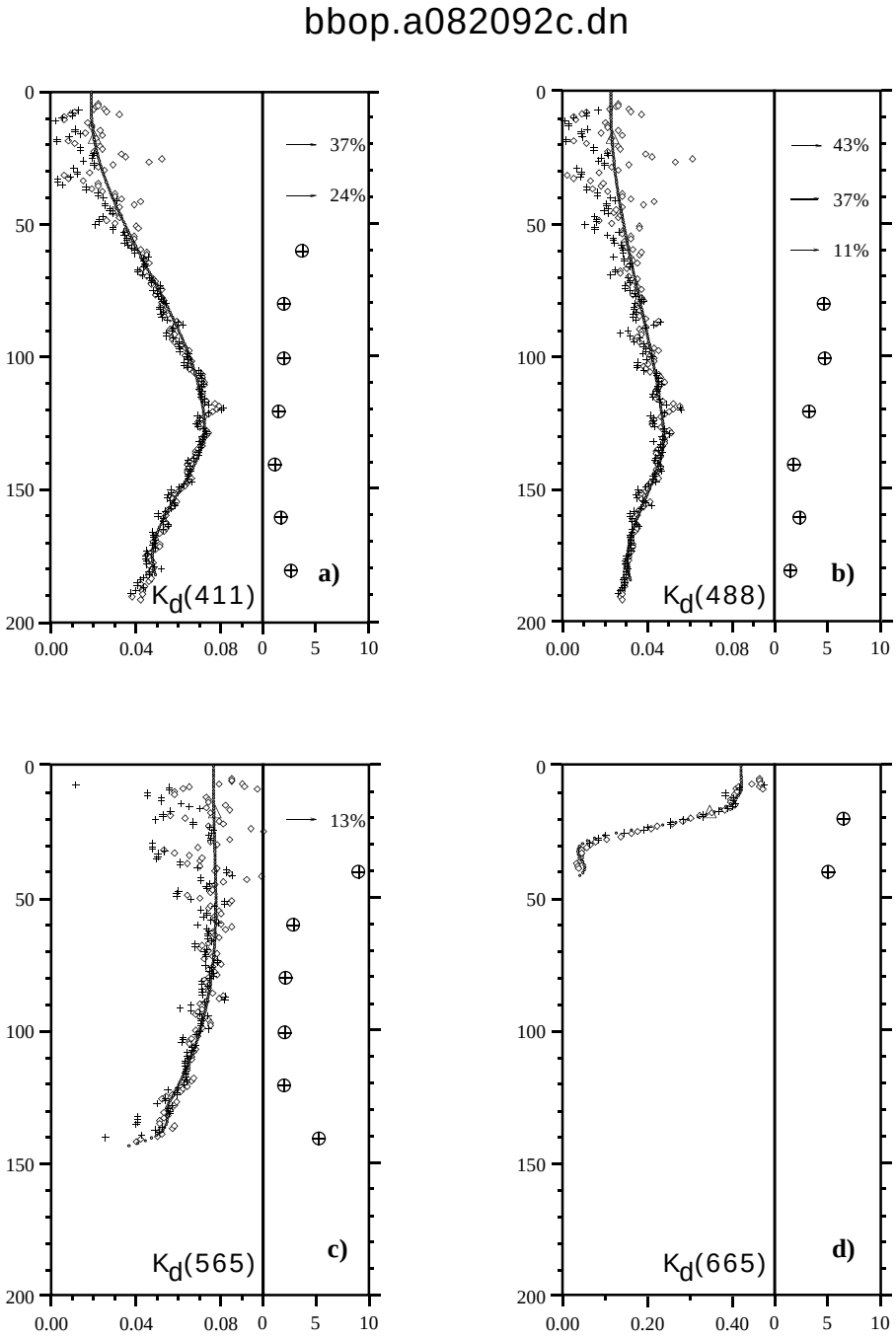

Fig. 20. Vertical profiles of $K_d(z, \lambda)$ for downwelling irradiance from BBOP `a082092c`, and the normalized rms deviation for the four DARR-94 analyses in the **a)** blue, **b)** blue-green, **c)** green-yellow, and **d)** red spectral regions. Normalized rms deviations are calculated over 20 m intervals. The four individual analyses are shown as plus signs (+) for BBOP, dots (•) for CHORS, diamonds (◇) for NRL, and triangles (△) for SIO.

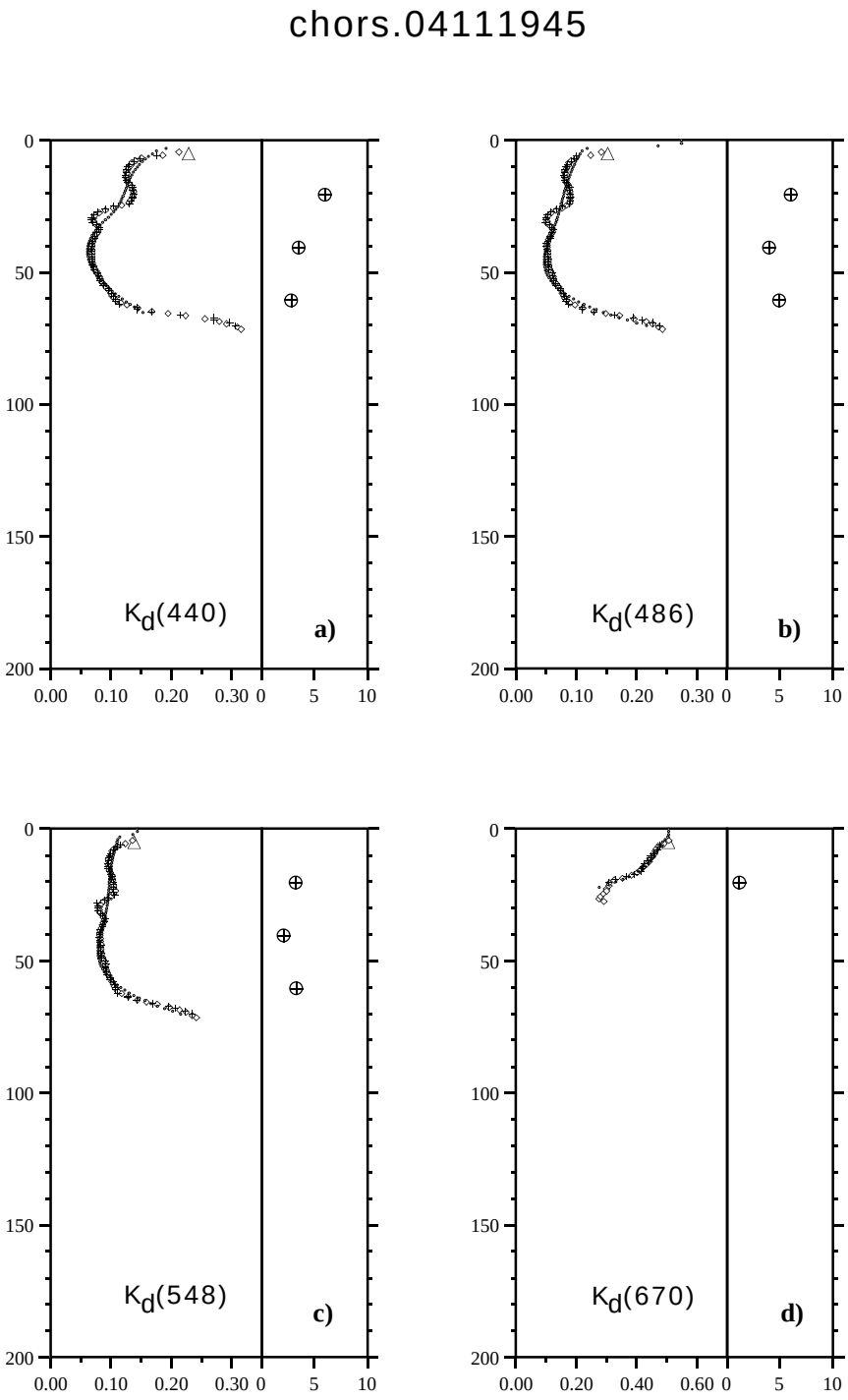

Fig. 21. Vertical profiles of $K_d(z, \lambda)$ for downwelling irradiance from CHORS `04111945`, and the normalized rms deviation for the four DARR-94 analyses in the **a)** blue, **b)** blue-green, **c)** green-yellow, and **d)** red spectral regions. Normalized rms deviations are calculated over 20 m intervals. The four individual analyses are shown as plus signs (+) for BBOP, dots (•) for CHORS, diamonds (◇) for NRL, and triangles (△) for SIO.

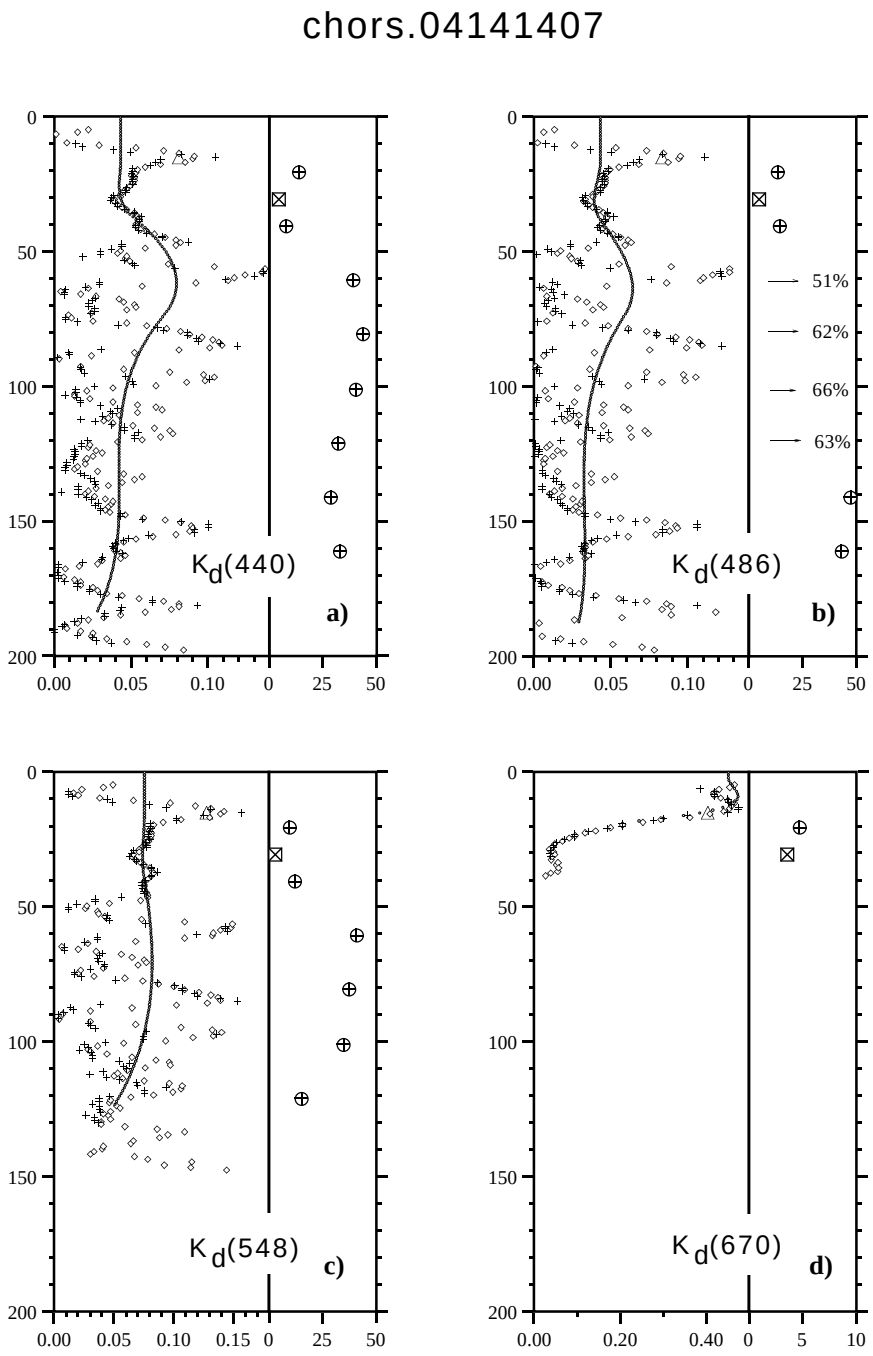

Fig. 22. Vertical profiles of $K_d(z, \lambda)$ for downwelling irradiance from CHORS `04141407`, and the normalized rms deviation for the four DARR-94 analyses in the **a)** blue, **b)** blue-green, **c)** green-yellow, and **d)** red spectral regions. Normalized rms deviations are calculated over 20 m intervals. The four individual analyses are shown as plus signs (+) for BBOP, dots (•) for CHORS, diamonds (◇) for NRL, and triangles (△) for SIO.

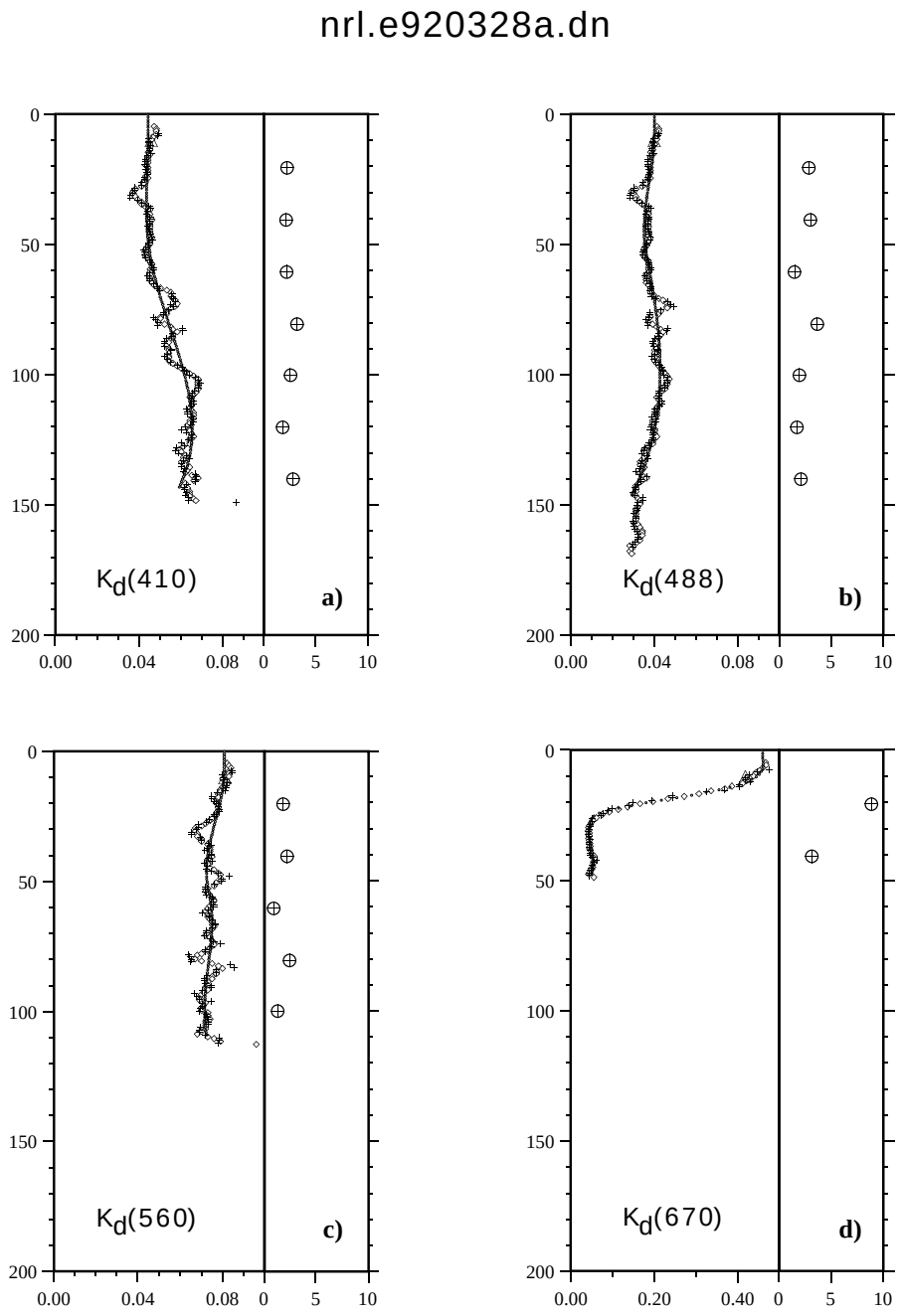

Fig. 23. Vertical profiles of $K_d(z,\lambda)$ for downwelling irradiance from NRL `e920328a`, and the normalized rms deviation for the four DARR-94 analyses in the **a)** blue, **b)** blue-green, **c)** green-yellow, and **d)** red spectral regions. Normalized rms deviations are calculated over 20 m intervals. The four individual analyses are shown as plus signs (+) for BBOP, dots (•) for CHORS, diamonds (◇) for NRL, and triangles (△) for SIO.

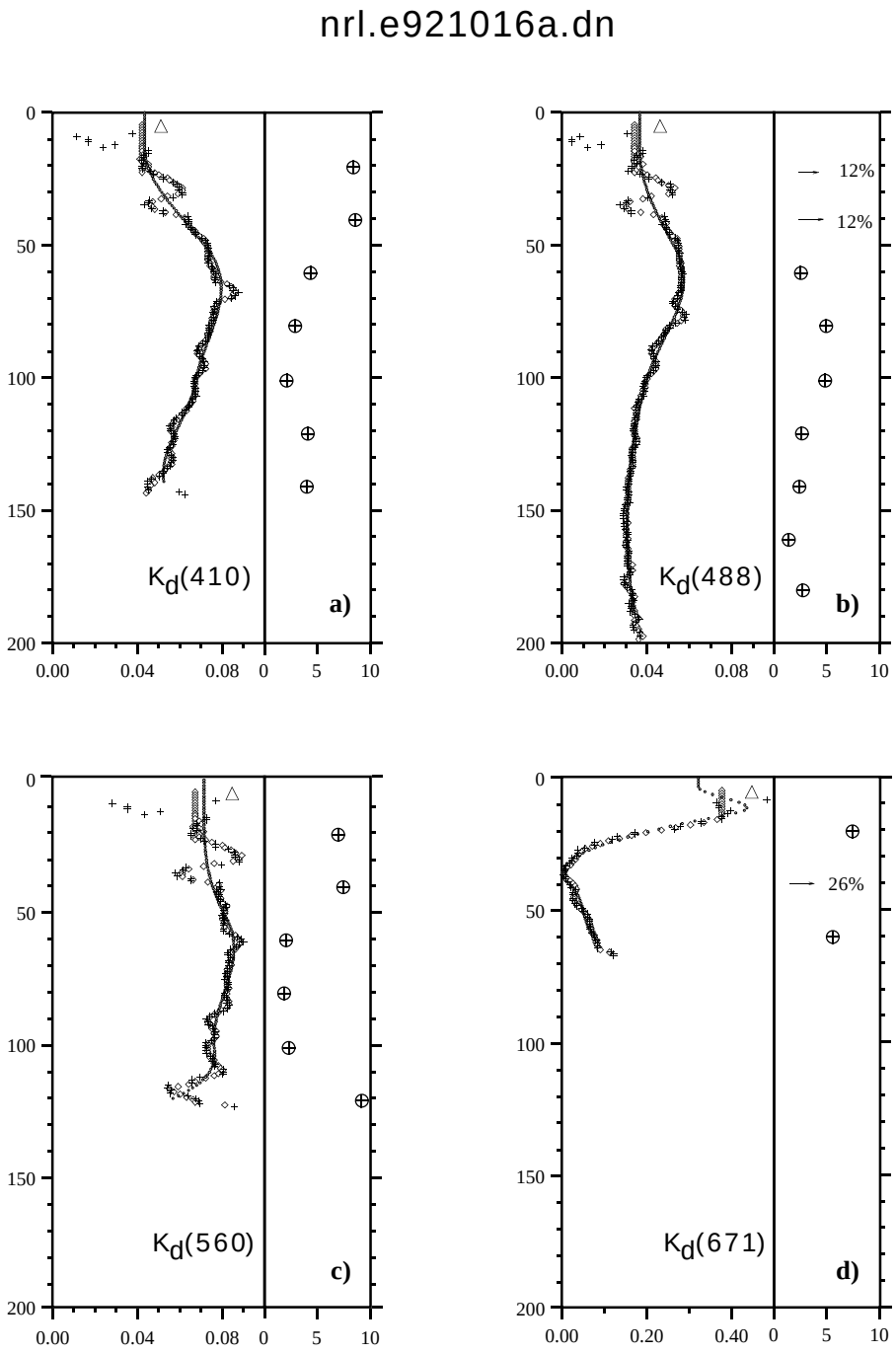

Fig. 24. Vertical profiles of $K_d(z,\lambda)$ for downwelling irradiance from NRL `e921016a`, and the normalized rms deviation for the four DARR-94 analyses in the **a)** blue, **b)** blue-green, **c)** green-yellow, and **d)** red spectral regions. Normalized rms deviations are calculated over 20 m intervals. The four individual analyses are shown as plus signs (+) for BBOP, dots (•) for CHORS, diamonds (◇) for NRL, and triangles (△) for SIO.

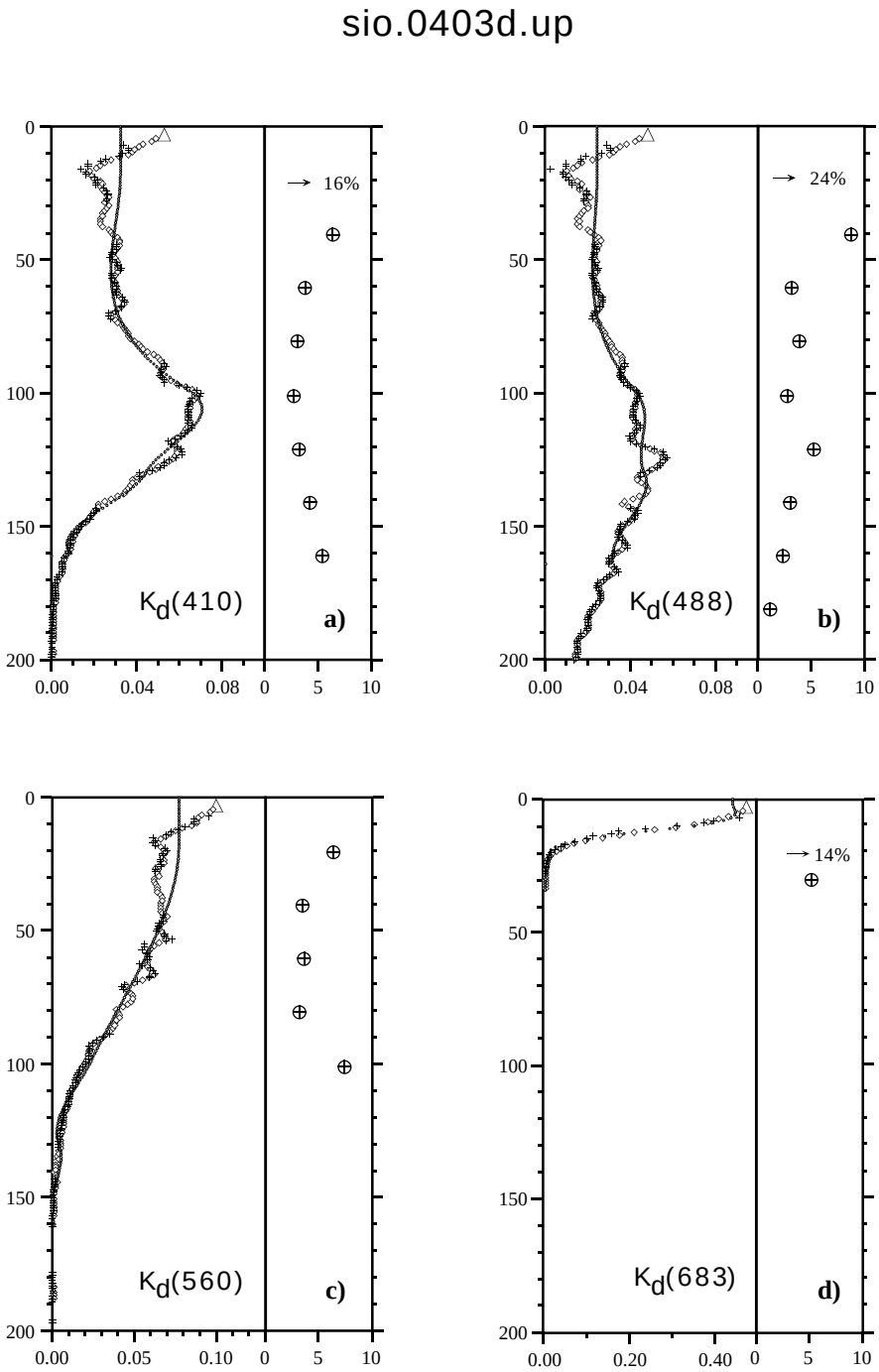

Fig. 25. Vertical profiles of $K_d(z, \lambda)$ for downwelling irradiance from SIO `0403d`, and the normalized rms deviation for the four DARR-94 analyses in the **a)** blue, **b)** blue-green, **c)** green-yellow, and **d)** red spectral regions. Normalized rms deviations are calculated over 20 m intervals. The four individual analyses are shown as plus signs (+) for BBOP, dots (•) for CHORS, diamonds (◇) for NRL, and triangles (△) for SIO.

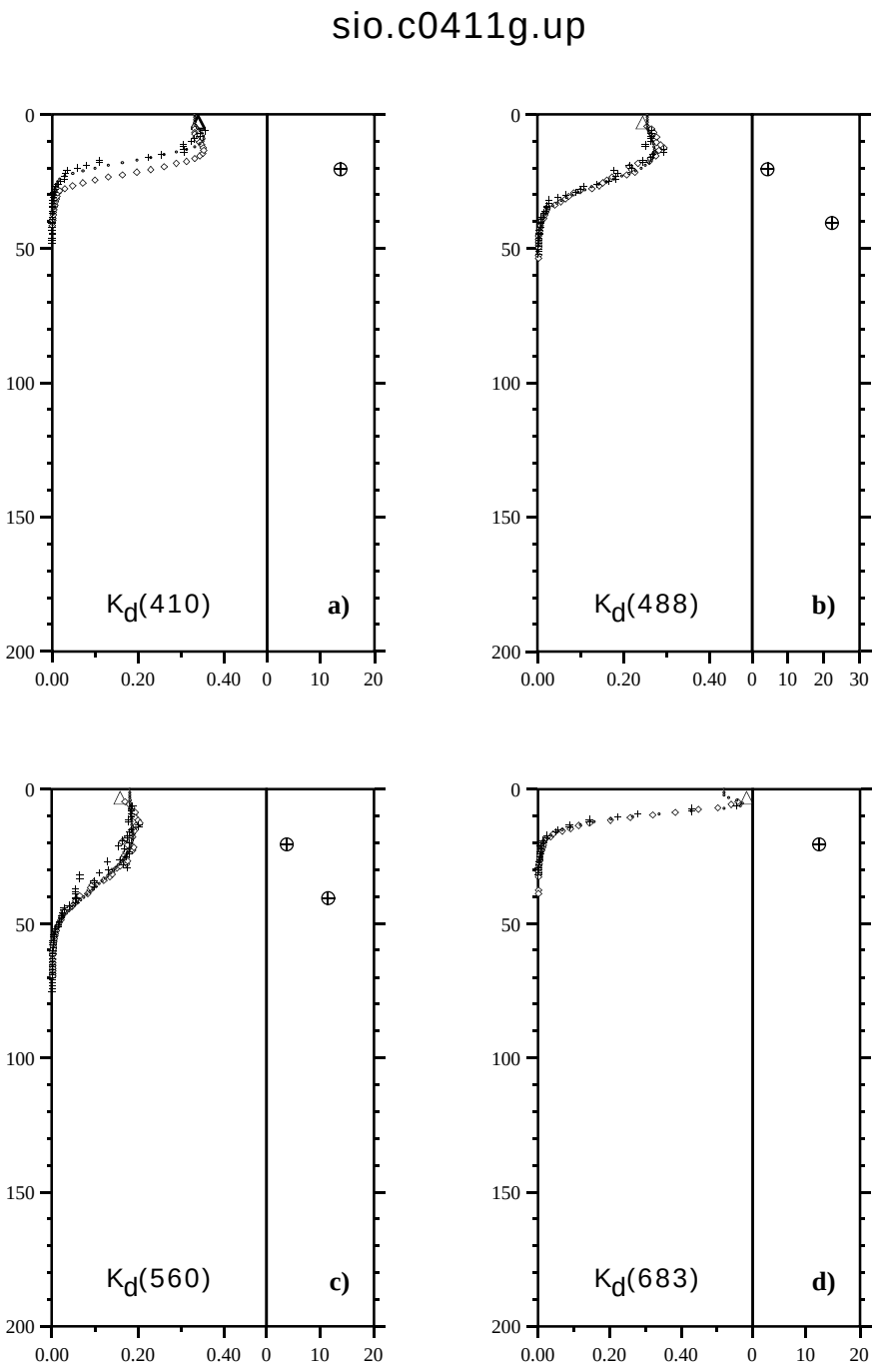

Fig. 26. Vertical profiles of $K_d(z, \lambda)$ for downwelling irradiance from SIO `c0411g`, and the normalized rms deviation for the four DARR-94 analyses in the **a)** blue, **b)** blue-green, **c)** green-yellow, and **d)** red spectral regions. Normalized rms deviations are calculated over 20 m intervals. The four individual analyses are shown as plus signs (+) for BBOP, dots (•) for CHORS, diamonds (◇) for NRL, and triangles (△) for SIO.

1.4 DISCUSSION

The possible cause of deviation among the differing $L_u(0^-, \lambda)$, $E_d(0^-, \lambda)$ and $K_d(z, \lambda)$ estimates can be better understood by considering how a profiling spectroradiometer samples a time-varying sea and how values of $L_u(0^-, \lambda)$ and $E_d(0^-, \lambda)$ are determined. Specifically, a profiling spectroradiometer samples both in time and depth as it is lowered through the water column. If there are sources of *in situ* radiation variability with time scales at, or less than, the time required to sample the upper 20 or so meters of the water column, these variations will be superimposed upon the time-mean signal whose properties are being assessed. The different analysis methods presented here all smooth the data in different manners and evaluate $E_d(0^-, \lambda)$ and $L_u(0^-, \lambda)$ over different portions of the vertical profile and, therefore, will be evaluated over differing sampling times. This results in different values of retrieved AOPs as has been shown.

Cloud-induced variations of the incident flux are an obvious source of noise in an irradiance profile, e.g., CHORS `04141407`. Fortunately, the presence or absence of cloud variations can be evaluated by simultaneously sampling the incident downwelling irradiance. Although time variations at depth may not exactly correspond with incident ones, the presence or absence of incident flux variations provides a measure of whether cloud-induced variations are important (see Figs. 1–10). With the exception of the CHORS `04141407` cast, the priority 1 data set appears to be nearly free from this source of noise variability. The effect of incident flux variations upon the $K_d(z, \lambda)$ estimates is obvious, even when attempts are made to normalize the underwater with the surface fluxes (the CHORS analysis of the CHORS `04141407` cast in Fig. 22).

A major source of $E_d(z, \lambda)$ variability near the sea surface is caused by surface gravity waves (e.g., Dera and Gordon 1968, Snyder and Dera 1970, Siegel and Dickey 1988, and Stramski et al. 1992). The tilting of the sea surface due to surface gravity wave motions results in quasi-random fluctuations in the *in situ* irradiance with time scales on the order of the wave period (cf., Gordon et al. 1971 and Siegel and Dickey 1988). An estimate of the effects of surface gravity waves upon a vertical profile of downwelling irradiance can be made by assuming a dominant swell period of 8 seconds and a package lowering rate of $0.5\,\mathrm{m\,s^{-1}}$. In this example, the surface swell would produce a fluctuating component of irradiance with a vertical scale of approximately 4 m. This signal must be eliminated if accurate estimates of AOPs are to be made by determining the AOPs over some large vertical interval (on the order of 10–20 m). Differences in how this is accomplished will obviously result in differences in the retrieved AOPs. However, this fact points to AOP estimation methods which eliminate (or de-emphasize) the effects of outliers off the time-mean irradiance profiles, e.g., Press et al. 1992.

The observed differences between the uncertainties in the $E_d(0^-, \lambda)$ and $L_u(0^-, \lambda)$ estimates can also be reconciled if one considers the underwater radiance distribution near the sea surface, e.g., Smith 1974 and Voss 1989. Neglecting diffuse light for the moment, the downwelling photons will be restricted to within a Fresnel cone (within 41° of zenith). The area of sea surface sampled by the radiometer increases dramatically with the depth of measurement. Near the sea surface, the extent of the sea surface intersecting the sampling Fresnel cone is small and the effects of surface wave glint will be very important. As the depth of sampling is increased, however, the area of sea surface increases to include many glinting facets. This will effectively average out the effects of the randomly glinting sea surface elements on the sampled irradiance signal. Hence, the effects of sea surface gravity waves will be most prominent on $E_d(z, \lambda)$ profiles near the sea surface which are being used to estimate values of $E_d(0^-, \lambda)$. Profiles of $L_u(z, \lambda)$ will be smoother with respect to depth since upwelling radiance is backscattered downwelling light and, hence, has entered the sea over a considerably larger area than the Fresnel sampling cone for that depth. Therefore, the surface gravity wave noise will affect $E_d(z, \lambda)$ profiles to a much larger degree than $L_u(z, \lambda)$. This can be seen qualitatively in the raw data distributions in Figs. 1–10 or in the relative uncertainty estimates of Table 5. This argument is similar to the ship shadow avoidance distance discussion presented in Mueller and Austin (1995).

Quasi-random variations in the orientation of the spectroradiometer package may also be an important factor in creating noise in $E_d(z, \lambda)$ and $L_u(z, \lambda)$ profiles, particularly near the sea surface. In essence, random tilts can push the collection of $E_d(z, \lambda)$ into, and out of, the Fresnel cone. This affects the $L_u(z, \lambda)$ profile determination to a much lesser degree because of the more uniform angular distribution of the upwelling radiance (Smith 1974 and Voss 1989).

Ship shadows may also be an important factor, which will give rise to variations in the retrieved AOP values. In some sense, a ship shadow provides a time-mean perturbation to *in situ* radiation signals with a depth scale on the order of 10 m. This again will create differences in sea surface extrapolated fluxes if the data are handled in different manners. There may also be a differential spectral response. Unfortunately, this effect cannot be objectively assessed using the present data set.

The results of the DARR-94 workshop do not point to one analysis being better than another, but rather give indications of the inherent uncertainty of AOP estimation due to geophysical noise sources. The different analyses assess different parts of the profile and thus, different parts of the space-time distribution of the *in situ* radiation signal. The different methods average, smooth, and perform curve fits on the raw data profiles in different ways. This strongly suggests *the determination of AOPs from spectroradiometry profiles should be posed as a statistical problem*. Statistically determined AOP estimates should have

associated confidence intervals. The size of the confidence intervals provides an objective measure of the *goodness* of the derived AOP estimate. Presently, only the BBOP data analysis method provides a measure of confidence for the estimate; although this is certainly not a criticism of the other analysis methods.

This vision must be carried through in the analysis and *utilization* of spectroradiometry profiles. Generally, a statistical technique is employed to estimate AOP values, which will naturally provide an uncertainty estimate. This confidence estimate needs to be determined and used. In addition, the means to exploit AOP uncertainties in further analyses and interpretations needs to be developed. For example, a data point with a large uncertainty about its estimated value should have a smaller contribution to a global regression analysis than an estimate with a small uncertainty, e.g., Press et al. 1992.

There are obvious extensions of this thinking to objective mapping of satellite imagery, e.g., Santoreli et al. 1991. This use of confidence intervals may be most important when *in situ* AOP estimates are compared with satellite imagery, i.e., calibration and validation. When performing calibration and validation, a retrieved satellite-sensed pixel value, which has been corrected for the effects of the atmosphere, is compared with the estimated *in situ* AOP value. Both values will have a quantifiable degree of uncertainty associated with them; hence, the calibration and validation problem should be restated formally as a statistical one. This uncertainty information is important and must be considered in future calibration and validation analyses. Researchers must now work to develop effective means to use these important pieces of information.

1.5 CONCLUSIONS

The bottom line result of the DARR-94 study is that, with good data, the spread among different data analysis methods for determining the upwelling radiance and downwelling irradiance just beneath the sea surface, $L_u(0^-, \lambda)$ and $E_d(0^-, \lambda)$, respectively, is about 3–4% of the analyses aggregate mean estimate. The statistical uncertainty in determinations of $E_d(0^-, \lambda)$ are considerably larger (approximately 7%) than those for $L_u(0^-, \lambda)$ (approximately 2%), as found using the BBOP results. These differences can be attributed to geophysical noise sources in the raw data streams, which appear to be dominated by surface wave glinting processes. Furthermore, the profile of the diffuse attenuation coefficient spectrum, $K_d(z, \lambda)$, can be replicated to better than 5% with the differing analyses. These differences account for much of the total 5% uncertainty that is tolerated for SeaWiFS calibration and validation purposes (Mueller and Austin 1995). For bad casts, much larger deviations among methods can occur.

The DARR-94 results do not show a clear winner or loser among the three *sophisticated* data analysis methods. Some degree of outlier rejection is required to accurately estimate $L_u(0^-, \lambda)$ or $E_d(0^-, \lambda)$. Whether this happens automatically (i.e., BBOP) or manually (i.e., CHORS or NRL) does not seem to matter. The bulk method, however, is simply not adequate. Possible solutions include manual or automated data disqualification, robust curve fitting routines, or extrapolation using the incident flux (not fully evaluated here). Furthermore, the calculation, evaluation, and exploitation of confidence intervals for the AOP determinations need to be explored in more detail. This is critical for the long-term assessment of ocean color imagery and its calibration and validation using *in situ* data sets.

Critical to the results presented here is the need for good data. There are no substitutes. Good at-sea procedures are essential including the sampling of unaliased, continuous data sets. The SeaWiFS Project has spent a great deal of effort ensuring that this is the case (Mueller and Austin 1995) and recommends strongly that these guidelines be followed.

Chapter 2

The BBOP Data Processing System

Jens C. Sorensen, Margaret C. O'Brien, Daniel A. Konnoff, and
David A. Siegel
University of California, Santa Barbara, Santa Barbara, California

Abstract

The shear volume of profiling spectroradiometer data is increasing dramatically as global change research programs are placing more emphasis on the evaluation of spatial and temporal structure of ocean biogeochemical cycles. For example, BBOP collects over 1,000 profiles each year in order to link time-series observations of primary production rates to bio-optical parameters. It is likely that these trends will continue as there are several satellite ocean color sensors that are planned to be deployed between now and the end of the century. However, these vast amounts of data must be calibrated, processed, reduced, analyzed, and interpreted in a timely manner. Here, a computer data processing system for efficiently achieving this goal is presented in terms of both computational and human resources. The processing system is comprised of a suite of ANSI `C++` programs that read and operate on a specified file format, the LCD data file. The LCD file contains all relevant data and metadata, which include calibration information and at-sea comments, in a single ASCII file. UNIX shell scripts are used in the control of data flow, as well as error and log handling. The final product is a binned spectroradiometer data set with relevant derived parameters included [$K_d(z,\lambda)$, $R_{rs}(z,\lambda)$, $E_d(0^-,\lambda)$, etc.] that may be disseminated to other groups or databases. At UCSB, the BBOP system has been used for the past two years and the system is available for use by other research groups.

2.1 INTRODUCTION

It is well recognized that ocean optics data sets have a huge potential for addressing many aspects of ocean biogeo-chemical cycles (see for example, Dickey and Siegel 1993). To be effectively used in interdisciplinary studies, such as JGOFS, optical data sets must be made available in a timely manner. For example, in order to effectively collaborate with other investigators in the JGOFS BATS, the BBOP activity must provide and interpret ocean optical data sets on the same time scale as the BATS collaborators to work up pigment, primary production and water chemistry data. In addition, the calibration and validation needs of the upcoming SeaWiFS ocean color mission requires processed ocean optics data in near-real time (McClain et al. 1992).

A major stumbling block in the dissemination and utilization of bio-optical data sets has been the lack of efficient and straightforward data processing schema. Bio-optical data sets have several characteristics which make their *final* products difficult to produce quickly. First, they tend to be large (several Mbytes each) due to high data sampling rates and a diverse parameter range. Second, many profiles (tens to thousands) are often made during a single cruise due to experimental design and the at-sea ease of making these profiles. Recalculation of measured parameters is another characteristic of profiling spectroradiometer data sets that is often necessary, as radiometric calibrations are at times uncertain (Mueller and Austin 1995). Each year, the BBOP sampling collects over 1,000 spectroradiometer profiles, and the instrument is recalibrated at UCSB three times each year. In order to effectively meet scientific, logistic, and collaboration goals, these data must be efficiently processed and analyzed.

In anticipation of this large volume of data, as well as the rapid turn-around requirements imposed by the calibration and validation of satellite data sets, a new data processing system for large volumes of multispectral profile data has been developed. In what follows, the structure and data flow of the BBOP data processing system is introduced. This manuscript is intended as a simplified overview and not as a detailed users' guide (see Siegel et al. 1995b for a users' guide).

Editors' Note: This Chapter has appeared as an article in an *SPIE* publication (Sorensen et al. 1994) and is being included in this volume with permission of the authors and SPIE. Minor editorial changes have been made to reflect the style of the *SeaWiFS Technical Report Series.*

2.2 PHILOSOPHY

As with any data processing system, there are several conceptual and philosophical positions that need to be taken based on the scientific goals of the project and the available resources. In no specific order, the goals of the BBOP data processing system are to:

- Utilize as much of the existing spectroradiometer analysis methods as possible,
- Rapidly produce final archival data sets,
- Minimize human intervention steps,
- Maximize the number of data quality assessment and assurance checks,
- Generate fully self-describing data sets,
- Provide data files in ASCII which are easily read and edited,
- Make quick-look products easy to obtain at several stages of the processing,
- Include processing documentation in the data files at each step,
- Work on many present and future computer platforms, and
- Allow much of the data reduction to be accomplished by an experienced undergraduate student.

As a limitation imposed by the number of casts generated and the imposed rapid turn-around requirements, each profile cannot be manipulated individually. Therefore, in order to assure data quality, many efficient quality assessment and control steps must be implemented. Known sensor problems must be corrected or *flagged*. Examples of known problems include low signal-to-noise ratios (SNRs) in irradiance and radiance channels near the dark current values, and obvious spiking in data fields due to acquisition errors. These problems require that the affected data values be replaced with trap flags (-9.9×10^{35}) so that no processing is performed on these spurious fields. In addition, the quality of the data for some applications is affected by events occurring during collection, including excessive package tilts and variations in incident illumination during a cast due to changes in cloud cover. These events require that entire data records be qualified. In these cases, a new field is created containing a flag which defines the quality of the data based on data values in one or two fields. Data records containing either trap or quality flags can be later deleted or accepted by making simple threshold comparisons.

Provisions also must be made for unknown and unexplained sources of error. These may be simple, the complete failure of a channel, or insidious, the slow change in a calibration constant. To catch these errors, plots must be made of several important quantities on a regular basis. These may be spectra of calculated diffuse attenuation coefficients, reflection ratios, or simply profiles of processed conductivity, temperature, and depth (CTD) data. The BBOP data processing system streamlines the plotting of important parameters by allowing quick output of selected variables as simple ASCII files, which are easily read and manipulated by plotting programs.

The documentation of data processing procedures is often neglected in many data processing schemes. For example, it is essential to trace changes in calibration constants. Things as simple as the digital filtering method used are also important characteristics imposed upon a data set. As part of the BBOP data processing system, processing documentation is added automatically to the data file so that every data user knows explicitly what was done to the data file.

2.3 LCD FILE FORMAT

At the heart of the BBOP processing system is the LCD file and its structure. The LCD file is self-contained, with all pertinent header, calibration, and processing history included. This system is somewhat redundant since much of the header and calibration data will be identical for all casts in a cruise; however, the benefits of easy access to calibration constants and processing history far outweigh the cost of slightly larger data files. During the first 18 months of the BBOP activity, 20 different calibration files have been required due to changes in spectroradiometer calibration, ancillary instruments, and collection software. Record keeping has been simplified by recording all calibration information within each data file. The LCD file can be stored in a compressed format to save disk space.

The LCD file is organized into five major sections separated by keywords in brackets (`<...>`). The header portion, `<cruise_info>`, contains general cast information gleaned from several sources. The `<sampled_parameters>` and `<derived_parameters>` sections contain a list of the contents of the data fields found in the `<data>` section. The `<sampled_parameters>` section also contains the calibration constants. At the end of the LCD file is the `<filters_used>` section which contains a record of all BBOP programs applied to the file as well as any statistical output generated by the programs. Excerpts of an LCD file after some processing are shown in Fig. 27.

The LCD file structure is required by all BBOP filters and scripts. The choice of a conversion program depends on the software used to collect the data. If the data have been collected with Biospherical Instrument's M24-PROF software, the LCD file can be created with the BBOP program, `mer2lcd`. The LCD file is created from the card, binary, and calibration files. The output is an LCD file containing all the necessary features with an abbreviated header, which can be augmented later or concurrently by using the BBOP shell script `smklcd` (Section 2.4.1). Once the LCD file is completed, it is ready for processing using the BBOP filters.

```
<cruise_info>
filename a111292f
date 11-12-1992
position 31 17.96 64 18.81
cruise b50
...
castid index 1mer_time 1depth
a111292f.dt1 2.5000000e+01 1.8150000e+01 1.3406400e+00
a111292f.db1 4.9100000e+02 1.3502500e+02 1.2275800e+02
a111292f.ub1 5.2000000e+02 1.4727500e+02 1.2317100e+02
a111292f.ut1 9.2000000e+02 2.4760000e+02 1.1174000e+00
<sampled_parameters>
1ed410 0.  4.547500e-02 1.603000e-03
...
<derived_parameters>
kc-1ed410
...
<data>
-9.900000e+35 3.457528e+01 3.790249e+01 4.242258e+01 ...
...
<filters_used>
...
bscalc -fr 1ed410 1 20 hmdqa111292f.lcd.1 bhmdqa111292f.lcd.1
#stats ---> samples = 19 abdev = 1.663616e-01
int = 3.457528e+01 slope = 9.904044e-01
min = 9.872207e+00 max = 3.772964e+01
mean = 2.863836e+01 stdDev = 1.364106e+00 var = 1.101210e+00
confidence(95) = 1.381770e+00
bbopkc -fs 1ed410 10 bhmdqa111292f.lcd.1 kbhmdqa111292f.lcd.1
...
```

Fig. 27. Example of an LCD file.

2.4 BBOP FILTERS

The BBOP filters are a suite of UNIX programs designed to perform a variety of functions in the processing of LCD data files:

`mer2lcd` creates the LCD file from the M24-PROF created card, binary, and calibration files.

`bboprecal` recalibrates sampled parameters based on new scales and offsets.

`bbopradq` compares data to thresholds and replaces them with trap flags if they are below the threshold.

`bbopangq` compares package angle data to a constant and writes a quality flag.

`bbopkq` calculates incident irradiance changes over a depth interval and writes a quality flag.

`bbopdespike` flags spikes based on thresholds and forward first difference or slope difference, replacing data with a mean of windowed points.

`bbopmovavg` smooths data using a moving arithmetic mean window (boxcar).

`bboph2o` calculates water properties using UNESCO FORTRAN routines.

`bbopbin` breaks the cast into profiles, sorts the profiles on depth, and averages data over depth intervals creating new LCD files for each profile.

`bscalc` extrapolates data to a null depth (z=0^-) over a specified depth window.

`bbopkc` calculates the diffuse attenuation coefficients.

`bboptrans` performs transformation operations (`log`, `sqrt`, `sin`, etc.) on data.

`bbopmath` performs simple math operations with data by columns, or by one operand and a scalar.

`bbopfutil` extracts or removes fields from an LCD file and writes the result as a new LCD file.

`bbopdeflag` removes or keeps lines of data based on flag values and thresholds.

`bbopstrip` extracts LCD data columns and writes them to a simple ASCII file.

The filters are designed as stand-alone programs that can be applied to LCD files directly or embedded in shell scripts. The BBOP Filters are built using `g++` (gcc) version 2.4.0 and are stable on Sun Microsystems (SUN) Sparc, Digital Equipment Corporation (DEC) Ultrix, and SGI platforms. The BBOP filters will either replace data values within the `<data>` section of the LCD file, add new

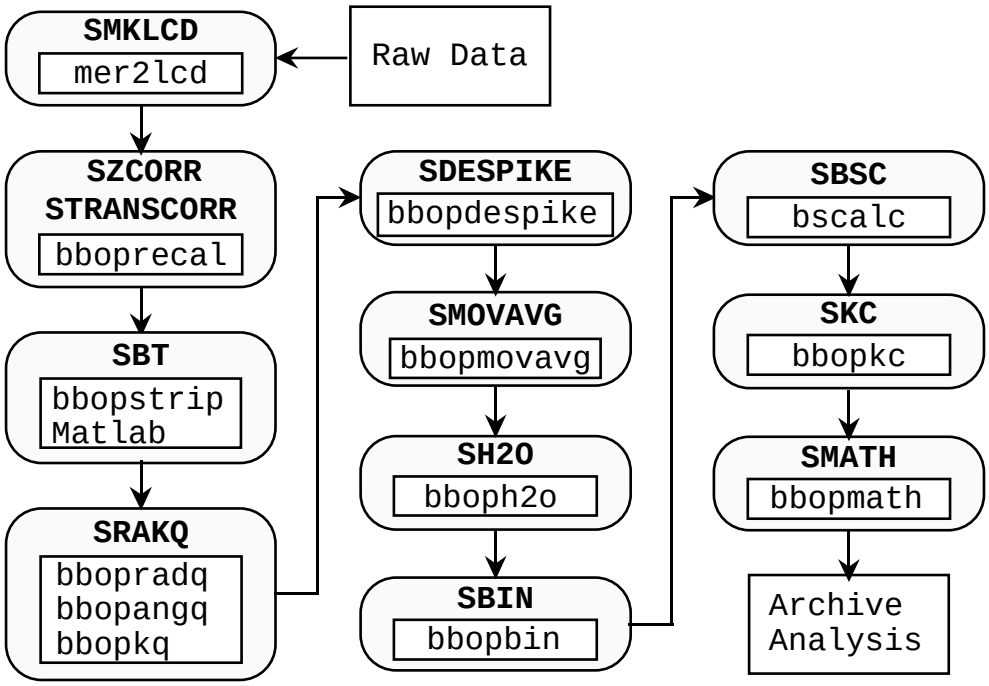

Fig. 28. Schematic cartoon tracing some of the processing steps used in BBOP. The outer shell holds the shell script(s) which in turn call the BBOP filter(s) within the box. The resulting files are binned, qualified LCD files for archiving.

data fields, or do both. New data field names are placed in the `<derived_parameters>` section and can be operated on by most of the filters in the same way as those in the `<sampled_parameters>` section.

All filters share certain fundamental features:

1. Filters read and operate on an external ASCII LCD file and create an output file with a name specified by the user, with the exception of `bbopbin`, which creates the output file name using the input file name.
2. Filters require that LCD files contain all the keywords described above.
3. Filters append the contents of their command lines to the `<filters_used>` section of the output file.
4. Filters will not operate on a field if the same filter and arguments have been used before, or if the new field name already exists.

The flow of data processing is controlled using UNIX shell scripts written in the Bourne and Bash shells. These scripts can create and extract header information, build LCD files, and call graphics packages or BBOP filters. The scripts are used to point to the appropriate directories, automate processing, check for errors in execution, and update log files. Figure 28 illustrates the overall structure of the BBOP processing system. The scripts currently used are as follows:

`smklcd` creates the LCD file from the card, binary and calibration files, and cruise notes.

`szcorr` recalculates the pressure channel using a new cruise offset.

`stranscorr` recalculates the transmissometer channel using the new cruise air calibration and dark offset.

`sbt` determines tops and bottoms of profiles using an interactive Matlab script and inserts the castid table into the LCD header section.

`srakq` qualifies data based on dark value thresholds, instrument tilt, and constant surface illumination intensity.

`sdespike` despikes conductivity, temperature, fluorometer, and transmissometer data twice (two passes).

`smovavg` smoothes despiked conductivity, temperature, fluorometer, and transmissometer channels.

`sh2o` calculates salinity, σ, σ_t, potential temperature, and σ_θ.

`sbin` breaks a cast into profiles, and sorts and averages the data into 1 m bins.

`sbsc` extrapolates below surface irradiance and radiance to a null depth over a predefined window using the robust algorithm.

`skc` calculates attenuation coefficients over a 10 m moving window.

`smath` calculates irradiance and radiance products and ratios.

`sdeflag` removes data lines containing trap flags.

`sloop` is a simple looping program for passing file names to other scripts.

`scmds` automates the entire BBOP processing system (see example below).

The scripts calling individual BBOP filters can be run singly, or more commonly, are combined in a global script (`scmds`). By combining the scripts and utilizing the UNIX environment, the entire data processing system can be automated. Figure 29 shows an example of the global script `scmds`, processing a recalibrated LCD file through completion.

```
#!/local/gnu/bin/bash
lcd_file=‘basename $1‘
logfile=$PWD/log/${lcd_file}.log
{
 echo -n "$lcd_file : "; date
 srakq $1&&\
 sdespike q${lcd_file}&&rm q${lcd_file}&&\
 sfmovavg dq${lcd_file}&&rm dq${lcd_file}&&\
 sh2o mdq${lcd_file}&&rm mdq${lcd_file}&&\
 sbin hmdq${lcd_file}&&\
 { for filename in ‘ls hmdq${lcd_file}.*‘
 do
   sbsc $filename&&\
   skc b${filename}&&rm bhmdq${lcd_file}.*&&\
   smath kb${filename}
 done }
 date
} 2>&1 | tee -a $logfile
```

Fig. 29. An example of the global script `scmds`.

The `&&` construct allows the following command to be executed only if the command preceding it is successful (returns a zero exit value). This insures that if one step fails, the running of the script on a particular file will stop. The standard output of each script is sent to a log file for each LCD. Each script called in `scmds` prefixes a unique letter to the input file name. For example, `hmdqa010193.lcd` indicates that the scripts `srakq`, `sdespike`, `smovavg`, and `sh2o` have been run on the LCD file `a010193.lcd`. In `scmds`, most intermediate LCD files are removed with the exception of the files that precede and follow `bbopbin`, which are later archived. Files are available for quick looks at any step within the processing sequence.

2.5 DATA PROCESSING STEPS

2.5.1 Bottom-to-Top Indexing

Because the LCD file must be eventually split into individual profiles, each cast is examined to determine the tops and bottoms of down- and up-casts. Initially, an automated method for marking these points was pursued, but the great variety in the shape of the time versus depth curve made this determination prohibitively complicated. It was decided that the time versus depth curve must be evaluated manually for each cast. There are any number of ways this could be done. Matlab, a commercial software package, was chosen as a GUI to allow a trained user to interactively select these points. A table comprised of a header line and corresponding indices and depths is inserted into the `<cruise_info>` section of the LCD file (see the example LCD file). These indices and depths are points marking the tops and bottoms of the profiles within the cast. Once these data are inserted, the first line of the table (beginning `castid`) functions as a list of keywords. The data within this table are used by `bbopkq` in anticipation of the binning process and then by `bbopbin`.

2.5.2 Recalculation

Recalculation may be needed due to changes in instrument calibration constants, at-sea atmospheric pressure offsets, or transmissometer offsets. The `bboprecal` filter converts data from engineering units to voltages using scale and offset values from the `<sampled_parameters>` section and converts back to engineering units using the scale and offset values from the command line. The new scale and offset constants are inserted following the variable name in the `<sampled_parameters>` section maintaining a calibration history within the LCD file. Recalibration is not implemented for Sea-Bird (CTD) sampled parameters or derived fields.

2.5.3 Data Qualification

Because the BBOP data processing approach minimizes human intervention, the number of data quality assessment and assurance checks that are made as part of the BBOP data processing is maximized. The first data qualification uses `bbopradq` to assess the ambient light levels for each channel. When ambient light levels fall below a predefined level, the individual data fields are replaced by a trap flag (-9.9×10^{35}). At all later stages of BBOP processing, flagged fields are not operated upon. Lines containing these flags can be later deleted using `bbopdeflag` or in an application program.

The `bbopangq` filter qualifies lines of data based on the orientation of the radiometer in the water, since spectral data may be compromised by excessive tilting of the instrument. This filter creates a new field containing a quality flag rather than replacing data in a field.

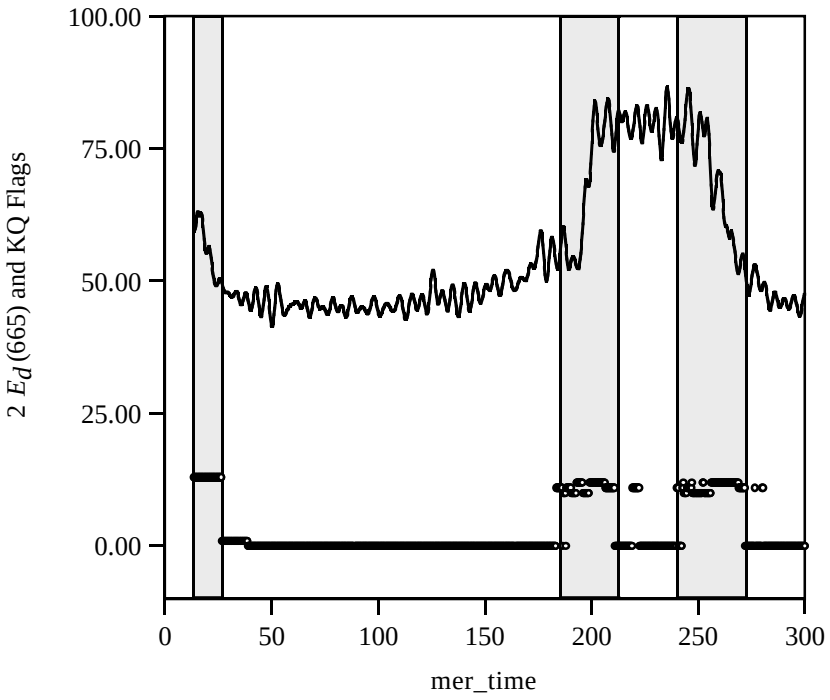

Fig. 30. Incident downwelling irradiance (solid) and K_d quality (KQ) flags produced by `bbopkq`. Regions of non-zero KQ flags (shaded) indicate periods where the calculation of $K_d(z,\lambda)$ may be uncertain due to variable incident irradiance. Lines of data can be later deleted or accepted using `bbopdeflag` and user specified flag thresholds.

Accuracy of the diffuse attenuation coefficient calculation is strongly dependent on a constant intensity of incident radiation during the calculation time interval. The `bbopkq` filter is used to identify the segments of the cast over which surface illumination is steady enough for the diffuse attenuation coefficient to be accurately determined. The `bbopkq` filter uses the `castid` table information to perform its qualification in anticipation of the binning and calculation of attenuation coefficients (see `bbopkc` in Section 2.5.8). The `bbopkq` routine calculates the standard deviation and the mean of the first difference for the group of points centered at each data line within the user-selected depth interval (in meters) over which the attenuation coefficients will be calculated. The user also specifies a threshold values for the standard deviation and maximum first difference with which `bbopkq` compares its calculated values and writes a quality flag into a new field dependent upon the results of the comparison. Later, these flag values can be used to assess the quality of the calculated diffuse attenuation coefficients (Fig. 30).

2.5.4 Despiking and Smoothing

Two types of digital low-pass filters are used to reduce spurious data values (spikes) within the BBOP data processing system. The first filter (`bbopdespike`) uses two criteria, either together or individually, to flag potential data spikes. Flagged values are either replaced with arithmetic means over a user defined window or trap flags if no valid (non-flagged) data exists within that window. The criteria are based upon either a forward first difference or a forward slope difference compared to specified threshold values. The second filter, `bbopmovavg`, uses a moving arithmetic mean (boxcar) with the window size defined by the user. Despiking and smoothing are carried out on temperature, conductivity, transmissometer, and fluorometer fields only. Both the despiking and moving average filters create new fields, leaving the input field untouched.

2.5.5 CTD Calculations

The `bboph2o` routine calculates water characteristics using the standard UNESCO FORTRAN subroutines and writes the calculated parameter as a new field in the LCD file. The `bboph2o` routine must have despiked temperature and conductivity data to produce a smooth salinity profile. Time constant differences between the conductivity and temperature sensors are accounted for using a single-pole digital filter. The following parameters are calculated: salinity, *in situ* density, σ_t, potential temperature, σ_θ, and coefficients of thermal and saline expansion.

2.5.6 Binning

A cast may contain from one to several up or down profiles (yo-yos) and hence, may not be monotone in depth. The binning filter, `bbopbin`, uses the information from the `castid` table to break up the LCD file into individual daughter profiles that are sorted based on pressure and compacted using arithmetic averages over a pressure interval (bin$\pm\Delta$p). The resulting pressure field for each binned profile is also binned to evaluate the *true* depth of each binned data record. Each daughter LCD file retains the complete header and processing history of the original LCD file and contains two new `<derived_parameters>` fields named `bin_m`, where `m` is the interval chosen by the user, and `bin_pts`, containing the number of raw bandwidth data records that have been averaged into that bin. If the file is missing pressure interval data near the surface, `bbopbin` fills in the lines for the missing bins with trap flags such that the binned LCD file begins at its lowest bin interval (i.e., 1.0) and increases monotonically.

2.5.7 Null Depth Extrapolations

The determination of optical fluxes just beneath the sea surface, or at null depth, are of obvious relevance for ocean color remote sensing (Dickey and Siegel 1993 and McClain et al. 1993). The direct determination of null depth optical signals is particularly difficult due to high levels of surface wave glint noise and uncertain water depth determinations. In order to provide accurate data at a null depth for the irradiance and radiance channels, profiling data sets must extrapolate their signals to the sea surface. The BBOP filter `bscalc` employs an algorithm which statistically extrapolates a depth profile to the surface over a user-specified depth interval. The `bscalc` filter allows the user to specify both the upper and lower bounds in the extrapolation interval, and the log-transformed fields are extrapolated to the sea surface using the Beer-Lambert relation (Smith and Baker 1986 and Siegel and Dickey 1987). Two extrapolation algorithms are currently available, the standard chi-square (χ^2) algorithm and a robust algorithm which eliminates points greater than two standard deviations (2σ) from the mean (Press et al. 1992). The `bscalc` filter does not make any derived fields, but rather creates a new line of data at the top of the `<data>` section with `0` in the `bin_m` field and trap flags in any field for which the extrapolation was not calculated. Statistics for the extrapolation fits are included following the command line in the `<filters_used>` section (see the example LCD file).

2.5.8 *K* Calculations

The BBOP filter `bbopkc` calculates the attenuation coefficient, $K_d(z,\lambda)$, at each binned depth interval using the Beer-Lambert relation by employing a sliding regression window. This procedure is similar to that employed by Smith and Baker (1984) and Siegel and Dickey (1987). The user specifies the channel, algorithm, and depth window over which to perform the regressions using either standard χ^2 or robust algorithms (Press et al. 1992). It was decided not to normalize the underwater irradiance fields to simultaneous above-water irradiance data for the $K_d(z,\lambda)$ calculations. The approach is to select profiles that are free from perturbations and to create composites of profiles based on `bbopkq` KQ flags. It is unclear whether the normalization would be relevant in a quickly changing irradiance field due to the passing of small convective cloud elements. Furthermore, it is uncertain whether a surface irradiance normalization routine will mask any variations associated with the incident radiance distribution. The depth window used with `bbopkc` should be the same as was used for `bbopkq`.

2.5.9 Simple Math and Transformations

A variety of utility BBOP filters are also available. For example, `bbopmath` performs simple math operations on LCD data fields (add, subtract, multiply, ratio), and adds a new field to the data section. The `bboptrans` filter performs simple math transformations (`log`, `exp`, `sin`, `asin`, `sqrt`, etc.) on the data and adds a new field to the data section. Both these tools are used in the final stages of processing to produce spectral ratios and reflectance ratios, as well as to calculate the beam attenuation coefficients for the transmissometry field.

2.6 CONCLUSIONS

The BBOP data processing system meets the data processing goals. By making this system available to the community, other investigators will hopefully benefit from the investments made at UCSB and will contribute incremental improvements to the existing system. It is intended that investigators will customize or rewrite the filters and scripts to suit their own needs and systems, as well as contribute suggestions for improvement. This processing system and source code are available to anyone via anonymous ftp from `ftp.icess.ucsb.edu` (`/pub/bbop/soft`). The BBOP data processing system, however, is not intended as a software product, but the usual free software licensing caveats apply.

Acknowledgments

The development of the BBOP data processing system was supported by NSF (OCE 90–16372) and by NASA (NAGW–3145). Support from Digital Equipment Corporation's flagship research project, Sequoia 2000, is also gratefully acknowledged.

Chapter 3

Integral Method for Analyzing Irradiance and Radiance Attenuation Profiles

James L. Mueller
San Diego State University, San Diego, California

Abstract

A method is presented for determining the profile of attenuation coefficient (K) for a vertical profile of irradiance or radiance through a least-squares fit to the optical depth profile, expressed as the integral of K from the surface to each depth z. The measured optical depth at each z is calculated as the natural logarithm of the surface-to-depth ratio of measured irradiances (or radiances). The K profile is represented analytically by Hermitian cubic polynomials connecting nodes at several discrete depths, with unknown values of K and its vertical derivative at each node as coefficients. These polynomials are integrated analytically to each z, which allows each measured optical depth to be set equal to a polynomial with node values of K and its derivative at the node depths. This results in an overdetermined set of equations corresponding to all measured depths in the irradiance (or radiance) profile, which is solved using classical least-squares methods. Prior to solution, irradiance data are normalized to minimize effects of surface irradiance variations, and segments near major anomalies (resulting from strong cloud shadows or ship shadows) are eliminated from the fit. In contrast to the classical derivative solutions for K, the integral approach ensures a correct representation of total attenuation through missing data intervals.

3.1 INTRODUCTION

Vertical profiles of downwelling irradiance $E_d(z,\lambda)$ are related to $E_d(0^-,\lambda)$, incident irradiance just below the sea surface, by the equation

$$E_d(z,\lambda) \;=\; E_d(0^-,\lambda)e^{-\int_0^z K_d(z',\lambda)dz'} \qquad . \qquad (1)$$

The function $K_d(z,\lambda)$ is the profile of irradiance attenuation coefficients throughout the water column. This same equation relates upwelling irradiance $E_u(z,\lambda)$ to $E_u(0^-,\lambda)$ and $K_u(z,\lambda)$ and relates upwelling radiance $L_u(z,\lambda)$ to $L_u(0^-,\lambda)$ and $K_L(z,\lambda)$.

It has become relatively common practice to measure vertical profiles of $E_d(z,\lambda)$, $E_u(z,\lambda)$, and $L_u(z,\lambda)$ using underwater radiometers, with the usual objective being to determine $K_d(z,\lambda)$, $K_u(z,\lambda)$, and $K_L(z,\lambda)$. The classical approach to determining $K(z,\lambda)$ from $E(z,\lambda)$ is described in detail by Smith and Baker (1984 and 1986). It is necessary to first normalize the $E(z,\lambda)$ profile to surface irradiance $E_s(z,\lambda)$ profiles, measured on the deck of the ship during a cast. $K(z,\lambda)$ is then determined by estimating the slope of $\ln\big(E(z,\lambda)\big)$ at depth z; this is accomplished by least-squares fitting a straight line through a data *window* extending several meters above and below depth z. The window is then slid down approximately 1 m and a least-squares K is determined again, and so on over the entire profile.

A typical window size ranges from 8 m (Smith and Baker 1984 and 1986) to 20 m; the latter is used in the present work for preliminary K estimates. This precludes the fitted K profile from following rapid variations through sharply defined layers of suspended particles, which are commonly observed in beam attenuation profiles in coastal and frontal water masses. Even with a 20 m window, moreover, the local slope-fitting procedure is sensitive to high frequency fluctuations in incident irradiance which are not in phase at the on-deck and underwater radiometers.

A new method is presented for determining K profiles by minimizing the departure of the estimated optical depth profile

$$\hat{\tau}(z,\lambda) \;=\; \int_0^z K(z',\lambda)dz' \qquad (2)$$

from the measured optical depth profile

$$\tau(z,\lambda) \;=\; \ln\left[\frac{E(0^-,\lambda)}{E(z,\lambda)}\right]. \qquad (3)$$

The new approach has the advantage of being able to more closely follow variations in K through very turbid

layers, as indicated independently by beam attenuation. At the same time, the integral approach is more successful at smoothing through surface irradiance fluctuations than is the local slope-fitting method.

3.2 DECK CELL SMOOTHING

The first step in this procedure is to fit the deck cell irradiance profiles $E_s(z,\lambda)$ directly to Hermitian cubic basis functions,

$$\begin{aligned}\gamma_{01}(\xi) &= \frac{1}{4}(\xi-1)^2(\xi+2),\\ \gamma_{02}(\xi) &= \frac{-1}{4}(\xi+1)^2(\xi-2),\\ \gamma_{11}(\xi) &= \frac{L_i}{8}(\xi-1)^2(\xi+1), \quad \text{and}\\ \gamma_{12}(\xi) &= \frac{L_i}{8}(\xi+1)^2(\xi-1).\end{aligned} \tag{4}$$

For z in the ith depth element $z_{i-1} \le z < z_i$, ξ is a local coordinate ranging from -1 at node z_{i-1} (the shallow end point of the element) to $+1$ at node z_i, that is,

$$\xi = \frac{1}{L_i}\Big(2z - \big(z_i + z_{i-1}\big)\Big), \tag{5}$$

with differential

$$d\xi = \frac{2}{L_i}dz, \tag{6}$$

where L_i is the length of ith finite element, i.e.,

$$L_i = z_i - z_{i-1}. \tag{7}$$

At any depth z corresponding to location ξ in element i, the smoothed estimate of deck cell irradiance $\hat{E}_s(z,\lambda)$ will be given by

$$\begin{aligned}\hat{E}_s(z,\lambda) &= \gamma_{01}(\xi)\overline{E}_{s,i-1}(\lambda)\\ &+ \gamma_{02}(\xi)\overline{E}_{s,i}(\lambda)\\ &+ \gamma_{11}(\xi)\frac{\partial}{\partial z}\overline{E}_{s,i-1}(\lambda)\\ &+ \gamma_{12}(\xi)\frac{\partial}{\partial z}\overline{E}_{s,i}(\lambda),\end{aligned} \tag{8}$$

where $\overline{E}_{s,i}(\lambda)$ is the value of $E_s(z,\lambda)$, and $\frac{\partial}{\partial z}\overline{E}_{s,i}(\lambda)$ is its derivative with respect to z, at node depth z_i. Both the function $\hat{E}_s(z,\lambda)$ and its first derivative are continuous at nodes joining adjacent finite depth elements.

The profile of measured $E_s(z,\lambda)$ is displayed on the computer's screen. Nodes are placed at N depths z_n ($n = 0,\ldots,N-1$) selected to allow the cubic functions of (8) to closely follow major excursions of incident irradiance, while smoothing high frequency *wiggles* which are unlikely to be well matched to incident irradiance fluctuations observed by the underwater radiometer. The selection of which E_s fluctuations follow closely is one subjective element in this procedure. The recommended practice is to pick nodes which allow the fitted curve to closely follow fluctuations with wavelengths greater than or equal to 10 m, and to smooth out shorter scale fluctuations. In the time domain, 10 m corresponds to approximately 20 s at a typical winch speed of 0.5 m s^{-1}.) The smoothed $E_s(z,\lambda)$ and normalized $E_d(z,\lambda)$ profiles should, in any event, be examined jointly before proceeding further. If features in the fitted E_s curve are reflected by opposing features in the E_d curve indicating overcompensation by the deck cell normalization, then the data from that segment of both profiles should be eliminated from the fitting procedure.

Once node depths z_n are selected, the $E_s(z_m,\lambda)$ vector, measured at $m = 1,\ldots,M$ depths z_m, may be expressed in matrix form as

$$\vec{E}_s(z_m,\lambda) = \mathbb{H}\vec{\overline{E}}_s(\lambda), \tag{9}$$

where $\vec{E}_s(\lambda)$ is the measured irradiance vector of length M

$$\vec{E}_s(\lambda) = \begin{pmatrix} E_s(z_1,\lambda)\\ E_s(z_2,\lambda)\\ \vdots\\ E_s(z_m,\lambda)\\ \vdots\\ E_s(z_M,\lambda)\end{pmatrix}, \tag{10}$$

$\vec{\overline{E}}_s(\lambda)$ is the unknown vector (of length $2N$) of irradiances and vertical gradients of irradiance at the N node depths z_n,

$$\vec{\overline{E}}_s(\lambda) = \left(\begin{array}{c} \overline{E}_{s,0}(\lambda)\\ \overline{E}_{s,1}(\lambda)\\ \vdots\\ \overline{E}_{s,n}(\lambda)\\ \vdots\\ \overline{E}_{s,N-1}(\lambda)\\ \hline \frac{\partial}{\partial z}\overline{E}_{s,0}(\lambda)\\ \frac{\partial}{\partial z}\overline{E}_{s,1}(\lambda)\\ \vdots\\ \frac{\partial}{\partial z}\overline{E}_{s,n}(\lambda)\\ \vdots\\ \frac{\partial}{\partial z}\overline{E}_{s,N-1}(\lambda)\end{array}\right), \tag{11}$$

and $\mathbb{H}$ is a matrix with $2N$ columns and M rows

$$\mathbb{H} = \big[h_{mj}\big], \tag{12}$$

with elements

$$h_{mj} = \begin{cases} \gamma_{01}, & z_m \text{ in element } n \text{ and } j = n-1;\\ \gamma_{11}, & z_m \text{ in element } n \text{ and } j = n-1+N;\\ \gamma_{02}, & z_m \text{ in element } n \text{ and } j = n;\\ \gamma_{12}, & z_m \text{ in element } n \text{ and } j = n+N;\\ 0, & \text{otherwise.}\end{cases} \tag{13}$$

To reduce (9) to normal form for least-squares determination of the vector $\vec{E}_s$, multiply both sides by $\mathbb{H}^T$, the transpose of $\mathbb{H}$, and rearrange to obtain

$$\vec{\overline{E}}_s(\lambda) \;=\; \left[\mathbb{H}^T\mathbb{H}\right]^{-1}\mathbb{H}^T\vec{E}_s(\lambda), \tag{14}$$

where $\left[\mathbb{H}^T\mathbb{H}\right]^{-1}$ is the inverse matrix of $\left[\mathbb{H}^T\mathbb{H}\right]$.

The resulting components $\overline{E}_{s,n}(\lambda)$ are the coefficients needed, together with the array of node depths z_n, to compute smoothed deck cell irradiance $\vec{E}_s(\lambda)$ at any depth z using either (8) or its matrix equivalent (9).

The smoothed E_s profiles are now ready for use in obtaining smoothed fits to measured profiles of downwelling irradiance $E_d(z,\lambda)$, upwelled irradiance $E_u(z,\lambda)$, and upwelled radiance $L_u(z,\lambda)$. To provide guidance for node placement in a least-squares fit to cubic Hermitian finite elements, the profiles are first binned to 1 m intervals, and preliminary attenuation coefficients K are estimated using the classic practice of fitting a least-squares slope over a window extending a few meters (in this case ±10 m) on each side of each depth point, e.g., Smith and Baker (1984 and 1986).

3.3 BIN-AVERAGED PROFILES

Profiles of $E_d(z,\lambda)$, $E_u(z,\lambda)$, and $L_u(z,\lambda)$ are averaged into 1 m depth bins in preparation for preliminary least-squares smoothing to obtain the vertical attenuation coefficients of each quantity. The preliminary smoothing algorithm outlined below is similar to that described by Smith and Baker (1984):

$$\begin{aligned} K'_d(z,\lambda) \;&=\; \frac{-1}{E_d(z,\lambda)}\frac{d}{dz}E_d(z,\lambda), \\ K'_u(z,\lambda) \;&=\; \frac{-1}{E_u(z,\lambda)}\frac{d}{dz}E_u(z,\lambda), \quad \text{and} \\ K'_L(z,\lambda) \;&=\; \frac{-1}{L_u(z,\lambda)}\frac{d}{dz}L_u(z,\lambda) \end{aligned} \tag{15}$$

are determined by least-squares fits to the equations

$$\begin{aligned} \ln\left[\frac{E_d(z,\lambda)\overline{E}_s(550)}{E_s(z,550)}\right] \;&=\; A_d(\overline{z},\lambda) - K'_d(z,\lambda)[z-\overline{z}], \\ \ln\left[\frac{E_u(z,\lambda)\overline{E}_s(550)}{E_s(z,550)}\right] \;&=\; A_u(\overline{z},\lambda) - K'_u(z,\lambda)[z-\overline{z}], \\ \ln\left[\frac{L_u(z,\lambda)\overline{E}_s(550)}{E_s(z,550)}\right] \;&=\; A_l(\overline{z},\lambda) - K'_L(z,\lambda)[z-\overline{z}], \end{aligned} \tag{16}$$

where $\overline{z}$ is the mid-depth of a 20 m window, $\overline{E}_s(550)$ is the smoothed 550 nm deck cell irradiance at depth $\overline{z}$, $E_s(z,550)$ is the 550 nm deck cell irradiance coincident with measurements at depth z, and the intercepts A correspond to the natural logarithm of smoothed irradiance or radiance at depth $\overline{z}$, i.e.,

$$\begin{aligned} A_d(\overline{z},\lambda) \;&=\; \ln\left[E'_d(\overline{z},\lambda)\right], \\ A_u(\overline{z},\lambda) \;&=\; \ln\left[E'_u(\overline{z},\lambda)\right], \quad \text{and} \\ A_l(\overline{z},\lambda) \;&=\; \ln\left[L'_u(\overline{z},\lambda)\right]. \end{aligned} \tag{17}$$

The values of $E'_d(\overline{z},\lambda)$, $E'_u(\overline{z},\lambda)$, and $L'_u(\overline{z},\lambda)$ [as obtained from $A_d(\overline{z},\lambda)$, $A_u(\overline{z},\lambda)$, and $A_l(\overline{z},\lambda)$ by the above least-squares smoothing algorithm] are then each normalized to the surface by the ratio of deck cell irradiance $E_s(0,550)$:$E_s(\overline{z},550)$ calculated using (14).

The resulting smoothed profiles of K' and E' are used as a guide in selecting node depths for fitting improved K and E profiles to the measured irradiance.

3.4 OPTICAL DEPTH PROFILE FIT

Measured optical depth $\tau(z)$ at depth z is calculated as

$$\tau(z) \;=\; \ln\left[\frac{E(0^-)}{E(z)}\right], \tag{18}$$

where E may be E_d, E_u or L_u, and $E(0^-)$ is irradiance (or radiance) just beneath the sea surface. A first guess estimate of $E(0^-)$ is obtained from the preliminary bin-averaged, window-fit K' and E' profiles as

$$E(0^-) \;\cong\; E'(10)e^{10K'(10)}. \tag{19}$$

[Because of the 20 m fitting window, $K'(10)$ and $E'(10)$ at 10 m are the shallowest estimates in that profile.]

Optical depth is related to the irradiance (or radiance) attenuation coefficient $K(z)$ profile by the

$$\tau(z) \;=\; \int_0^z K(z')dz'. \tag{20}$$

If once again the water column is divided into $N-1$ finite elements, separated by N nodes at depths z_n ($n = 0,\ldots,N-1$), $K(z)$ may be estimated in the depth element $z_{n-1} \le z < z_n$ as

$$\begin{aligned} \hat{K}(z) \;=\; &\gamma_{01}(\xi)\overline{K}_{n-1} \;+\; \gamma_{02}(\xi)\overline{K}_n \\ &+\; \gamma_{11}(\xi)\frac{\partial}{\partial z}\overline{K}_{n-1} \;+\; \gamma_{12}(\xi)\frac{\partial}{\partial z}\overline{K}_n, \end{aligned} \tag{21}$$

where $\gamma_{ij}(\xi)$ and ξ are defined in (4) and (5), respectively. The same form of cubic Hermitian polynomial expansion is used in (8) and (21) to represent the variables $E_s(z)$ and $K(z)$, respectively.

If (21) is substituted into (20), the resulting equation obtains for $z_{n-1} \le z < z_n$:

$$\begin{aligned}\tau(z) \;=\; \sum_{i=1}^{i<n}\Bigg[& \overline{K}_{i-1}\int_{z_{i-1}}^{z_i}\gamma_{01}(\xi)dz' + \overline{K}_{i-1}\int_{z_{i-1}}^{z_i}\gamma_{02}(\xi)dz' \\ & + \frac{\partial}{\partial z}\overline{K}_{i-1}\int_{z_{i-1}}^{z_i}\gamma_{11}(\xi)dz' + \frac{\partial}{\partial z}\overline{K}_{i}\int_{z_{i-1}}^{z_i}\gamma_{12}(\xi)dz'\Bigg] \\ & + \overline{K}_{n-1}\int_{z_{n-1}}^{z}\gamma_{01}(\xi)dz' + \overline{K}_{n}\int_{z_{n-1}}^{z}\gamma_{02}(\xi)dz' \\ & + \frac{\partial}{\partial z}\overline{K}_{n-1}\int_{z_{n-1}}^{z}\gamma_{11}(\xi)dz' + \frac{\partial}{\partial z}\overline{K}_{n}\int_{z_{n-1}}^{z}\gamma_{12}(\xi)dz'.\end{aligned} \tag{22}$$

By the definition of ξ and its differential in (5), variables may be changed to express the integral terms in (22) in the form

$$\int_{z_{n-1}}^{z}\gamma(\xi)dz' \;=\; \frac{L_i}{2}\int_{-1}^{\xi}\gamma(\xi')d\xi'. \tag{23}$$

Thus, (22) may be formally integrated from $\xi' = -1$ to ξ, to obtain new coefficients

$$\begin{aligned} g_{01}(\xi) &= \frac{1}{4}\left[\frac{\xi^4}{4} - \frac{3\xi^2}{2} + 2\xi + \frac{13}{4}\right], \\ g_{02}(\xi) &= \frac{-1}{4}\left[\frac{\xi^4}{4} - \frac{3\xi^2}{2} - 2\xi - \frac{3}{4}\right], \\ g_{11}(\xi,L_i) &= \frac{L_i}{8}\left[\frac{\xi^4}{4} - \frac{\xi^3}{3} - \frac{\xi^2}{2} + \xi + \frac{11}{12}\right], \\ g_{12}(\xi,L_i) &= \frac{L_i}{8}\left[\frac{\xi^4}{4} + \frac{\xi^3}{3} - \frac{\xi^2}{2} - \xi - \frac{5}{12}\right], \end{aligned} \tag{24}$$

with values at $\xi = 1$ (i.e., the integrals over a complete finite element from -1 to 1):

$$\begin{aligned} g_{01}(1) &= 1, \\ g_{02}(1) &= 1, \\ g_{11}(1,L_i) &= \frac{L_i}{6}, \quad \text{and} \\ g_{12}(1,L_i) &= \frac{-L_i}{6}. \end{aligned} \tag{25}$$

With substitutions from (23) through (25) and some rearrangement of the terms involved, (22) may be expressed for $z = z_m$, $z_{n-1} \le z_m < z_n$, as

$$w_m\tau(z_m) \;=\; w_m\sum_{i=0}^{n}\left[h_{m,i}\overline{K}_i + h_{m,i+N}\frac{\partial}{\partial z}K_i\right], \tag{26}$$

where

$$h_{mi} = \begin{cases} \dfrac{L_1}{2}g_{01}(\xi), & n=1,\ i=0; \\ \dfrac{L_1}{2}, & n>1,\ i=0; \\ \dfrac{L_i+1+L_i}{2}, & n>1,\ 0<i<n-1; \\ \dfrac{L_n}{2}g_{01}(\xi) + \dfrac{L_n-1}{2}, & n>1,\ i=n-1; \\ \dfrac{L_n}{2}g_{02}(\xi), & i=n; \end{cases} \tag{27}$$

and

$$h_{m,i+N} = \begin{cases} \dfrac{L_1}{2}g_{11}(\xi,L_1), & n=1,\ i=0; \\ \dfrac{L_1^2}{12}, & n>1,\ i=0; \\ \dfrac{L_{i+1}^2 - L_i^2}{12}, & n>1,\ 0<i<n-1; \\ \dfrac{L_n}{2}g_{11}(\xi,L_n) + \dfrac{L_{n-1}^2}{12}, & n>1,\ i=n-1; \\ \dfrac{L_n}{2}g_{12}(\xi,L_n), & i=n. \end{cases} \tag{28}$$

The coefficients w_m in (26) weight the relative importance of each mth measurement in the τ profile. A relatively simple weighting prescription is used at the time of this writing. The weighting coefficient at each depth z_m is first computed as

$$w_m \;=\; \frac{1}{s_0(z_m)}, \tag{29}$$

where $s_0(z_m)$ is the standard deviation of measured deck cell irradiance $E_s(z,\lambda)$ relative to the smoothed profile [computed using (8–15)] over the 10 m depth interval centered at z_m. This weighting gives reduced importance to irradiance measurements made when surface irradiance fluctuates rapidly, e.g., due to variable cloud cover, and increased importance to measurements made when incident irradiance is relatively steady. In depth intervals where both the surface and normalized subsurface irradiance profiles exhibit relatively large amplitude fluctuations, w_m are further multiplied by 10^{-6} to completely discount observations where incident irradiance variations viewed by the deck and underwater radiometers are obviously not in phase.

Ship shadow contamination can be visually recognized in many irradiance profiles measured under overcast conditions. The characteristic shape of this phenomenon is illustrated in Voss et al. (1986). In profiles where ship shadow

is present, the resulting curvature in the upper layer can distort the K and irradiance profile fits over the upper 100 m. In principle, a ship shadow model could be used to correct the profile explicitly, but research to develop and test the implementation of such a method is beyond the scope of the present report. As an interim substitute, multiply the weighting coefficients w_m by 10^{-4} at depths where ship shadow curvature is visually apparent. With the surface layer boundary conditions used at present (see below), this has the effect of passing a straight line to represent $E(z,\lambda)$ from the surface intercept to the depth of the first node selected by the operator, without regard to any curvature that may be apparent in the measured data.

In matrix form, (26) for $m = 1,\ldots,M$ profile observations at depths z_m are combined as

$$\vec{\tau} \;=\; \mathbb{H}\vec{\overline{K}}. \tag{30}$$

The M elements of the vector $\vec{\tau}$ are $\tau_m = w_m\tau(z_m)$, calculated from the data with (18). The elements of the $M\times 2N$ matrix $\mathbb{H}$ are $w_m h_{mi}$, where h_{mi} are defined in (27) for $i \le n$, in (28) for $N \le i \le n+N$, and $h_{mi} = 0$ for $n < i < N$ and $i > n+N$. Finally, the vector $\vec{\overline{K}}$ is defined as

$$\vec{\overline{K}} \;=\; \begin{pmatrix} \overline{K}_0 \\ \overline{K}_1 \\ \vdots \\ \overline{K}_n \\ \vdots \\ \overline{K}_{N-1} \\ \hline \frac{\partial}{\partial z}\overline{K}_0 \\ \frac{\partial}{\partial z}\overline{K}_1 \\ \vdots \\ \frac{\partial}{\partial z}\overline{K}_n \\ \vdots \\ \frac{\partial}{\partial z}\overline{K}_{N-1} \end{pmatrix}, \tag{31}$$

i.e., the unknown vector of attenuation coefficients and their gradients at the N nodes.

As with $\vec{\overline{E}}_s$, $\vec{\overline{K}}$ is determined by the least-squares solution to (30) as

$$\vec{\overline{K}} \;=\; \left[\mathbb{H}^T\mathbb{H}\right]^{-1}\mathbb{H}^T\vec{\tau}, \tag{32}$$

which can be solved using any standard matrix inversion program. In implementation, the singular value decomposition method and computer codes used were given by Press et al. (1992).

To constrain the solution at the surface node, which depends on the entire data profile below it, it is required that

$$\overline{K}_0 \;\equiv\; \overline{K}_1, \tag{33}$$

which implies further that

$$\begin{aligned} \frac{\partial}{\partial z}\overline{K}_0 \;&\equiv\; \frac{\partial}{\partial z}\overline{K}_1, \\ &\equiv\; 0. \end{aligned} \tag{34}$$

In other words, a layer of constant K is imposed between the surface and the depth of the first node selected by the operator.

The bottom boundary values are not constrained, and frequently take on unreasonable values. The solution at the bottom node is determined only by the data in the deepest finite element, when the data values are near the minimum detectable level of the instrument, and consequently are noisy. To minimize the influence of the bottom node on the overall profile, a thin (less than 10 m) bottom element is selected by picking the second deepest node (node index $N-2$) very close to the deepest one (index $N-1$). Then ignored is the fitted curve in this bottom boundary layer simply by dropping node $N-1$ when the fitted K and E curves are calculated using (22) and (30).

This completes the mathematical description of the fitting procedure. In use, the first estimate bin-averaged $E'(z)$ profile is overlaid on the measured $E(z)$ profile on the computer screen. To aid the operator in selecting node depths, profiles of bin-averaged $K'(z)$ and smoothed deck cell irradiance $E_s(z)$ are also displayed. If data from a beam transmissometer or fluorometer are available, the profiles of beam attenuation coefficient $c_p(z)$ and chlorophyll a fluorescence $F(z)$ are displayed as a further guide to selecting node depths. The operator then interactively selects an array of node depths, observes the resulting fit obtained using (18–32), and iteratively adjusts node depths and refined estimates of $E(0^-)$ until a best fit is obtained.

After this procedure has been applied to all radiometer channels, each profile of $K_d(z,\lambda)$, $K_u(z,\lambda)$, and $K_L(z,\lambda)$ is represented by a vector of node depths $\vec{\overline{z}}_n$ and the associated vector $\vec{\overline{K}}$, as given in (31). The fitted curve for each $K(z,\lambda)$ can then be calculated using (22). To calculate the fitted $E_d(z,\lambda)$ profile, (30) is first used to calculate the $t_d(z,\lambda)$ profile and then

$$E_d(z,\lambda) \;=\; E_d(0^-,\lambda)e^{-\tau_d(z,\lambda)}. \tag{35}$$

The same procedure is used to retrieve $E_u(z,\lambda)$ and $L_u(z,\lambda)$ profiles from the Hermitian finite element representation.

Chapter 4

Automated and Interactive Bio-Optical Processing Package

Curtiss O. Davis
W. Joseph Rhea
Naval Research Laboratory, Washington, DC

Abstract

Underwater profiles of upwelling and downwelling irradiance, as well as upwelling radiance have been collected from a wide variety of ocean environments. To obtain apparent optical properties from these data requires removing data spikes, binning and smoothing, and removing possible artifacts from changes in surface illumination, ship shadow, or reflections and wave focusing. To accomplish these data processing requirements, the AIBOP software package was developed. In the AIBOP system, the data is processed in two parts: first, an automated de-spiking and binning routine, and second, interactive spectral processing to remove the effects of changes in surface illumination, ship shadow, or reflection and near-surface effects such as wave focusing. Once the data is processed, routines are provided for calculating extinction coefficients, surface radiance and irradiance values, and remote sensing reflectance.

4.1 INTRODUCTION

Optical data has been collected with a BOPS as part of a number of interdisciplinary oceanographic expeditions, such as, the JGOFS EqPac and Arabian Sea programs. The BOPS records 44 channels of data and extensive processing is required to retrieve AOPs from the measured underwater light fields. To provide accurate, rapid processing of these large data sets, a AIBOP software package written by W. Rhea using IDL from Research Systems, Inc. The full processing of the data was broken down into two distinct levels, the first one being an automated despiking and binning routine, and the second one being a more detailed, user-interactive spectral processing section where underwater optical effects, such as ship shadow, were removed from the data.

The philosophy behind the development of the AIBOP software centered on the desire to process all possible optical casts, not just those made under ideal environmental conditions. Due to the number of different projects competing for wire time during most research cruises, often only one optical cast was made per day. Under these conditions, it is necessary to use all possible data, even if it contains correctable optical contamination, such as intermittent clouds, wave focusing effects, and occasionally ship shadow or ship hull reflection. The AIBOP software was designed specifically to remove as many of these effects as possible.

4.2 INSTRUMENTATION

Optical data were collected with a BOPS, an updated version of the BOPS originally developed by Smith et al. (1984). The package is built around a Biospherical Instruments MER-1048 spectroradiometer, which measures upwelling and downwelling spectral irradiance as well as upwelling spectral radiance. The data collected with the BOPS consists of 44 parameters and includes the following measurements made by the MER:

- 13 channels of downwelling irradiance, E_d, ranging from 410–710 nm;
- 8 channels of upwelling irradiance, E_u, ranging from 410–694 nm;
- 8 channels of upwelling radiance, L_u, ranging from 410–683 nm;
- Photosynthetically available radiation (PAR);
- Depth; and
- Instrument tilt and roll.

In addition, conductivity and temperature were measured with a Sea-Bird CTD, chlorophyll fluorescence was measured with a Sea Tech fluorometer, and beam transmission was measured with a Sea Tech 25 cm transmissometer. Simultaneously, a deck cell collected 4 channels of surface downwelling irradiance, $E_d(0^+)$, ranging from 410–683 nm. The MER acquired all the *in situ* data 16 times a second, averaged it to four records a second, and sent it up the

```
31, 43, 44
******** DATA PROCESSING NOTES *********
Post-cruise (WJR) - Data processed using calibration file listed below.
Initial data-cleaning limited to occasional data spike or gap removal.
Data then binned to 1 meter depths.
09/91 (WJR) - Reprocessed Lu channel using time-averaged comparison between
original calibration (06/11/87) and SDSU/CHORS calibration (07/17/91).
******** VERTICAL CAST CASTCARD ********
FILE w910321a; 03-21-1991
CRUISE IDENTIFICATION.....  WHITE POINT OUTFALL - 03/91
CALIBRATION FILE.........8302W10a.cfl
CALFILE DESC.............MER-1048-8302 Recalibrated for JPL 12 MAR 1991
NAME.................w910321a
DATE.....................03-21-1991
STATION..................STA 1
Position.............LONG:118-20.41 W
.....................LAT :33-41.20 N
SKY CONDITION............CLEAR
OPERATOR NAME............WJR
SUN POSITION.............2
HANDSHAKE.................  1
ANALOG CHANNELS...........  35
FREQUENCY AVERAGED........  1023
ANALOG CYCLES AVERAGED....  4
START TIME...............12:23:41
DOWNCAST ENDING MARKED AT RECORD 1391
UPCAST ENDING MARKED AT RECORD 2423
FINAL TIME...............12:35:25
TRANSMISSION ERRORS.......  0
NORMAL TERMINATION OF DATA LOGGING.
TOTAL RECORDS RECORDED....  2462
Record,Ed410,Ed441,Ed488,Ed520,Ed550,...
4,102.0160,118.3141,143.5586,138.1729,...
```

Fig. 31. An example of a working data file.

cable to a deck box and a PC which stored the data on a hard disk.

4.3 LEVEL-1 PROCESSING

The first level of processing the BOPS data began with a decision to use either the downcast or upcast, depending upon various criteria including absence of clouds in the data, absence of ship shadow, and absence of data spikes or dropouts cause by occasional pauses in the data transmission from the MER to the onboard computer. The next step was an automated process to remove any remaining data spikes or dropouts from the selected cast data and replace them (typically single values) with interpolated values.

The data was then checked for single points lying outside 3σ of a 7-point bin, and any outlying points were then replaced with interpolated values. This was done to reduce much of the effects caused by wave focusing in clear waters. This cleaned data was then mean-binned into 1 m intervals, centered on the half meter. This completed the level-1 processing.

4.4 LEVEL-2 PROCESSING

The level-2 processing involved interactive spectral processing of the data. First, ship roll was removed from surface light channels (when necessary) by applying a seven-point running mean filter to each of the four surface light channels. Next, cloud effects were removed from the underwater light field by normalizing each underwater optical channel to either the mean or maximum of the closest matching surface light wavelength. The decision whether to use the mean or maximum of surface light value depended on the nature of the light field during the cast. In general, the maximum value was used when the sky was either very clear or fully overcast. The mean value was used only during partly cloudy conditions where bright clouds caused a brief increase in measured light levels on either side of the cloud with a shadow in the middle. In these cases, the mean light value more closely matched the overall clear-sky light levels than did the maximum light value.

Also, when needed, the surface light channel records were shifted slightly in time before normalizing the underwater data to account for the difference between the time a cloud passed over the surface and underwater arrays. This

```
52, 43, 44
33.68667,-118.34016, 80.51598, 80.84930
================================BEGIN_HEADER================================
DESCRIPTION OF FIRST LINE IN FILE (BEFORE HEADER):
Number of Header Records in this File
Number of Data Records following this header
Number of Columns within each Data Record
DESCRIPTION OF SECOND LINE IN FILE (BEFORE HEADER):
Latitude of Cast (Degrees; South=[-]; North=[+])
Longitude of Cast (Degrees; West=[-]; East=[+])
Date and Local Time of Cast (Julian Day + Local Time in percent of 24hr)
Date and G.M. Time of Cast (Julian Day + G.M. Time in percent of 24hr)
================================CAST_INFO====================================
Filename---------------------->,w910321a.mer
Cruise Identification---------->,WHITE POINT OUTFALL - 03/91
Station Identification--------->,STA 1
Date of Cast (Mon/Day/Year)---->,03-21-1991
Local Start Time (Hr:Min:Sec)-->,12:23:41
Latitude (Degrees Minutes )---->, 33-41.20 N
Longitude (Degrees Minutes)---->,118-20.41 W
Sky State During Cast---------->,CLEAR
============================PROCESSING_NOTES================================
Post-cruise (WJR) - Data processed using calibration file listed below.
Initial data-cleaning limited to occasional data spike or gap removal.
Data then binned to 1 meter depths.
09/91 (WJR) - Reprocessed Lu channel using time-averaged comparison between
original calibration (06/11/87) and SDSU/CHORS calibration (07/17/91).
05/93 (WJR) - Ship-roll removed from all surface (Deck) channels.
05/93 (WJR) - All optical channels normalized to max surface (Deck) channels.
05/93 (WJR) - All optical channels smoothed to remove wave effects.
05/93 (WJR) - Ship shadow/reflection removed from affected optical channels.
08/93 (WJR) - %Transmission corrected by new calibration
08/93 (WJR) - %Transmission converted to Beam Attenuation
========================DATA_COLUMN_DESCRIPTIONS============================
Column, Column_Title, Description
--------------------------------------------------------------------------------
0, Depth, Mean Depth of 1-meter record bin (meters)
1, Pts/m, Number of points averaged per bin (0=interpolated data)
2, Tilt_, Instrument Tilt (degrees; range -45 to 45)
3, Roll_, Instrument Roll (degrees; range -45 to 45)
4, TempC, Water Temperature (Deg C)
5, S_ppt, Calculated Salinity (PPT)
6, Cond_, Measured Conductivity
7, Sigma, Calculated Water Density
8, BeamC, Beam Attenuation Coefficient from 25cm Transmissometer
9, Fluor, Stimulated Fluoresence (Fluoro units; range 0 to 100)
10, PARuw, Downwelling Scalar PAR at depth (E17 quanta/sec/cm2)
11-23, Ed410-Ed710, Downwelling Spectral Irradiance at depth (uW/cm2/nm)
24-31, Eu410-Eu469, Upwelling Spectral Irradiance at depth (uW/cm2/nm)
32-39, Lu410-Lu683, Upwelling Spectral Radiance at depth (uW/cm2/nm/str)
40-43, E+410-E+683, Spectral Irradiance above sea surface (uW/cm2/nm)
============================DATA_COLUMN_TITLES==============================
Depth,Pts/m,Tilt_,Roll_,TempC,S_ppt,Cond_,Sigma,BeamC,Fluor,PARuw,Ed410,...
================================END_HEADER==================================
0.50000, 0.00000, 1.81487, 5.48543, 0.00000, 0.00000, 0.00000, ...
```

Fig. 32. An example of a final data file.

shifting was used only for normalizing and was not applied to the final surface light data. The next processing step was to smooth out sea-surface wave effects from underwater optical channels by applying either a three-, five-, or seven-point boxcar mean filter to all underwater optical channels.

As a final step in casts where obvious effects such as ship shadow, ship hull reflection, or wave focusing were present in the downwelling irradiance (E_d) data, the upper (shallow) portion of each affected E_d channel was replaced with extrapolated, or curve-fit data. This was accomplished using a automated program that makes use of the lower non-shadowed optical data and finds the most accurate extrapolation to a predefined surface value estimated from the deck cell data. The extrapolation was carried out using a least-squares polynomial fit performed in log space. For those underwater E_d channels where there was no corresponding above-water $E_d(0^+)$ channel, estimated $E_d(0^+)$ values were automatically calculated using `RADTRAN` (Gregg and Carder 1990) for the time, day, location, and sky conditions.

4.5 CALCULATION OF *K*

The diffuse attenuation coefficient for downwelling irradiance (K_d) was calculated from the E_d profile using a least-squares fit of the log-transformed data (Smith and Baker 1894). A 9 m window ($z \pm 4$ m) was used for calculating K_d at each depth level. These K_d values were not stored but rather were calculated on demand when requested. Whenever measured chlorophyll and phaeopigment data were available, the calculated K_d values were overplotted with K_d values as predicted by the model of Morel (1988).

4.6 DATA FILE FORMATS

There are two file formats used by the AIBOP software package. The first is a *working format* (Fig. 31), which is used by the software during all of the processing steps. This format keeps the data in the same configuration as output by Biospherical Instruments data collection software. The second format is a *final format* (Fig. 32) which is distributed to the public. The final format differs from the working format in several ways:

- The data column are rearranged in a more logical order (e.g., having depth as the first column),
- Percent transmission from the transmissometer is converted to beam attenuation, and
- Greenwich Mean Time (GMT) is calculated for each cast and is shown along with local time.

Also a special *plotting* line is added which can aid in quickly determining the exact location and time of each cast. All files are in comma-separated ASCII for ease of reading by others.

4.7 LOG FILES

A log file was automatically created for each cast which lists all of the level-2 spectral processing steps in the order they were performed. The log file (Fig. 33) allows for later recreation of the processed data, as well as serving as a permanent record of the processing session. These log files are stored separately from the data files but are available to anyone requesting them.

```
MER OPTICAL PROCESSING LOG FILE
FOR: w910321a.mer
BY: WJR DATE: 05/93

PROCESSING PERFORMED ON ALL OPTICAL CHANNELS:
REMOVED_SHIP_ROLL_FROM_SURFACE
NORMALIZED_UW_TO_SURF_MAXIMUM
REMOVED_UW_WAVE_EFFECTS_(5PTS)
INDIVIDUAL OPTICAL CHANNELS PROCESSED:
1, (Ed 410), SHADOW_REMOVED_(7,13)
2, (Ed 441), SHADOW_REMOVED_(7,13)
3, (Ed 488), SHADOW_REMOVED_(11,15)
4, (Ed 520), SHADOW_REMOVED_(7,17)
5, (Ed 550), SHADOW_REMOVED_(3,13)
6, (Ed 560), SHADOW_REMOVED_(10,16)
7, (Ed 589), SHADOW_REMOVED_(5,13)
8, (Ed 633), SHADOW_REMOVED_(9,19)
9, (Ed 656), SHADOW_REMOVED_(7,15)
10, (Ed 671), SHADOW_REMOVED_(3,9)
11, (Ed 683), SHADOW_REMOVED_(2,12)
12, (Ed 694), SHADOW_REMOVED_(2,10)
13, (Ed 710), SHADOW_REMOVED_(2,10)
17, (Lu 410), NOT PROCESSED
18, (Lu 441), NOT PROCESSED
19, (Lu 488), NOT PROCESSED
20, (Lu 520), NOT PROCESSED
21, (Lu 550), NOT PROCESSED
22, (Lu 633), NOT PROCESSED
23, (Lu 656), NOT PROCESSED
24, (Lu 683), NOT PROCESSED
25, (Eu 410), NOT PROCESSED
26, (Eu 441), NOT PROCESSED
27, (Eu 488), NOT PROCESSED
28, (Eu 520), NOT PROCESSED
29, (Eu 550), NOT PROCESSED
30, (Eu 589), NOT PROCESSED
31, (Eu 671), NOT PROCESSED
32, (Eu 694), NOT PROCESSED
35, (PAR uw), NOT PROCESSED
END OF MER OPTICAL PROCESSING LOG FILE
```

Fig. 33. An example of a log file.

Chapter 5

The SIO Method

Eric A. Brody
University of California, Santa Barbara, Santa Barbara, California

Abstract

The SIO group has employed a bulk method for deriving AOPs from spectroradiometry profiles. The bulk approach has been long employed in the past and much of what is known about AOPs is a result of using this approach. The bulk method has been used in the past by the SIO group, although, they are not doing so presently. The bulk approach fits a straight line to the log-transformed irradiance and radiance profiles within the oceanic mixed layer. The fluxes just below the sea surface are estimated from the exponentiated intercept and the slope gives a mixed layer averaged diffuse attenuation coefficient, $K_d(z_0, \lambda)$. This method provides only a single estimate of $K_d(z_0, \lambda)$ and cannot be used to determine the depth dependence of $K_d(z, \lambda)$. One distinct advantage of the bulk method is that it can easily be applied using any spreadsheet program on a modest computer (PC).

5.1 INTRODUCTION

For the SIO MER-1012 data, a very simple and conservative method, based on the traditional Smith and Baker (1984 and 1986) method, was used. Now with the new MER-2040 and the addition of spectral irradiance above the surface, this approach is no longer employed and a switch to the BBOP method has been made. A summary of the data processing methodology is given below.

5.2 DATA PROCESSING

Preparation of the data includes averaging the data to a 1 m bins and calculating the mixed-layer depth by visually inspecting the temperature, salinity, and beam attenuation data. In addition, an inspection for ship shadows, wave focusing, and surface glitter is made to determine the shallowest *good depth*. Sometimes the deepest depth is not the base of the mixed layer, but the depth at which the downwelling irradiance becames less than 10 times the noise levels. This is especially important when solar zenith angles are large, or cloudy conditions cause minimal surface flux.

In addition, the surface PAR (E_0 PAR) is checked to be *more or less* constant during the profiling. If PAR is less than $0.1\times10^{16}\,\mathrm{Q\,cm^{-2}\,s^{-1}}$ or varied *too much*, then the data is rejected. Since surface irradiance for each channel was not available, the data was not normalized to the surface as outlined by Smith and Baker (1984).

Using the (visually) selected shallowest and deepest depths, a least-squares regression fit is applied to the depth versus the natural log of a given channel (see for example, Smith and Baker 1984 and 1986). The slope is the derived diffuse attenuation coefficient (K) for the mixed layer depth and the exponential of the intercept is the data extropolated to just below the surface ($z = 0^-$). The ratio of water leaving radiance to downwelling irradiance just below the surface, $L_w(0^-)$:$E_d(0^-)$, is the remote sensing reflectance, $R_{rs}(0^-)$. The Fresnel coefficient is not used to get values at ($z = 0^+$).

Verifcation of the data involves correlating the mixed layer depth chlorophyll and phaeopigment or particle absorption with the $R_{rs}(0^-)$ and K for the mixed layer depth and comparing it to the algorithms (Gordon et al. 1988; Smith and Baker 1984 and 1986).

Editors' Note: Although this Chapter is not as detailed as the others, the editors' thank the author for making an effort to make up for a lack of material from the SIO group.

Appendix A

Attendees to the First SeaWiFS Data Analysis Round-Robin (DARR-94)

The attendees to DARR-94 are presented alphabetically.

Karen Baker
UCSD/SIO
La Jolla, CA 92093
Voice: 619–534–2350
Fax: 619–534–2996
Net: karen@icess.ucsb.edu

Eric Brody
UCSB/ICESS
Santa Barbara, CA 93106
Voice: 805–893–4449
Fax: 805–893–2578
Net: ebrody@icess.ucsb.edu

Curtiss Davis
Naval Research Laboratory
Code 7212
Washington, DC 20375
Voice: 202–767–9296
Fax: 202–404–7453
Net: davis@rira.nrl.navy.mil

Vincent Fournier-Sicre
UCSD/Scripps Oceanography
La Jolla, CA 92093–0218
Voice: 619–534–8947
Fax: 619–534–2997
Net: fournier@spode.ucsd.edu

Stanford Hooker
NASA/GSFC/Code 970.2
Greenbelt, MD 20771
Voice: 301–286–9503
Fax: 301–286–1775
Net: stan@ardbeg.gsfc.nasa.gov

John Morrow
Biospherical Instruments, Inc.
5340 Riley Street
San Diego, CA 92110
Voice: 619–686–1888
Fax: 619–686–1887
Net: morrow@biospherical.com

James Mueller
SDSU/CHORS/Suite 206
6505 Alvarado Road
San Diego, CA 92120–5005
Voice: 619–594–2230
Fax: 619–594–4570
Net: jim@chors.sdsu.edu

Margaret O'Brien
UCSB/ICESS
Santa Barbara, CA 93106
Voice: 805–893–2544
Fax: 805–893–2578
Net: mob@icess.ucsb.edu

W. Joseph Rhea
Naval Research Laboratory
Code 7212
Washington, D.C. 20375
Voice: 202–767–9296
Fax: 202–404–7453
Net: rhea@riva.nrl.navy.mil

Dave Siegel
UCSB/ICESS
Santa Barbara, CA 93106
Voice: 805–893–4547
805–893–2544
Fax: 805–893–2578
Net: davey@icess.ucsb.edu

Ray Smith
UCSB/ICESS
Santa Barbara, CA 93106
Voice: 805–893–4709
Fax: 805–893–2578
Net: ray@icess.ucsb.edu

Jens Sorensen
UCSB/ICESS
Santa Barbara, CA 93106
Voice: 805–893–4449
Fax: 805–893–2578
Net: jens@icess.ucsb.edu

Glossary

AIBOP	Automated and Interactive Bio-Optical Processing
ANSI	American National Standards Institute
AOP	Apparent Optical Property
ASCII	American Standard Code for Information Interchange
BATS	Bermuda Atlantic Time-Series Station
BBOP	Bermuda Bio-Optics Project
BOPS	Bio-Optical Profiling System
CalCoFI	California Cooperative Fisheries Institute
CHORS	Center for Hydro-Optics and Remote Sensing (San Diego State University)
COARE	Coupled Ocean-Atmosphere Response Experiment
CTD	Conductivity, Temperature, and Depth
c.v.	coefficient of variation
CVT	Calibration and Validation Team
DAAC	Distributed Active Archive Center
DARR	Data Analysis Round-Robin
DARR-94	The First DARR (July 1994)
DEC	Digital Equipment Corporation
EC	Excluding CHORS (data)
EqPac	Equatorial Pacific (Process Study)
FORTRAN	Formula Translation (computer language)
ftp	file transfer protocol
GLOBEC	Global Ocean Ecosystems
GMT	Greenwich Mean TIme
`gcc`	GNU C Compiler
GNU	GNU's not UNIX
GOMEX	Gulf of Mexico Experiment
GSFC	Goddard Space Flight Center
GUI	Graphical User Interface

IBM International Business Machines
ICESS Institute for Computational Earth System Science (University of California at Santa Barbara)
IDL Interactive Data Language
IRIX Not an acronym, a computer operating system.

JGOFS Joint Global Ocean Flux Study

KQ K_d Quality (flag)

LCD Least Common Denominator (file)

MER Marine Environmental Radiometer
MOBY Marine Optical Buoy

NASA National Aeronautics and Space Administration
NRL Naval Research Laboratory
NSF National Science Foundation

PAR Photosynthetically Available Radiation
PC (IBM) Personal Computer

rms root mean squared

SDSU San Diego State University
SeaBASS SeaWiFS Bio-Optical Archive and Storage System
SeaWiFS Sea-viewing Wide Field-of-view Sensor
SGI Silicon Graphics, Incorporated
SIO Scripps Institution of Oceanography
SIRREX SeaWiFS Intercalibration Round-Robin Experiment
SNR Signal-to-Noise Ratio
SUN Sun Microsystems
SXR SeaWiFS Transfer Radiometer

TOGA Tropical Ocean Global Atmosphere program

UCSB University of California at Santa Barbara
UNESCO United Nations Educational, Scientific, and Cultural Organizations
UNIX Not an acronym, a computer operating system.

WOCE World Ocean Circulation Experiment

Symbols

$A_d(\overline{z},\lambda)$ Linear regression intercepts at the center of a fitted depth interval for ln of $A_d(z,\lambda)$ defined in (17).
$A_u(\overline{z},\lambda)$ Linear regression intercepts at the center of a fitted depth interval for ln of $A_u(z,\lambda)$ defined in (17).
$A_l(\overline{z},\lambda)$ Linear regression intercepts at the center of a fitted depth interval for ln of $A_l(z,\lambda)$ defined in (17).

$E(\lambda)$ Spectral irradiance.
$E_d(0^-,\lambda)$ Incident downwelling spectral irradiance just beneath the sea surface.
$E_d(z,\lambda)$ Incident downwelling spectral irradiance profile.
$E_s(z,\lambda)$ Vertical profile of surface irradiance.
$\overline{E}_{s,i}(\lambda)$ The value of $E_s(z,\lambda)$ at node depth z_i.
$\vec{E}_s(z_m,\lambda)$ Defined as $\mathbb{H}\vec{\overline{E}}_s(\lambda)$.
$\vec{E}_s(\lambda)$ The measured irradiance vector of length M.
$E_u(0^-,\lambda)$ Upwelling spectral irradiance just beneath the sea surface.
$E_u(z,\lambda)$ Upwelling spectral irradiance profile.

g_{ij} Integrals of γ_{ij}, defined in (24).

h_{mj} Matrix elements defined in (28).
$\mathbb{H}$ Matrix of coefficients $[h_{mj}]$.

K Diffuse attenuation coefficient.
$K_d(z,\lambda)$ Vertical profile of the diffuse attenuation coefficient for the downwelling irradiance spectrum.
$K'_d(z,\lambda)$ $K_d(z,\lambda)$ determined by least squares regression over a depth interval.
$K_L(z,\lambda)$ Vertical profile of the diffuse attenuation coefficient for the upwelling radiance spectrum.
$K'_L(z,\lambda)$ $K_L(z,\lambda)$ determined by least squares regression over a depth interval.
$K_u(z,\lambda)$ Vertical profile of the diffuse attenuation coefficient for the upwelling irradiance spectrum.
$K'_u(z,\lambda)$ $K_u(z,\lambda)$ determined by least squares regression over a depth interval.

L_i The length of the ith element.
$L_u(0^-,\lambda)$ Upwelling spectral radiance just beneath the sea surface.
$L_u(z,\lambda)$ Upwelling spectral radiance profile.

M Total number of discrete data points in a vertical radiometeric profile.

N The number of node depths.

$R_{rs}(z,\lambda)$ Vertical profile of the remote sensing reflectance spectrum.

w_m The weighting coefficient at each depth z_m.

z The vertical coordinate.
z_i The depth of a particular node.
z_m The depth of the mth data point in a vertical radiometric profile.
z_n The node depth number ($n = 0,\ldots,N-1$).

γ_{ij} Hermitian cubic basis function.

λ Wavelength of light.

ξ A local depth coordinate ranging from -1 at node z_{i-1} to $+1$ at node z_i.

σ One standard deviation.
σ_t The density of sea water determined from the *in situ* salinity and temperature, but at atmospheric pressure.
σ_θ The density of sea water determined from the *in situ* salinity and the potential temperature (θ), but at atmospheric pressure.

$\hat{\tau}(z,\lambda)$ The estimated vertical profile of the spectral optical depth.
$\tau(z,\lambda)$ Vertical profile of the spectral optical depth.

References

Dera, J., and H.R. Gordon, 1968: Light field fluctuations in the photic zone. *Limnol. Oceanogr.,* **13,** 697–699.

Dickey, T.D., and D.A. Siegel, (Eds.), 1993: *Bio-Optics in U.S. JGOFS.* Report of the Bio-Optics Workshop, U.S. JGOFS Planning and Coordination Office, Woods Hole, Massachusettes, 180 pp.

Gordon, H.R., J.M. Smith, and O.B. Brown, 1971: Spectra of underwater light-field fluctuations in the photic zone. *Bull. Mar. Sci.,* **21,** 466–470.

——, O.B. Brown, R.H. Evans, J.W. Brown, R.C. Smith, K.S. Baker, and D.K. Clark, 1988: A semianalytic radiance model of ocean color. *J. of Geophys. Res.,* **93,** 10,909–10,924.

Gregg, W.W., and K.L. Carder, 1990: A simple spectral solar irradiance model for cloudless maritime atmospheres. *Limnol. Oceanogr.,* **35,** 1,657–1,675.

Hooker, S.B., W.E. Esaias, G.C. Feldman, W.W. Gregg, and C.R. McClain, 1992: An Overview of SeaWiFS and Ocean Color. *NASA Tech. Memo. 104566, Vol. 1,* S.B. Hooker and E.R. Firestone, Eds., NASA Goddard Space Flight Center, Greenbelt, Maryland, 24 pp., plus color plates.

——, C.R. McClain, J.K. Firestone, T.L. Westphal, E-n. Yeh, and Y. Ge, 1994: The SeaWiFS Bio-Optical Archive and Storage System (SeaBASS), Part 1. *NASA Tech. Memo. 104566, Vol. 20,* S.B. Hooker and E.R. Firestone, Eds., NASA Goddard Space Flight Center, Greenbelt, Maryland, 40 pp.

McClain, C.R., W.E. Esaias, W. Barnes, B. Guenther, D. Endres, S. Hooker, G. Mitchell, and R. Barnes, 1992: Calibration and Validation Plan for SeaWiFS. *NASA Tech. Memo. 104566, Vol. 3,* S.B. Hooker and E.R. Firestone, Eds., NASA Goddard Space Flight Center, Greenbelt, Maryland, 41 pp.

——, G. Feldman, and W. Esaias, 1993: Oceanic primary production. *Global Change Atlas,* C. Parkinson, J. Foster, and R. Gurney, Eds., Cambridge University Press, 251–263.

Mitchell, B.G., and O. Holm-Hansen, 1991: Bio-optical properties of the Antarctic Peninsula waters: Differentiation from temperate ocean models. *Deep-Sea Res.,* **38,** 1,009–1,029.

Morel, A., 1988: Optical modeling of the upper ocean in relation to its biogenous matter content (case I waters). *J. Geophys. Res.,* **93,** 10,749–10,768.

Mueller, J.L., 1993: The First SeaWiFS Intercalibration Round-Robin Experiment, SIRREX-1, July 1992. *NASA Tech. Memo. 104566, Vol. 14,* S.B. Hooker and E.R. Firestone, Eds., NASA Goddard Space Flight Center, Greenbelt, Maryland, 60 pp.

——, and R.W. Austin, 1992: Ocean Optics Protocols for SeaWiFS Validation. *NASA Tech. Memo. 104566, Vol. 5,* S.B. Hooker and E.R. Firestone, Eds., NASA Goddard Space Flight Center, Greenbelt, Maryland, 43 pp.

——, and ——, 1995: Ocean Optics Protocols for SeaWiFS Validation, Revision 1. *NASA Tech. Memo. 104566, Vol. 25,* S.B. Hooker, E.R. Firestone, and J.G. Acker, Eds., NASA Goddard Space Flight Center, Greenbelt, Maryland, 66 pp.

Press, W.H., S.A. Tuekolsky, W.T. Vettering, and B.P. Flannery, 1992: *Numerical Recipes in C: The Art of Scientific Computing.* Cambridge University Press, 994 pp.

Santoreli, R., S. Marallo, and E. Böhm, 1991: An objective analysis scheme for AVHRR imagery. *Int. J. Remote Sens.,* **12,** 681–693.

Siegel, D.A., and T.D. Dickey, 1987: Observations of the vertical structure of the diffuse attenuation coefficient spectrum. *Deep-Sea Res.,* **34,** 547–563.

——, and ——, 1988: Characterization of high-frequency downwelling irradiance fluctuations. *Ocean Optics IX,* **925,** 67–74.

——, A.F. Michaels, J. Sorensen, M.C. O'Brien, and M. Hammer, 1995a: Seasonal variability of light availability and its utilization in the Sargasso Sea. *J. Geophys. Res.,* (in press).

——, M.C. O'Brien, J.C. Sorensen, D. Konnoff, and E. Fields, 1995b: *BBOP Sampling and Data Processing Protocols.* U.S. JGOFS Planning and Coordination Office, Woods Hole, Massachusettes, 79 pp.

Smith, R.C., 1974: Structure of the solar radiation in the upper layers of the sea. *Optical Aspects of Oceanography.* N.G. Jerlov and E. Steemann-Neilsen, Eds., Academic Press, 95–119.

——, and K.S. Baker, 1978a: The bio-optical state of ocean waters and remote sensing. *Limnol. Oceanogr,* **23,** 247–259.

——, and ——, 1978b: Optical classification of natural waters. *Limnol. Oceanogr.,* **23,** 260–267.

——, and ——, 1984: The analysis of ocean optical data. *Ocean Optics VII,* SPIE, **489,** 95–126.

——, C.R. Booth, and J.L. Star, 1984: Oceanographic bio-optical profiling system. *Appl. Opt.,* **23,** 2,791–2,797.

——, and K.S. Baker, 1986: Analysis of ocean optical data. *Ocean Optics VIII,* SPIE, **637,** 95–107.

Snyder, R.L., and J. Dera, 1970: Wave-induced light-field fluctuations in the sea. *J. Opt. Soc. Am.,* **60,** 1,072–1,079.

Sorensen, J., D. Konnoff, M.C. O'Brien, E. Fields, and D.A. Siegel, 1994: The BBOP data processing system. *Ocean Optics XII,* SPIE, **2,258,** 539–546.

Stramski, D., C.R. Booth, and B.G. Mitchell, 1992: Estimation of the downward irradiance attenuation from a single mooring instrument. *Deep-Sea Res.,* **39,** 567–584.

Strickland, J.D.H., 1958: Solar radiation penetrating the ocean: A review of requirements, data and methods of measurement, with particular reference to photosynthetic production. *J. Fish. Bd. Can.,* **15,** 453–493.

Tyler, J.E., and R.C. Smith, 1970: *Measurement of Spectral Irradiance Underwater.* Gordon and Breech Sci. Publ., New York, 103 pp.

Voss, K.J., 1989: Use of the radiance distribution to measure the optical absorption coefficient in the ocean. *Limnol. Oceanogr.,* **34,** 1,614–1,622.

——, J.W. Nolten, and G.D. Edwards, 1986: Ship shadow effects on apparent optical properties. *Ocean Optics VIII,* SPIE, **637,** 186–190.

Weir, C., D.A. Siegel, A.F. Michaels, and D. Menzies, 1994: An *in situ* evaluation of a ship's shadow. *Ocean Optics XII,* SPIE, **2,258,** 815–821.

The SeaWiFS Technical Report Series

Vol. 1

Hooker, S.B., W.E. Esaias, G.C. Feldman, W.W. Gregg, and C.R. McClain, 1992: An Overview of SeaWiFS and Ocean Color. *NASA Tech. Memo. 104566, Vol. 1,* S.B. Hooker and E.R. Firestone, Eds., NASA Goddard Space Flight Center, Greenbelt, Maryland, 24 pp., plus color plates.

Vol. 2

Gregg, W.W., 1992: Analysis of Orbit Selection for SeaWiFS: Ascending vs. Descending Node. *NASA Tech. Memo. 104566, Vol. 2,* S.B. Hooker and E.R. Firestone, Eds., NASA Goddard Space Flight Center, Greenbelt, Maryland, 16 pp.

Vol. 3

McClain, C.R., W.E. Esaias, W. Barnes, B. Guenther, D. Endres, S. Hooker, G. Mitchell, and R. Barnes, 1992: Calibration and Validation Plan for SeaWiFS. *NASA Tech. Memo. 104566, Vol. 3,* S.B. Hooker and E.R. Firestone, Eds., NASA Goddard Space Flight Center, Greenbelt, Maryland, 41 pp.

Vol. 4

McClain, C.R., E. Yeh, and G. Fu, 1992: An Analysis of GAC Sampling Algorithms: A Case Study. *NASA Tech. Memo. 104566, Vol. 4,* S.B. Hooker and E.R. Firestone, Eds., NASA Goddard Space Flight Center, Greenbelt, Maryland, 22 pp., plus color plates.

Vol. 5

Mueller, J.L., and R.W. Austin, 1992: Ocean Optics Protocols for SeaWiFS Validation. *NASA Tech. Memo. 104566, Vol. 5,* S.B. Hooker and E.R. Firestone, Eds., NASA Goddard Space Flight Center, Greenbelt, Maryland, 43 pp.

Vol. 6

Firestone, E.R., and S.B. Hooker, 1992: SeaWiFS Technical Report Series Summary Index: Volumes 1–5. *NASA Tech. Memo. 104566, Vol. 6,* S.B. Hooker and E.R. Firestone, Eds., NASA Goddard Space Flight Center, Greenbelt, Maryland, 9 pp.

Vol. 7

Darzi, M., 1992: Cloud Screening for Polar Orbiting Visible and IR Satellite Sensors. *NASA Tech. Memo. 104566, Vol. 7,* S.B. Hooker and E.R. Firestone, Eds., NASA Goddard Space Flight Center, Greenbelt, Maryland, 7 pp.

Vol. 8

Hooker, S.B., W.E. Esaias, and L.A. Rexrode, 1993: Proceedings of the First SeaWiFS Science Team Meeting. *NASA Tech. Memo. 104566, Vol. 8,* S.B. Hooker and E.R. Firestone, Eds., NASA Goddard Space Flight Center, Greenbelt, Maryland, 61 pp.

Vol. 9

Gregg, W.W., F.C. Chen, A.L. Mezaache, J.D. Chen, J.A. Whiting, 1993: The Simulated SeaWiFS Data Set, Version 1. *NASA Tech. Memo. 104566, Vol. 9,* S.B. Hooker, E.R. Firestone, and A.W. Indest, Eds., NASA Goddard Space Flight Center, Greenbelt, Maryland, 17 pp.

Vol. 10

Woodward, R.H., R.A. Barnes, C.R. McClain, W.E. Esaias, W.L. Barnes, and A.T. Mecherikunnel, 1993: Modeling of the SeaWiFS Solar and Lunar Observations. *NASA Tech. Memo. 104566, Vol. 10,* S.B. Hooker and E.R. Firestone, Eds., NASA Goddard Space Flight Center, Greenbelt, Maryland, 26 pp.

Vol. 11

Patt, F.S., C.M. Hoisington, W.W. Gregg, and P.L. Coronado, 1993: Analysis of Selected Orbit Propagation Models for the SeaWiFS Mission. *NASA Tech. Memo. 104566, Vol. 11,* S.B. Hooker, E.R. Firestone, and A.W. Indest, Eds., NASA Goddard Space Flight Center, Greenbelt, Maryland, 16 pp.

Vol. 12

Firestone, E.R., and S.B. Hooker, 1993: SeaWiFS Technical Report Series Summary Index: Volumes 1–11. *NASA Tech. Memo. 104566, Vol. 12,* S.B. Hooker and E.R. Firestone, Eds., NASA Goddard Space Flight Center, Greenbelt, Maryland, 28 pp.

Vol. 13

McClain, C.R., K.R. Arrigo, J. Comiso, R. Fraser, M. Darzi, J.K. Firestone, B. Schieber, E-n. Yeh, and C.W. Sullivan, 1994: Case Studies for SeaWiFS Calibration and Validation, Part 1. *NASA Tech. Memo. 104566, Vol. 13,* S.B. Hooker and E.R. Firestone, Eds., NASA Goddard Space Flight Center, Greenbelt, Maryland, 52 pp., plus color plates.

Vol. 14

Mueller, J.L., 1993: The First SeaWiFS Intercalibration Round-Robin Experiment, SIRREX-1, July 1992. *NASA Tech. Memo. 104566, Vol. 14,* S.B. Hooker and E.R. Firestone, Eds., NASA Goddard Space Flight Center, Greenbelt, Maryland, 60 pp.

Vol. 15

Gregg, W.W., F.S. Patt, and R.H. Woodward, 1994: The Simulated SeaWiFS Data Set, Version 2. *NASA Tech. Memo. 104566, Vol. 15,* S.B. Hooker and E.R. Firestone, Eds., NASA Goddard Space Flight Center, Greenbelt, Maryland, 42 pp., plus color plates.

Vol. 16

Mueller, J.L., B.C. Johnson, C.L. Cromer, J.W. Cooper, J.T. McLean, S.B. Hooker, and T.L. Westphal, 1994: The Second SeaWiFS Intercalibration Round-Robin Experiment, SIRREX-2, June 1993. *NASA Tech. Memo. 104566, Vol. 16,* S.B. Hooker and E.R. Firestone, Eds., NASA Goddard Space Flight Center, Greenbelt, Maryland, 121 pp.

Vol. 17

Abbott, M.R., O.B. Brown, H.R. Gordon, K.L. Carder, R.E. Evans, F.E. Muller-Karger, and W.E. Esaias, 1994: Ocean Color in the 21st Century: A Strategy for a 20-Year Time Series. *NASA Tech. Memo. 104566, Vol. 17,* S.B. Hooker and E.R. Firestone, Eds., NASA Goddard Space Flight Center, Greenbelt, Maryland, 20 pp.

Vol. 18

Firestone, E.R., and S.B. Hooker, 1994: SeaWiFS Technical Report Series Summary Index: Volumes 1–17. *NASA Tech. Memo. 104566, Vol. 18,* S.B. Hooker and E.R. Firestone, Eds., NASA Goddard Space Flight Center, Greenbelt, Maryland, 47 pp.

Vol. 19

McClain, C.R., R.S. Fraser, J.T. McLean, M. Darzi, J.K. Firestone, F.S. Patt, B.D. Schieber, R.H. Woodward, E-n. Yeh, S. Mattoo, S.F. Biggar, P.N. Slater, K.J. Thome, A.W. Holmes, R.A. Barnes, and K.J. Voss, 1994: Case Studies for SeaWiFS Calibration and Validation, Part 2. *NASA Tech. Memo. 104566, Vol. 19,* S.B. Hooker, E.R. Firestone, and J.G. Acker, Eds., NASA Goddard Space Flight Center, Greenbelt, Maryland, 73 pp.

Vol. 20

Hooker, S.B., C.R. McClain, J.K. Firestone, T.L. Westphal, E-n. Yeh, and Y. Ge, 1994: The SeaWiFS Bio-Optical Archive and Storage System (SeaBASS), Part 1. *NASA Tech. Memo. 104566, Vol. 20,* S.B. Hooker and E.R. Firestone, Eds., NASA Goddard Space Flight Center, Greenbelt, Maryland, 40 pp.

Vol. 21

Acker, J.G., 1994: The Heritage of SeaWiFS: A Retrospective on the CZCS NIMBUS Experiment Team (NET) Program. *NASA Tech. Memo. 104566, Vol. 21,* S.B. Hooker and E.R. Firestone, Eds., NASA Goddard Space Flight Center, Greenbelt, Maryland, 43 pp.

Vol. 22

Barnes, R.A., W.L. Barnes, W.E. Esaias, and C.R. McClain, 1994: Prelaunch Acceptance Report for the SeaWiFS Radiometer. *NASA Tech. Memo. 104566, Vol. 22,* S.B. Hooker, E.R. Firestone, and J.G. Acker, Eds., NASA Goddard Space Flight Center, Greenbelt, Maryland, 32 pp.

Vol. 23

Barnes, R.A., A.W. Holmes, W.L. Barnes, W.E. Esaias, C.R. McClain, and T. Svitek, 1994: SeaWiFS Prelaunch Radiometric Calibration and Spectral Characterization. *NASA Tech. Memo. 104566, Vol. 23,* S.B. Hooker, E.R. Firestone, and J.G. Acker, Eds., NASA Goddard Space Flight Center, Greenbelt, Maryland, 55 pp.

Vol. 24

Firestone, E.R., and S.B. Hooker, 1995: SeaWiFS Technical Report Series Summary Index: Volumes 1–23. *NASA Tech. Memo. 104566, Vol. 24,* S.B. Hooker and E.R. Firestone, Eds., NASA Goddard Space Flight Center, Greenbelt, Maryland, (in press).

Vol. 25

Mueller, J.L., and R.W. Austin, 1995: Ocean Optics Protocols for SeaWiFS Validation, Revision 1. *NASA Tech. Memo. 104566, Vol. 25,* S.B. Hooker, E.R. Firestone, and J.G. Acker, Eds., NASA Goddard Space Flight Center, Greenbelt, Maryland, 66 pp.

Vol. 26

Siegel, D.A., M.C. O'Brien, J.C. Sorensen, D.A. Konnoff, E.A. Brody, J.L. Mueller, C.O. Davis, W.J. Rhea, and S.B. Hooker, 1995: Results of the SeaWiFS Data Analysis Round-Robin (DARR), July 1994. *NASA Tech. Memo. 104566, Vol. 26,* S.B. Hooker and E.R. Firestone, Eds., NASA Goddard Space Flight Center, Greenbelt, Maryland, 58 pp.

REPORT DOCUMENTATION PAGE

Form Approved
OMB No. 0704-0188

Public reporting burden for this collection of information is estimated to average 1 hour per response, including the time for reviewing instructions, searching existing data sources, gathering and maintaining the data needed, and completing and reviewing the collection of information. Send comments regarding this burden estimate or any other aspect of this collection of information, including suggestions for reducing this burden, to Washington Headquarters Services, Directorate for Information Operations and Reports, 1215 Jefferson Davis Highway, Suite 1204, Arlington, VA 22202-4302, and to the Office of Management and Budget, Paperwork Reduction Project (0704-0188), Washington, DC 20503.

1. AGENCY USE ONLY *(Leave blank)*	2. REPORT DATE	3. REPORT TYPE AND DATES COVERED
	February 1995	Technical Memorandum

4. TITLE AND SUBTITLE
SeaWiFS Technical Report Series
Volume 26–Results of the SeaWiFS Data Analysis Round-Robin, July 1994 (DARR-94)

5. FUNDING NUMBERS
Code 970.2

6. AUTHOR(S) David A. Siegel, Margaret C. O'Brien, Jens C. Sorensen, Daniel A. Konnoff, Eric A. Brody, James L. Mueller, Curtiss O. Davis, W. Joseph Rhea and Stanford B. Hooker
Series Editors: Stanford B. Hooker and Elaine R. Firestone

7. PERFORMING ORGANIZATION NAME(S) AND ADDRESS(ES)
Laboratory for Hydrospheric Processes
Goddard Space Flight Center
Greenbelt, Maryland 20771

8. PERFORMING ORGANIZATION REPORT NUMBER
95B00081

9. SPONSORING/MONITORING AGENCY NAME(S) AND ADDRESS(ES)
National Aeronautics and Space Administration
Washington, D.C. 20546–0001

10. SPONSORING/MONITORING AGENCY REPORT NUMBER
TM–104566, Vol. 26

11. SUPPLEMENTARY NOTES
David A. Siegel, Margaret C. O'Brien, Jens C. Sorensen, Daniel A. Konnoff, and Eric A. Brody: University of California at Santa Barbara, Santa Barbara, California; James L. Mueller: San Diego State University, San Diego, California; Curtiss O. Davis and W. Joseph Rhea: Naval Research Laboratory, Washington, DC; Elaine R. Firestone: General Sciences Corporation, Laurel, Maryland

12a. DISTRIBUTION/AVAILABILITY STATEMENT
Unclassified–Unlimited
Subject Category 48
Report is available from the Center for AeroSpace Information (CASI), 7121 Standard Drive, Hanover, MD 21076–1320; (301)621-0390

12b. DISTRIBUTION CODE

13. ABSTRACT *(Maximum 200 words)*
The accurate determination of upper ocean apparent optical properties (AOPs) is essential for the vicarious calibration of the SeaWiFS instrument and the validation of the derived data products. To evaluate the role that data analysis methods have upon values of derived AOPs, the first Data Analysis Round-Robin (DARR-94) workshop was sponsored by the SeaWiFS Project during 21–23 July, 1994. The focus of this intercomparison study was the estimation of the downwelling irradiance spectrum just beneath the sea surface, $E_d(0^-,\lambda)$; the upwelling nadir radiance just beneath the sea surface, $L_u(0^-,\lambda)$; and the vertical profile of the diffuse attenuation coefficient spectrum, $K_d(z, \lambda)$\$. In the results reported here, different methodologies from four research groups were applied to an identical set of 10 spectroradiometry casts in order to evaluate the degree to which data analysis methods influence AOP estimation, and whether any general improvements can be made. The overall results of DARR-94 are presented in Chapter 1 and the individual methods of the four groups are presented in Chapters 2–5. The DARR-94 results do not show a clear winner among data analysis methods evaluated. It is apparent, however, that some degree of *outlier* rejection is required in order to accurately estimate $L_u(0^-,\lambda)$ or $E_d(0^-,\lambda)$. Furthermore, the calculation, evaluation and exploitation of confidence intervals for the AOP determinations needs to be explored. That is, the SeaWiFS calibration and validation problem should be recast in statistical terms where the *in situ* AOP values are statistical estimates with known confidence intervals.

14. SUBJECT TERMS
SeaWiFS, Oceanography, Data Analysis Round-Robin, DARR, Data Analysis Methods, Bio-Optical Processing, Radiance Attenuation Profiles, Irradiance Attenuation Profiles

15. NUMBER OF PAGES
58

16. PRICE CODE

17. SECURITY CLASSIFICATION OF REPORT	18. SECURITY CLASSIFICATION OF THIS PAGE	19. SECURITY CLASSIFICATION OF ABSTRACT	20. LIMITATION OF ABSTRACT
Unclassified	Unclassified	Unclassified	Unlimited